UiT THE ARCTIC UNIVERSITY OF NORWAY

Faculty of Science and Technology

Department of Physics and Technology

Characterization of Low Backscatter Regions in the Marine Environment by Multipolarization C- and X-band Synthetic Aperture Radar Data

—

Stine Skrunes

A dissertation for the degree of Philosophiae Doctor – July 2014

Abstract

The focus of this thesis is the application of multipolarization synthetic aperture radar (SAR) data for characterization of marine oil spills and other low backscatter ocean phenomena. SAR is a valuable tool for detection and monitoring of oil spills. However, one limitation for operational oil spill detection is the number of natural phenomena that can produce similar SAR signatures as oil spills and cause false alarms. In this thesis, a variety of features based on dual-copolarization measurements are investigated for the purpose of discrimination between oil spills and other low backscatter ocean regions. Both C-band data, which have traditionally been used for oil spill observation, and X-band data, which are only more recently applied for this purpose, are investigated. The analysis is performed on a unique data set collected during annual oil spill exercises in the North Sea.

Characterization of low backscatter regions can be limited by the proximity of the received signal to the sensor noise floor. For Radarsat-2 fine quad-polarization data, a high degree of noise contamination is here observed in the cross-polarization channels, and these are discarded. Only copolarization channels are used throughout this thesis. A number of dual-copolarization features are compared in terms of their ability to discriminate between low backscatter regions of varying origin. The two most promising features are selected and used as basis for image classification, and the results show that the feature pair can distinguish between a simulated biogenic slick and mineral oil spills.

As X-band sensors are being included in operational oil spill detection services, more documentation on the effect of the frequency and the variation between sensors is requested. X-band data from TerraSAR-X and COSMO-SkyMed are here investigated and found useful for oil spill detection in low wind conditions, except at very large incidence angles. TerraSAR-X is found preferable to COSMO-SkyMed when multipolarization techniques are used, due to the preservation of relative phase information in the former. A comparison between C- and X-band data is conducted, including analysis of near coincident acquisitions by Radarsat-2 and TerraSAR-X. No clear difference in the data quality, including signal-to-noise levels and damping ratios, is found between the sensors. Multipolarization features on the other hand, show enhanced slick-sea contrasts and better discrimination between mineral oil spills and other low backscatter regions in Radarsat-2 compared to TerraSAR-X. The presence of a non-Bragg scattering component in the data is revealed for both sensors. A relatively higher contribution of non-Bragg scattering and a larger deviation from Gaussian statistics are observed in TerraSAR-X data compared to Radarsat-2 data. A larger contribution of non-Bragg scattering to the total backscatter is also observed in slick-covered regions compared to the slick-free sea surface.

A potential for using log-cumulants for discrimination between mineral oil spills and other marine low backscatter regions is demonstrated. This is shown for both Radarsat-2 and TerraSAR-X, and for both single-polarization and multipolarization data. The proposed method has a potential for classification of low backscatter ocean regions of unknown origin.

The work presented in this thesis adds to the on-going discussion on the use of multipolarization data for oil spill characterization, including the effect of varying sensor parameters.

Acknowledgements

First of all I would like to express my gratitude to my supervisors Camilla Brekke and Torbjørn Eltoft. I thank them for giving me this opportunity, for their invaluable contributions to all my work, for their knowledgeable guidance and for helping me find my way through this project. Special thanks go to my main supervisor Camilla for her encouragement and positive attitude and for always making time for a talk or discussion on all matters, large and small. Thanks also to my second co-supervisor Rune Storvold at Norut for participation in discussions when needed and for proofreading my thesis.

I would like to acknowledge Total E & P Norge, who funded this project. I thank them for giving me the opportunity to study an interesting and important topic and for taking an interest in the work. Special thanks to Ottar Minsaas and Rune Teigland who have followed the project from beginning to end. Many thanks also to Véronique Miegebielle and the rest of the remote sensing group at Total in Pau, France for welcoming me to their group during the fall 2012.

I would like to thank NOFO for letting us participate in the oil-on-water exercises, which has been essential for this work to be possible. Special thanks to Jørn Harald Andersen in Norconsult for his efforts to include us in the exercises and for his positive attitude towards this project. Furthermore, I would like to thank KSAT, and in particular Line Steinbakk, for a valuable collaboration during these years, partly through the Multimission Oil Spill Detection project funded by the Norwegian Space Centre. During this work I have also benefited from the scientific community at Norut. In particular, I would like to thank Harald Johnsen for his help with wind retrieval from SAR data. I would also like to acknowledge John Sigurd Svendsen of the Department of Chemistry for his comments on simulation of monomolecular slicks, and Laurent Ferro-Famil of the University of Rennes 1 for valuable comments on polarimetry. Thanks also to Vladimir Kudryavtsev of the Russian State Hydrometeorological University for his contributions to my third paper.

I would also like to thank the many people at the Department of Physics and Technology who have helped me during these years. Many thanks go to Anthony Doulgeris for always taking time to answer my questions on everything from Mac and Matlab to statistics and English, and for his contributions to my last paper. Thanks also to Stian Normann Anfinsen for generously sharing his knowledge, in general and on log-cumulants in particular. Warm thanks go to all my fellow Ph.D. students and especially the students of the Barents Remote Sensing School; Mari-Ann Moen, Ane Schwenke Fors, Thomas Kræmer, Jakob Grahn, Ding Tao, Temesgen Yitayew and Vahid Akbari. Thank you for making life as a Ph.D. student much more fun.

Finally, I want to express my sincere gratitude to my family and friends for supporting me through these years. Endless thanks go to Håvard for his encouragement and patience and for being my rock.

Stine Skrunes,
Tromsø, July 2014

Contents

Nomenclature

List of Notation

A	anisotropy
A'	anisotropy in the dual-copolarization case
A_{12}	normalized difference between the two largest eigenvalues
B	bandwidth
c	speed of light
$\mathbf{C}$	covariance matrix
$\mathbb{C}$	complex plane
d	polarimetric dimension
d_a	antenna length
D_{CO}	normalized copolarization difference
$\mathbf{e}_i$	i^{th} eigenvector of $\mathbf{T}$
E_p^i	electromagnetic field of the incident wave in polarization p
E_p^s	electromagnetic field of the scattered wave in polarization p
f	probability density function
F	combined feature
g_{pq}	scattering coefficients in the Bragg model
h	standard deviation of the surface height
H	entropy
H'	entropy in the dual-copolarization case
I	intensity
k	wave number
$\mathbf{k}$	Pauli scattering vector
$\mathbf{l}$	Lexicographic scattering vector
L	number of looks
M	ν^{th} order log-moment
$\mathcal{M}$	Mellin transform
n	order of resonance

p_B	polarization ratio of Bragg scatter components
p_i	probability of the i$^{\text{th}}$ scattering mechanism
r_a	azimuth resolution
r_{CO}	real part of the copolarization cross product
r_g	ground range resolution
r_s	slant range resolution
R	distance from sensor to ground
$\mathbb{R}^+$	line of positive real numbers
s	complex transform variable
S	speckle component in the univariate case
S_{pq}	complex scattering coefficient of transmit polarization p and receive polarization q
$\mathbf{S}$	scattering matrix
T	texture variable
$\mathbf{T}$	coherency matrix
v	frequency
W	wave number spectral density of the surface roughness
$\widetilde{\mathbf{W}}$	speckle component in the multivariate case
$s\mathcal{W}_d^{\mathbb{C}}$	scaled complex Wishart distribution
X	positive, real-valued random variable
$\mathbf{Z}$	complex Hermitian random matrix
$\bar{\alpha}$	mean scattering angle
α_i	scattering angle of the i^{th} eigenvalue
α_i'	scattering angle of the i^{th} eigenvalue in the dual-copolarization case
γ	gamma distribution
γ_{CO}	copolarization power ratio
δ_p	penetration depth
ϵ	complex electric permittivity
ϵ_0	complex electric permittivity of vacuum
ϵ_r	relative dielectric constant
ζ	angle between the normal to the surface and the normal of a facet in the plane perpendicular to the plane of incidence
θ	incidence angle
θ_i	incidence angle of a tilted facet
κ_ν	ν^{th} order sample log-cumulant
λ	wavelength
λ_B	Bragg wavelength
λ_i	i^{th} eigenvalue of $\mathbf{T}$
Λ	average intensity
μ	geometric intensity
μ_ν	ν^{th} order sample log-moment
ρ_{CO}	magnitude of copolarization correlation coefficient
σ	population mean intensity

$\sigma_{\phi CO}$	standard deviation of copolarization phase difference
σ_0	radar backscatter coefficient
σ_{0B}	Bragg scattering coefficient
σ_{0nB}	non-Bragg scattering coefficient
$\mathbf{\Sigma}$	population mean matrix
τ	pulse length
ϕ_{CO}	copolarization phase difference
ϕ_{pq}	phase of the complex scattering coefficient of transmit polarization p and receive polarization q
ϕ_X	Mellin kind characteristic function of X
χ	ellipticity angle
ψ	orientation angle
Ψ	angle between the normal to the surface and the normal of a facet in the plane of incidence
ω	angular frequency
Ω_+	cone of positive definite Hermitian matrices

List of Acronyms

AIRSAR	Airborne Synthetic Aperture Radar
ALOS	Advanced Land Observing Satellite
API	American Petroleum Institute
ASI	Italian Space Agency
BAOAC	Bonn Agreement Oil Appearance Code
CAST	Chinese Academy of Space Technology
CC	conformity coefficient
CDTI	Spain's Center for Development of Industrial Technology
CF	characteristic function
CONAE	Argentina National Space Activities Commission
COSMO-SkyMed	COnstellation of small Satellites for the Mediterranean basin Observation
CP	compact polarimetry
CRESDA	China Centre for Resources Satellite Data and Application
CSA	Canadian Space Agency
DLR	German Aerospace Center
DoP	degree of polarization
DR	damping ratio
DWH	Deepwater Horizon
EM	electromagnetic
EMSA	European Maritime Safety Agency
ENVISAT	Environmental Satellite
ERS	European Remote Sensing Satellite
ESA	European Space Agency
IFO	Intermediate Fuel Oil
IMO	International Maritime Organization
IR	infrared
ISRO	Indian Space Research Organization
JAXA	Japan Aerospace Exploration Agency
JERS	Japanese Earth Resources Satellite
KARI	Korea Aerospace Research Institute
KSAT	Kongsberg Satellite Services
MARPOL	International Convention for the Prevention of Pollution from Ships
MLC	multilook complex
MLI	multilook intensity
MoD	Italian Ministry of Defense
NASA	National Aeronautics and Space Administration
NESZ	noise equivalent sigma zero
NOFO	Norwegian Clean Seas Association for Operating Companies
Norut	Northern Research Institute
NP	nonpolarized scattering component

OLA	oleyl alcohol
OOW	oil-on-water
PALSAR	Phased Array type L-band Synthetic Aperture Radar
PD	polarization difference
pdf	probability density function
PR	polarization ratio
RAR	real aperture radar
ROI	region of interest
SAR	synthetic aperture radar
SCS	single-look complex slant
SIR-C/X-SAR	Spaceborne Imaging Radar-C/X-Band Synthetic Aperture Radar
SLAR	side-looking airborne radar
SLC	single-look complex
SLI	single-look intensity
SSC	single-look slant range complex
UAVSAR	Uninhabited Aerial Vehicle Synthetic Aperture Radar
UV	ultraviolet

Chapter 1

Introduction

The focus of this thesis is the application of multipolarization C- and X-band synthetic aperture radar (SAR) data for characterization of marine oil spills and other low backscatter ocean phenomena. This chapter presents the motivation for the study and the outline of the thesis.

1.1 Motivation

Marine oil spills can have serious environmental and economic effects. Large oil spills in connection with oil production and transportation receive massive publicity. However, a much larger volume of oil is released into the oceans during operational discharges from ships, which take place continuously around the world and are often illegal.

Spaceborne SAR sensors have proven to be a useful tool for detection and monitoring of illegal and accidental oil releases. SAR sensors can operate during both day and night and in most weather conditions, and are used in operational oil spill detection services for continuous surveillance of vast ocean areas. However, some challenges still exist. The most important may be the so-called *look-alikes*. These are natural phenomena which produce similar SAR signatures as oil spills and include natural films produced by marine organisms, low wind areas, grease ice, rain cells, shear zones, internal waves and ship wakes [Brekke and Solberg, 2005]. Discrimination between oil spills and look-alikes is important to avoid false alarms and ensure more reliable oil spill detection services. Extraction of slick information, e.g., thickness, volume and oil type, is also desired to obtain more effective response operations. This type of information can currently not be retrieved from SAR data. Reliable methods for discrimination between oil slicks and look-alikes and for extraction of slick information can contribute to reducing the amount of illegal oil releases and to limit the environmental effects of accidental spills. Much research efforts are put into these topics. The main focus of this thesis is *characterization* of low backscatter ocean regions, which here refers to the tasks of describing the properties of a given region and the identification of its origin, e.g., oil spill or other phenomena.

Currently, single-polarization SAR data are used for operational oil spill detection.

Over the last decade, several sensors operating in dual- and quad-polarization modes, in which two or four polarization channels are acquired simultaneously, have been launched, e.g., TerraSAR-X and Radarsat-2. A number of studies have investigated the use of these data types for observing oil spills, and a potential for oil slick characterization has been demonstrated in, e.g., [Migliaccio et al., 2008, Nunziata et al., 2008, Migliaccio et al., 2009b, Minchew et al., 2012, Shirvany et al., 2012].

Operational oil spill detection services rely on high spatial and temporal coverage of the ocean surfaces. Conventionally, SAR sensors operating in the C-band (3.75 - 7.5 GHz) frequency range have been used for oil spill detection. However, several of the more recently launched sensors, as well as planned missions, operate in the X-band (7.5 - 12 GHz) range. As these sensors are now being incorporated into the detection services to improve the coverage, more documentation on the applicability of X-band sensors compared to C-band sensors is requested by the industry.

One challenge for the research on remote sensing of marine oil spills is the limited availability of data, particularly multipolarization data, which are currently not used operationally. Controlled releases of oil for research purposes are generally not allowed. However, an annual exercise is conducted in the North Sea where oil is released onto the open ocean in order to test newly developed oil spill response equipment. We have taken advantage of these opportunities to collect the unique data set used in this thesis, which includes data from different satellite and airborne sensors and corresponding ground truth information. Multipolarization SAR data from Radarsat-2, TerraSAR-X and the COnstellation of small Satellites for the Mediterranean basin Observation (COSMO-SkyMed), containing mineral oil spills and simulated biogenic slicks, are acquired. This data set allows for a thorough study of the imaging of oil spills with C- and X-band SAR in dual- and quad-polarization modes.

This thesis presents an extensive investigation on the use of multipolarization C- and X-band SAR data for characterization of marine oil spills and other low backscatter ocean phenomena. Four papers compose the research contribution of the thesis, and the main objectives are:

- to compare the usefulness of various multipolarization SAR features in terms of oil slick characterization ability (Papers I - III),
- to investigate the usefulness of X-band data for oil spill observation (Paper I and Paper III),
- to compare near-coincident C- and X-band acquisitions of low backscatter regions of various origin in terms of data quality and various signal characteristics (Paper III),
- to investigate the contribution of different scattering mechanisms in various low backscatter ocean phenomena (Paper III),
- to investigate the potential of selected statistical descriptors for discrimination between oil spills and other low backscatter ocean phenomena (Paper III and Paper IV).

This thesis presents for the first time an annual series of experiments where multipolarization acquisitions of real oil spills on the open ocean are collected and analyzed. Each experiment is conducted at the same location and time of year and data are collected with a set of SAR sensors.

1.2 Thesis Outline

This thesis is organized as follows. Chapter 2 gives an introduction to oil spills, their properties and effects when oil is released into the marine environment. Chapter 3 provides a brief discussion on the use of various sensors for remote sensing of oil spills. The basic principles and properties of SAR sensors are described in Chapter 4, including an introduction to SAR polarimetry and statistical data properties. The use of SAR sensors for observing oil spills is discussed in Chapter 5. Chapter 6 describes the oil-on-water experiments and the data collection. A summary of the four publications that contains the research contribution of this thesis is provided in Chapter 7, whereas the full papers are presented in Chapters 8 - 11. Research conclusions and a future outlook are given in Chapter 12.

Chapter 2

Oil Spills in the Marine Environment

Oil is released into the marine environment on a regular basis. The major oil spills that attract the attention of the media and the public only account for a small part of these releases. Large volumes of oil are also discharged from ships during routine operations. These spills, which can be both legal and illegal, take place continuously around the world, and also pose a threat for the marine environment. This chapter gives an introduction to the topic of marine oil spills, including an overview of important oil properties, weathering mechanisms, oil spill effects and actions taken to reduce the problem.

2.1 Accidents, Discharges and Natural Releases of Oil

The volume of oil released into the world's oceans every year is estimated to about 1.2 million tonnes. About half of this is released as natural seeps from geological strata below the sea floor, and the other half from anthropogenic sources during oil production, transportation and consumption [Schmidt-Etkin, 2011].

Accidental spillage from tankers has been recorded since 1970. Despite the increasing volume of oil that is transported by sea, a significant decrease in the number and volume of medium and large spills has taken place since 1970. The oil released in medium and large ($>$ 7 tonnes) accidents amounted to 12.000 tonnes in 2010, 2.000 tonnes in 2011, 1.000 tonnes in 2012 and 7.000 tonnes in 2013 [The International Tanker Owners Pollution Federation Limited, 2014]. The oil spill occurrence correlates with major production areas and transportation routes. One fifth of the oil spilled on global scale in the period 1960 - 2002 took place in the European Atlantic, with the English Channel and the Galician coast as the most affected areas [Vieites et al., 2004].

Two well-known tanker accidents are those of *Exxon Valdez* and *Prestige*. *Exxon Valdez* ran aground in the Prince William Sound in Alaska in March 1989. An estimated 36.000 tonnes of Alaska North Slope crude oil was released and more than 2.000 km of coastline were oiled [National Research Council, 2003]. In November 2002, the *Prestige* tanker sank off the Spanish coast of Galicia, releasing $\sim$ 64.000 tonnes of oil [Kluser et al., 2006]. More recently, the Deepwater Horizon (DWH) oil spill in the Gulf of Mexico caught international attention.

After the blowout in April 2010, an estimated 700.000 m^3 of oil were released before the well was capped in July 2010. The accident had large biological and economic consequences and is the worst environmental disaster in the history of the United States [Kwon and Li, 2012, Minchew et al., 2012].

In addition to the accidental releases of oil, intentional discharges, legal and illegal, take place continuously around the world during routing tanker operations. Oily waste, including ballast water, tank washing residues and bilge water, are discharged rather than delivered at appropriate facilities due to costs, increased dock time, lack of facilities and lack of inspections and sanctions [Kluser et al., 2006]. The amount of illegally discharged oil during routine operations is difficult to estimate and varying numbers are found in the literature. According to [Kluser et al., 2006], at least 3000 annual major events of illegal dumping have been estimated for Europe alone. This amounts to 1.750 - 5.000 tonnes in the Baltic Sea, 15.000 - 60.000 tonnes in the North Sea and more than 400.000 tonnes in the Mediterranean. The oil released in operational discharges may hence far exceed the accidental spillage [Kluser et al., 2006].

2.2 Oil Properties

The term *oil* describes a wide variety of both natural substances of plant, animal and mineral origin, and different synthetic compounds. *Crude oil* is a naturally occurring oil, generated by geological and geochemical processes [National Research Council, 2003]. A number of oil properties can affect the fate and behavior of an oil spill:

- *Viscosity* is the oils resistance to flow. Low viscosity oils flow more easily than those of high viscosity [National Research Council, 2003]. The former type spreads more rapidly than the latter, and is easier to pump and skim [Fingas, 2011b]. The viscosity is largely determined by the relative amount of light and heavy components, with decreasing values as the amount of light components increases. In most oils, the viscosity increases approximately exponentially with decreasing temperatures [Fingas, 2011b].

- *Density* is the mass of a given volume. This property is used to define light versus heavy oils, and indicates whether a specific oil will float or sink in water. Sea water has density 1.03 g/cm^3 (at 15°C), whereas the densities of most oils are in the range 0.7 - 0.99 g/cm^3 (at 15°C). Hence, most oils will float [National Research Council, 2003, Fingas, 2011b]. The density decreases approximately linearly with temperature [Hollebone, 2011].

- *Solubility* in water measures the amount of oil that will dissolve in the water column on molecular basis. The solubility of oil in water is small, generally less than 100 parts per million, but the soluble parts of the oil can be toxic for the aquatic life [National Research Council, 2003, Fingas, 2011b].

- *Flash point* is the temperature where enough vapor is produced that it could ignite if exposed to an open flame [Fingas, 2011b].

- *Pour point* is the temperature where the time it takes to pour the oil from a standard measuring vessel exceeds a specified limit [Fingas, 2011b].

- *American Petroleum Institute (API) gravity* is a measure of specific gravity, which describes the density of oil compared to water. API of water is 10°, and oils with progressively larger density have lower API values [Fingas, 2011b].

- *Interfacial tension/ surface tension* is the attraction or repulsion force between oil and water surface molecules. Lower values of interfacial tension indicate a greater extent of spreading [Fingas, 2011b].

Because the crude oil composition varies, each oil type has unique characteristics, which will affect the behavior and effects of an oil spill and the efficiency of cleanup efforts. The most important properties for the fate and behavior of spills are viscosity, density and solubility [National Research Council, 2003, Fingas, 2011b]. Typical properties of various oil types are given in Table 2.1.

Table 2.1: Typical oil properties for selected oil types [Fingas, 2011b]. IFO denotes Intermediate Fuel Oil.

	Gasoline	**Diesel**	**Light crude**	**Heavy crude**	**IFO**	**Bunker C**
Viscosity (mPa·s, 15°C)	0.5	2	5 to 50	50 to 50.000	1.000 to 15.000	10.000 to 50.000
Density (g/mL, 15°C)	0.72	0.84	0.78 to 0.88	0.88 to 1.0	0.94 to 0.99	0.96 to 1.04
Solubility in water (ppm)	200	40	10 to 50	5 to 30	10 to 30	1 to 5
Flash point (°C)	-35	45	-30 to 30	-30 to 60	80 to 100	>100
Pour point (°C)	not relevant	-35 to -10	-40 to 30	-40 to 30	-10 to 10	5 to 20
API gravity	65	35	30 to 50	10 to 30	10 to 20	5 to 15
Interfacial tension (mN/m, 15°C)	27	27	10 to 30	15 to 30	25 to 30	25 to 35

2.3 Weathering of Marine Oil Spills

Crude oils released into the marine environment are immediately subjected to *weathering processes*, which transform the physical and chemical characteristics of the released substance:

- *Evaporation* is in many cases the most important weathering process in terms of mass balance. Within a few days, up to 75% (40%) of the original volume of light (medium) crudes can be lost. Heavy or residual oils will lose no more than 10% in the first days after the spill [National Research Council, 2003]. The density and viscosity increase during the evaporation process [Lehr, 2001].

- *Emulsification* is the formation of various states of water in oil. Emulsions may not always form, and water may simply be entrained by the oil due to viscous forces, without forming more stable emulsions. It is distinguished between four water-in-oil states: stable emulsions, meso-stable emulsions, unstable emulsions and entrained water. Properties change significantly between the different types [National Research Council, 2003]. The water content in stable emulsions is between 60% and 85%, expanding the volume by three to five times. The density and viscosity increase with increasing emulsification, the latter typically by three orders of magnitude [National Research Council, 2003]. By increasing the viscosity and thickness, emulsification contributes significantly to the persistence of oil spills [Reed et al., 1999].

- *Dispersion* takes place when the oil is subjected to turbulent wave energy, and parts of the oil break up into drops of 1 - 1000 μm diameters, which are mixed down in the water column. For slicks of low viscosity oil under high sea state conditions, dispersion becomes the dominating process for removal of oil, and 90% or more of the slick may be dispersed. As the viscosity of the slick increases, the dispersibility decreases [Lehr, 2001].

- *Dissolution* is the chemical stabilization of oil components in the water, accounting for a small portion of the oil loss. However, as the soluble components of the oil can be toxic to aquatic species, it is still an important process [National Research Council, 2003].

- *Spreading* is especially important in the initial phase after release. The oil does not spread uniformly, and areas of thinner and thicker oil will form [Lehr, 2001]. It has been found that more than 90% of the oil is contained in less than 10% of the slick area [Hollinger and Mennella, 1973]. A high viscosity or high density will decrease the spreading in the first stage of the process [Kotova et al., 1998].

- *Oxidation* alters the mixture of organic compounds in the crude oil, creating new compounds and rearranging the distribution of the residuals. The oxidized products are more soluble in water than the original. Preferential oxidation of compounds

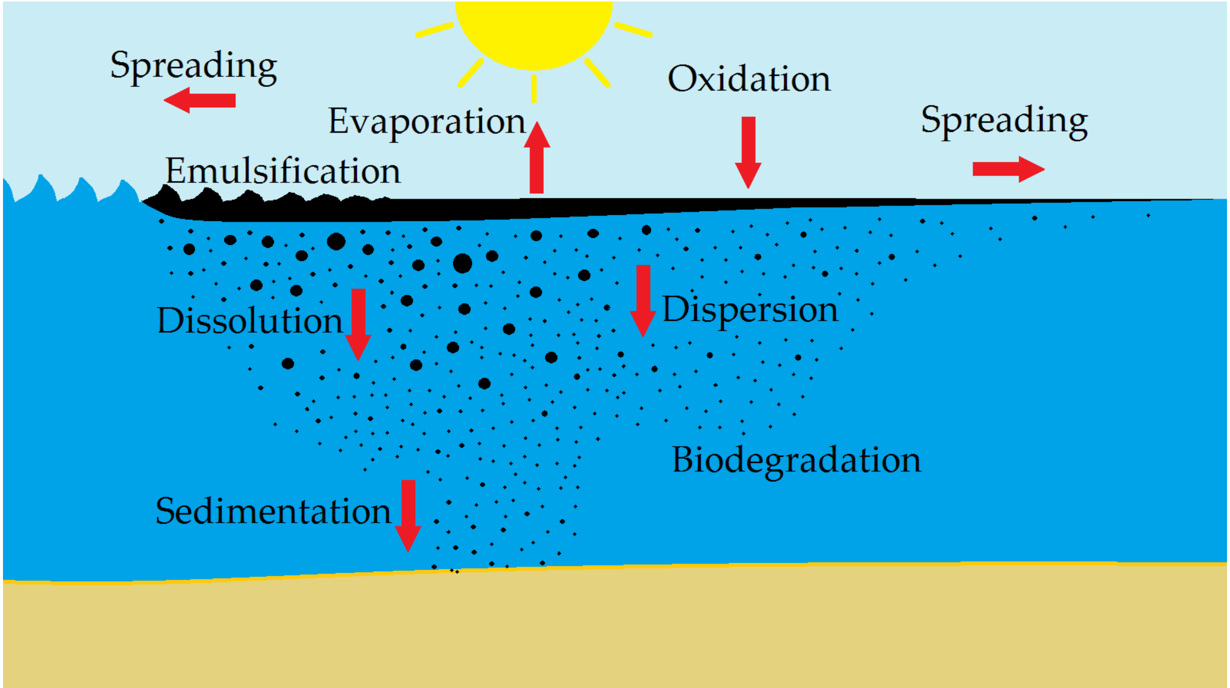

Figure 2.1: Weathering processes acting on an oil spill. Figure adapted from [The International Tanker Owners Pollution Federation Limited, 2002].

of low molecular weight increases the density of the unoxidized residue [National Research Council, 2003].

- *Biodegradation* of hydrocarbons has been considered one of the principal removal mechanisms in the aquatic environment. Environmental factors, including oxygen concentration, nutrients, temperature, salinity and pressure, as well as oil properties and energy level of the environment affect the biodegradation rates [National Research Council, 2003].

Fig. 2.1 illustrates the various weathering processes. The weathering depends more on the oil type than on environmental conditions. However, most processes are highly temperature dependent and will often slow to insignificant rates as the temperature decreases towards 0°C [National Research Council, 2003]. Oil spills may have a longer residence in cold environments, as the oil may be more viscous and the weathering slower in these conditions [Shigenaka, 2011]. The presence of breaking waves, occurring at wind speeds > 5 m/s, is a requirement for water uptake, and the dispersion rate varies proportionally to the square of the wind speed [Kotova et al., 1998]. Winds and currents can also enhance spreading [Fingas, 2011c]. The relative contribution of each weathering mechanism changes with time. Various models for the prediction of oil movement and weathering are described in, e.g., [Klemas, 2010, Fingas, 2011d].

2.4 Oil Spill Effects

Oil released into the marine environment can have serious environmental impacts, as well as economic consequences. The impacts and damages vary from event to event and depend on a number of factors, including the rate and volume of the release, the properties of the released oil, the properties of the local ecosystems, season, oceanographic conditions and weather conditions [Schmidt-Etkin, 2011, Shigenaka, 2011].

Most of the reported tanker spills take place in areas belonging to the Large Marine Ecosystems of the World, which are defined as the most productive ocean areas, and in zones with fragile coral reef ecosystems and marine biodiversity hotspots. Following an oil spill, flora and fauna populations in the polluted area may be reduced or die out. Birds, sea mammals, fish and marine invertebrate species are among the most impacted groups, but the whole food chain can be affected. Marine organisms may be harmed from direct contact, ingestion and through destruction of habitats. Direct exposure of birds to oil can lead to oil-covered feathers. This in turn can prevent them from flying, making them heavy enough to sink or lead to death by hypothermia. Fish can ingest oil through their gills, which can lead to inhibition of the ability to reproduce, cause deterioration in the DNA and cause deformed offspring. Oil that sinks can mix with sediments and destroy the habitats of bottom-dwelling organisms as well as spawning sites for other fauna. The actual effects and the time required for recovery vary between species and are not exactly known. Oil may also wash up on shore, causing damage to the coastal ecosystems, and possibly leak into fresh groundwater reservoirs. If the oil catches fire, it releases gases that contribute to global warming and acid rain [Vieites et al., 2004, Kluser et al., 2006]. The presence of oil spills can also affect the ocean-atmosphere interaction such as energy transfer from wind to waves, surface temperature variability and gas exchange [Ivanov, 2011].

The worldwide average cost of cleanup ranges between 20 - 200 dollars per liter oil, depending on oil type and location [Fingas, 2011a]. The losses attributed to the DWH accident is reported to be approximately 22.6 billion dollars, not including long-term environmental and economic losses. Nearly 7000 animals, including birds, turtles, dolphins and other mammals were killed due to this accident. The livelihoods of fishermen are at risk as they lost their source of income, and the tourism industry has been heavily affected [Kwon and Li, 2012].

2.5 Efforts to Reduce Oil Spills

The international legal regime regarding ship pollution is defined in the International Convention for the Prevention of Pollution from Ships (MARPOL 73/78), adopted in 1973 by the International Maritime Organization (IMO). The convention defines restrictions on the amount of oil that can be legally released in a given area and within a certain distance from shore. It includes a definition of Special Areas that are considered especially vulnerable, where discharges are completely prohibited, with minor and well-defined exceptions. The majority of the European seas are considered Special Areas, except for the Norwegian

Sea, the Bay of Biscay and the Iberian Coast [Kluser et al., 2006, Ferraro et al., 2009]. However, large amounts of oil are still discharged in these areas, as will be further discussed in Section 5.1.

The European Community urges marine companies to stop illegal dumping, and often brings to justice those that don't obey. Requirements for proper waste collection facilities are included in the European Directive 2000 59. Other measures reinforced by the European Commission include appropriate legal systems and aerial and satellite observation [Kluser et al., 2006].

In the North Sea, regular aerial surveillance for oil spill detection started in the 1980s. The eight countries bordering to the North Sea work together under the Bonn Agreement, which was signed in 1996 [Ferraro et al., 2009]. CleanSeaNet is the European satellite oil spill monitoring and vessel detection service that has been operated by the European Maritime Safety Agency (EMSA) since 2007. The objectives of ClenSeaNet are to monitor the European ocean areas to identify illegal discharges and to support response operations during accidental pollution [European Maritime Safety Agency, 2011]. The use of remote sensing data for the purpose of oil spill detection and characterization is further discussed throughout this thesis.

Chapter 3

Remote Sensing of Marine Oil Spills

Remote sensing is used to detect illegal and accidental oil releases, and to assist in response operations during oil spill accidents. A variety of sensor types that utilize different parts of the electromagnetic (EM) wave spectrum can be used for airborne and/or spaceborne remote sensing, each with its own advantages and limitations. A combination of different sensors and carrier platforms is used in the oil spill response system. The use of various sensor types for oil spill observation is described in the next sections, and a summary is presented in Table 3.1. Comparisons of the different sensors can be found in, e.g., [Jha et al., 2008, Klemas, 2010, Fingas and Brown, 2011, Leifer et al., 2012].

3.1 Visible Sensors

Sensors operating in the visual part of the EM spectrum include still cameras, video, multi- and hyperspectral sensors. In these wavelengths, oil has higher surface reflectance than water. However, many false alarms, e.g., sun glint, wind sheens and biological slicks, limit the usefulness of visible techniques for oil spill detection, and these sensors are largely restricted to documentation of spills. Visible sensors are also limited by the requirement of daylight and clear skies, which makes them less useful at spaceborne platforms [Fingas and Brown, 2011].

The visual appearance of oil varies somewhat with thickness. For aerial patrol flights, the Bonn Agreement Oil Appearance Code (BAOAC) has been developed to classify various areas of an oil slick according to its visual appearance and to estimate oil slick volumes. The BAOAC oil classes are defined in Table 3.2 and the visual appearance of the different zones are shown in Fig. 3.1.

3.2 Infrared Sensors

Solar radiation is absorbed by oil, and partly reemitted as thermal energy in the infrared (IR) region. In thermal IR images, thick oil appears hot or bright, oil of intermediate thicknesses appears cool and dark, whereas thin oil or sheens are not detected. The thicknesses where

Table 3.1: Applicability of the various EM bands for oil spill observation [Klemas, 2010].

	Visible	**Thermal infrared**	**Ultraviolet**	**Passive microwave**	**Radar**
Wavelength	0.4 - 0.7 μm	3 - 14 μm	0.3 - 0.4 μm	0.2 - 0.8 cm	1 - 30 cm
Oil detection mechanism	Reflectivity	Emissivity	Reflectivity fluorescence	Emissivity reflectivity	Wave damping (dielectric properties)
Oil contrast vs. water	Bright	Dark/bright	Bright	Bright	Dark
Oil thickness	No	Relative	No	Relative	No
Night operation	No	Yes	No	Yes	Yes
Weather limitations	Requires clear sky	Light fog	Requires clear sky	Heavy fog and rain	Heavy fog and rain
False target probability	High	Medium	Low	Low	High

the transitions take place are not well understood. However, the transition between hot and cold oil seems to be found between 50 and 150 μm, and a minimum detectable thickness between 10 and 70 μm has been indicated. Emulsions can normally not be detected by IR sensors, probably due to the large water content, which reduces the temperature difference between the oil and the surrounding sea. Thermal IR can be used also at night (the oil appears cooler than the surrounding sea), but with lower contrast than during daytime. As thermal IR sensors provide relative thickness information, these are valuable for guiding response efforts to the thickest parts of an oil spill. Also for IR, look-alikes, including seaweed, shoreline and oceanic fronts, can give false detections [Klemas, 2010, Fingas and Brown, 2011].

3.3 Ultraviolet Sensors

Oil slicks have a significantly higher reflection than water in the ultraviolet (UV) region, also in the thinner parts of a slick. Hence, IR and UV images can be overlaid and used to produce maps of relative thickness. Look-alike phenomena in the UV region include wind slicks, sun glint and biological material. As UV and IR have different look-alikes, a combination of the two can provide more reliable oil spill indications than if either one technique is used individually. As UV light is strongly scattered by the atmosphere, only airborne sensors are useful [Klemas, 2010, Fingas and Brown, 2011].

Table 3.2: Oil spill classes under the Bonn Agreement Oil Appearance Code, and corresponding thickness and volume ranges [Bonn Agreement, 2009].

Appearance	**Thickness (μm)**	**Litres per km^2**
Sheen (silvery/grey)	0.04 - 0.30	40 - 300
Rainbow	0.30 - 5.0	300 - 5.000
Metallic	5.0 - 50	5.000 - 50.000
Discontinuous true color	50 - 200	50.000 - 200.000
Continuous true color	$>$ 200	$>$ 200.000

3.4 Laser Fluorosensors

Some compounds in mineral oils absorb UV light and become electronically excited. The excitation is released through fluorescence emission, mainly in the visible region. The fluorescence is a strong indication of oil as few other compounds show this behavior. Different oil types provide slightly different fluorescent intensities and spectral signatures, enabling a distinction between some oil types under certain conditions. These sensors are viewed as a powerful tool in oil spill remote sensing as they can be used to estimate oil thickness, to discriminate between oiled and unoiled seaweed and to detect oil on shorelines and in some ice and snow conditions [Fingas and Brown, 2011].

3.5 Microwave Radiometers

Microwave radiometers are passive sensors that measure the emissivity of the surface. Clean sea and oil have apparent emissivities of 0.4 and 0.8, respectively, and the oil slicks are therefore detected as bright areas compared to the surrounding sea. The emissivity is expected to vary with thickness, but attempts to extract thickness information have not provided satisfactorily results due to an ambiguous relation between measurement and thickness. Microwave radiometers are limited by false detections due to biogenic material, the signal-to-noise ratio is low, and achieving a high spatial resolution is difficult. However, emerging technologies may improve the potential of these sensors for measuring slick thickness [Klemas, 2010, Fingas and Brown, 2011].

3.6 Radars

A radar is an active sensor, which transmits microwaves and records the backscattered signal. Oil slicks are detected by radars as areas of reduced backscatter. Radars are very useful sensors, as they can be used during both day and night, and in most weather conditions. However, a number of look-alike phenomena pose a challenge for oil spill detection by these sensors.

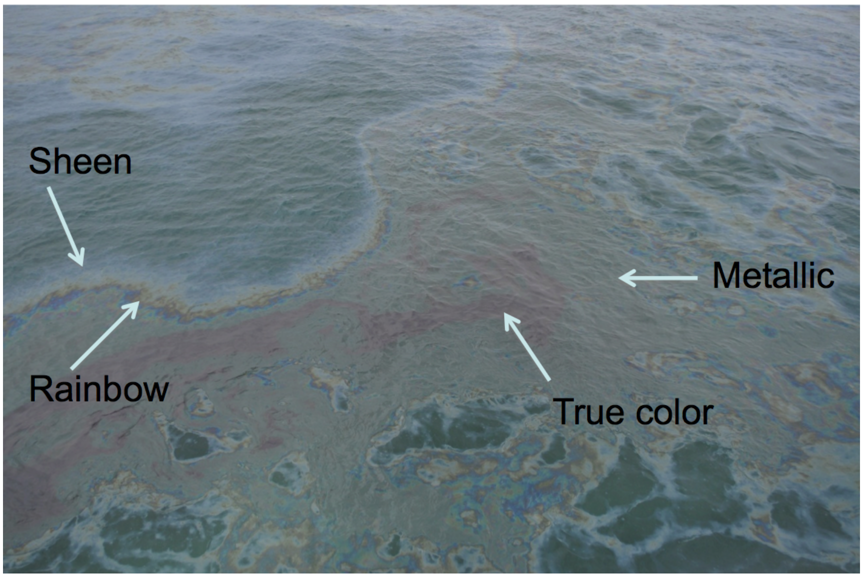

Figure 3.1: Visual appearance of various oil spill zones. Photo: Stine Skrunes.

Two types of imaging radars are used for remote sensing, i.e., side-looking airborne radar (SLAR) and synthetic aperture radar (SAR). SLAR is an older, but less expensive technology, where high resolution is achieved by a large antenna. A different concept is applied in SAR, where the forward motion of the sensor and sophisticated electronic processing are used to achieve high resolution, independent of the distance between the sensor and the surface [Fingas and Brown, 2011].

SAR is seen as the most efficient satellite sensor for oil spill observation, and a rich literature on the subject can be found. The rest of this thesis will focus on SAR, as this is the sensor used in the work presented here. The principle and characteristics of SAR are described in Chapter 4, and the use of SAR sensors for detection and characterization of oil spills is addressed in Chapter 5.

Chapter 4

Remote Sensing by SAR

SAR is considered the most efficient satellite sensor for oil spill detection. This chapter describes the basic principle and properties of SAR, with emphasis on SAR polarimetry and selected statistical data properties.

4.1 Imaging Geometry

SAR is an active, imaging sensor, transmitting microwaves and recording the backscattered signal, producing a two-dimensional image of the ground. The image matrix consists of pixels associated with a small area on the Earth's surface. Each pixel represents the reflectivity of the scatterers contained in the corresponding resolution cell. The surface reflectivity, also expressed as the radar backscatter coefficient σ_0, is a function of the radar system parameters, e.g., frequency, polarization and incidence angle, and of the surface parameters such as roughness, dielectric properties and topography [Lee and Pottier, 2009]. As SAR sensors provide their own illumination source, and microwaves can penetrate clouds, SAR can operate in both day and night, and in nearly all weather conditions.

The geometry of a SAR sensor system is shown in Fig. 4.1 and Fig. 4.2. The sensor platform is moving in the *azimuth* direction, and the SAR antenna is looking sideways in the *range* direction, perpendicular to the direction of travel. The antenna dimensions determine the illuminated area on the ground. The coverage of a scene in range direction is referred to as the *swath width*. The part of the swath closest to the satellite track is the *near range*, and the part furthest away from the track is the *far range*.

Two different range measures are used, i.e., *slant range* and *ground range*, as indicated in Fig. 4.2. Slant range is measured along the radar line of sight, and the pixels correspond to the actual SAR measurements, but the geometry is distorted relative to a map projection. The measurements can be resampled into ground range, which is the range along the ground measured from nadir, to obtain a correct geometry relative to a map projection. This requires a reference surface or projection, and an interpolation must be done, introducing correlation between pixels [Oliver and Quegan, 2004].

The illumination geometry is often given in terms of the *incidence angle*, which is

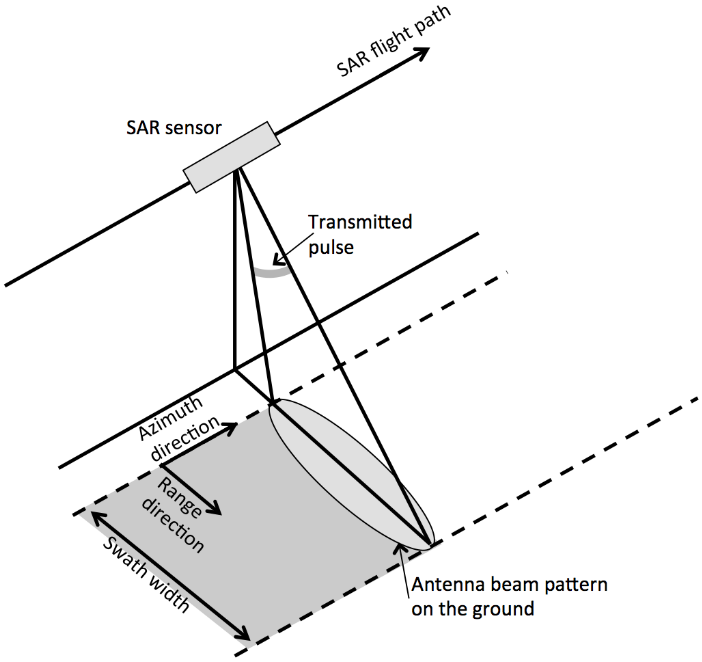

Figure 4.1: Imaging geometry of a SAR sensor. Figure adapted from [van Zyl and Kim, 2011].

the angle between the radar beam and the normal to the surface. The *grazing angle* is the complement of the incidence angle. The geometry may also be described by the *look angle*, which is the angle between the radar beam at the sensor and the vertical, and its complement, the *depression angle*, as indicated in Fig. 4.2 [van Zyl and Kim, 2011].

4.2 Resolution

The spatial resolution is the minimum distance between two points on the surface that allows the reflected signal from the two points to be separated. For objects separated by a smaller distance, the reflections will overlap and they will appear as one target. In SAR, surface elements are separated in range and azimuth directions by using the time delay between echoes and the Doppler history, respectively [Elachi and van Zyl, 2006].

The slant range resolution r_s is given as

$$r_s = \frac{c}{2B}, \tag{4.1}$$

where c is the speed of light and B is the signal bandwidth given as $B = 1/\tau$, where τ is the pulse length. The ground range resolution r_g is related to r_s (using flat Earth approximation) through

$$r_g = \frac{r_s}{\sin\theta}, \tag{4.2}$$

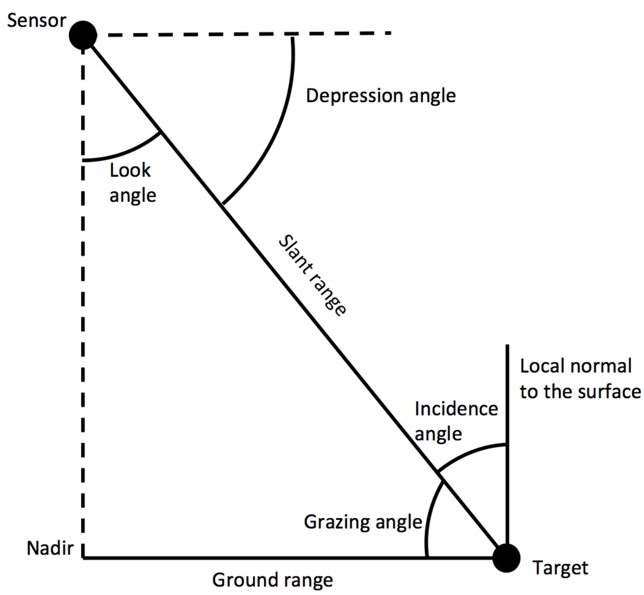

Figure 4.2: Illustration of some important radar imaging terms. Figure adapted from [van Zyl and Kim, 2011].

and hence varies nonlinearly across the swath with the incidence angle θ. To obtain a good range resolution, a short pulse can be used. However, this is in conflict with the desire to have a high-energy pulse to enhance the signal-to-noise ratio. This problem is overcome by using a frequency modulated pulse, called a *chirp*, in which the frequency is linearly changed through the pulse. The chirp is applied in both real aperture radar (RAR) and SAR sensors [Elachi and van Zyl, 2006].

In the azimuth direction however, the SAR is distinctive from other systems as it improves the azimuth resolution by aperture synthesis. In a RAR sensor, the azimuth resolution is given as $R\lambda/d_a$, where R is the distance from the sensor to the surface, λ is the wavelength of the SAR signal and d_a is the antenna length. In this case, the resolution may be enhanced by reducing the distance between the sensor and the surface or by increasing the antenna length. None of these options are practical solutions for a spaceborne sensor. To improve the azimuth resolution in SAR, a synthetic aperture technique is applied. When the radar beam is directed orthogonal to the direction of travel, a point on the surface is illuminated for an extended period of time as the radar beam traverses the point. This is illustrated in Fig. 4.3. As the beam passes over the target, the point is hit by a number of pulses at slightly varying observation geometry, producing a systematic change in the reflected signal phase. Through sophisticated signal processing, the phase and Doppler measurements of the point allows for a larger antenna to be synthesized, which can be several orders of magnitude larger than the physical antenna, enhancing the azimuth resolution [McCandless and Jackson, 2004]. The resulting SAR spatial azimuth resolution

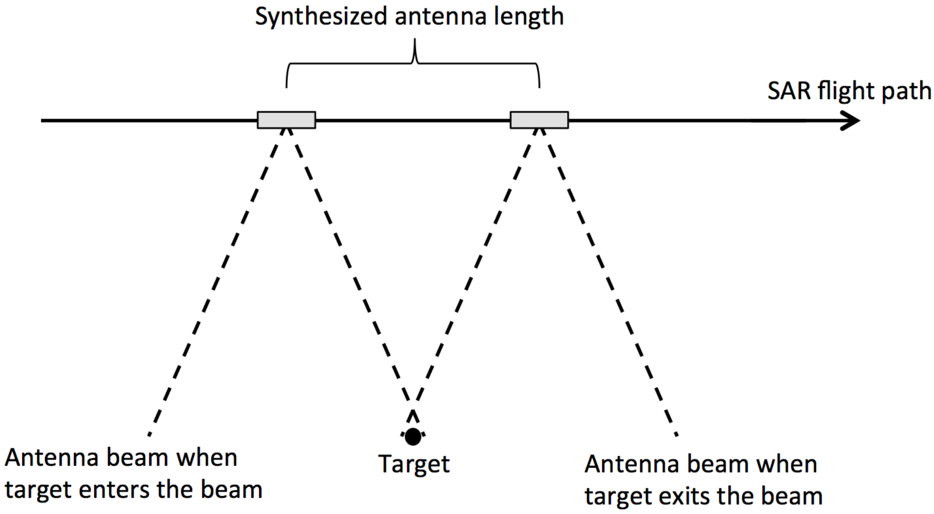

Figure 4.3: High azimuth resolution is achieved in a SAR sensor by using the forward motion of the sensor to synthesize a longer antenna. Figure adapted from [van Zyl and Kim, 2011].

is given as

$$r_a = \frac{d_a}{2}. \tag{4.3}$$

The r_a is independent of radar wavelength and sensor-surface distance and the resolution improves as the antenna length decreases. However, the resolution is limited by other factors related to application goals (e.g., area coverage and observation geometry) and technological limitations (e.g., data collection rate and volume, pulse power, phase control and calibration) [McCandless and Jackson, 2004, van Zyl and Kim, 2011]. The resolution given in (4.3) assumes a fixed antenna pointing direction with the SAR operating in the *stripmap* mode. Higher resolution can be obtained by steering the antenna (see Section 4.7.1) [Oliver and Quegan, 2004].

4.3 Speckle

A characteristic of SAR images is the grainy appearance caused by randomly distributed dark and bright pixels throughout the image. This "salt and pepper" appearance is referred to as *speckle*. In a SAR image of a distributed target, each resolution cell usually contains a large number of independent scatterers, and the speckle occur due to constructive and destructive interference between the many scattering events. Hence, speckle is an inherent property of SAR measurements, and can statistically be modeled as a random walk in the complex plane. Speckle can be considered as noise. However, it is not noise in the classic sense. As it is the radar signature of a point on the surface under the given circumstances, the speckle also carries information [McCandless and Jackson, 2004, Oliver and Quegan, 2004].

The speckle causes large variations in the SAR measurements, also within a uniform area. It complicates the image analysis, and reduces the effectiveness of image segmentation and classification techniques. Therefore, speckle is commonly reduced by the process of *multilooking*. Multilooking can be done during the image formation by dividing the full aperture into sub-apertures and averaging these, or it can be done in the spatial domain by averaging over a neighborhood of pixels. The standard deviation of the speckle is reduced proportionally to $\sqrt{L}$, when L is the number of independent looks [Massonnet and Souyris, 2008].

For a rough homogeneous surface with a large number of scatterers present within each resolution cell, the sum of the reflected waves can be assumed to have a phase uniformly distributed between $-\pi$ and π. This is referred to as *fully developed speckle*. From the central limit theorem, the real and imaginary parts of the sum are independently and identically Gaussian distributed with zero mean. Further, the amplitude of the signal will be Rayleigh distributed and the intensity will follow a gamma distribution [Oliver and Quegan, 2004, Lee and Pottier, 2009]. This is further addressed in Section 4.6.

4.4 Frequency

The frequency $v = 1/\lambda$ of the SAR signal, is very important for the interaction between the transmitted wave and the observed surface. As the frequency increases, the signal will interact with smaller surface elements, and the penetration depth will decrease. High frequency sensors are more sensitive to heavy rain, which can attenuate the signal and produce image artifacts. These processes are further discussed in Chapter 5.

The microwave frequency range is divided into several bands as shown in Table 4.1. The most commonly used frequency bands in SAR sensors are C-, X- and L-band. The effect of frequency on the imaging of oil spills is addressed in Paper III presented in Chapter 10.

Table 4.1: Microwave frequency bands [Moreira et al., 2013].

Frequency band	**Ka**	**Ku**	**X**	**C**	**S**	**L**	**P**
Frequency [GHz]	40 - 25	17.6 - 12	12 - 7.5	7.5 - 3.75	3.75 - 2	2 - 1	0.5 - 0.25
Wavelength [cm]	0.75 - 1.2	1.7 - 2.5	2.5 - 4	4 - 8	8 - 15	15 - 30	60 - 120

4.5 Polarimetry

An electromagnetic wave consists of electric and magnetic force fields that are orthogonal to each other and to the direction of travel. The wave *polarization* is thought of as the shape that the tip of the electric field would trace over time at a fixed point in space. In general, electromagnetic waves are elliptically polarized. Special cases include *linear* polarization,

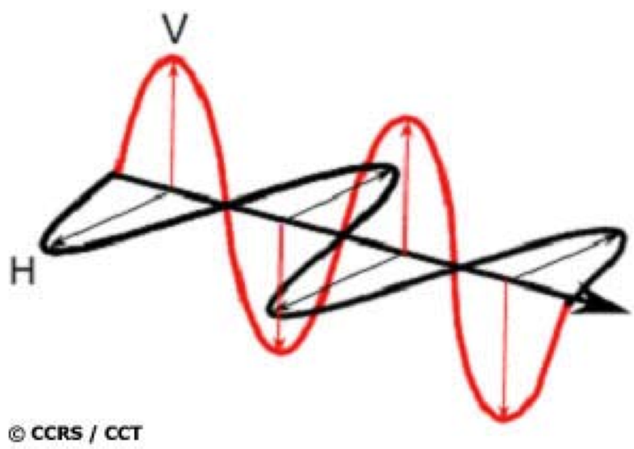

Figure 4.4: Electromagnetic waves with horizontal (H) and vertical (V) polarizations. Figure from [Canada Centre for Remote Sensing, 2007].

when the ellipse is reduced to a line, and *circular* polarization, when a circle is traced out. In traditional remote sensing systems, linear *horizontal* (H) and *vertical* (V) polarization (see Fig. 4.4) is applied [van Zyl and Kim, 2011].

The polarization of the transmitted SAR signal affects the interaction between the wave and the surface and hence the backscatter signal. Different transmit-receive polarization combinations (polarization channels) contain different information, and may be used in complement to characterize the observed surface. Which polarization channels that are measured vary between sensors and modes.

4.5.1 Polarization Diversity

The SAR polarization diversity is illustrated in Fig. 4.5. The simplest case is the *single-polarization* (mono-polarization) case where only one polarization is transmitted and received. In the case of *dual-polarized* systems, where two polarization channels are acquired, several variations exist. These include transmitting one polarization and receiving two orthogonal polarizations, or the transmission polarization may alternate to obtain two copolarized, orthogonal measurements. In some cases, the relative phase is also obtained. In the fully-polarized case, also referred to as *quadrature polarization* (quad-polarization), all four transmit-receive polarization combinations are obtained [Raney, 2011]. In the linear horizontal and vertical case, these are denoted HH, HV, VH and VV, in which the first and second letter indicates the polarization of the transmitted and received waves, respectively. Throughout this thesis, the term *multipolarization* refers to the combination of more than one polarization channel and *dual-copolarization* refers to the combination of HH and VV measurements.

In SAR polarimetry, measurements at different polarizations are used in combination to derive qualitative and quantitative physical information about the observed surface. A

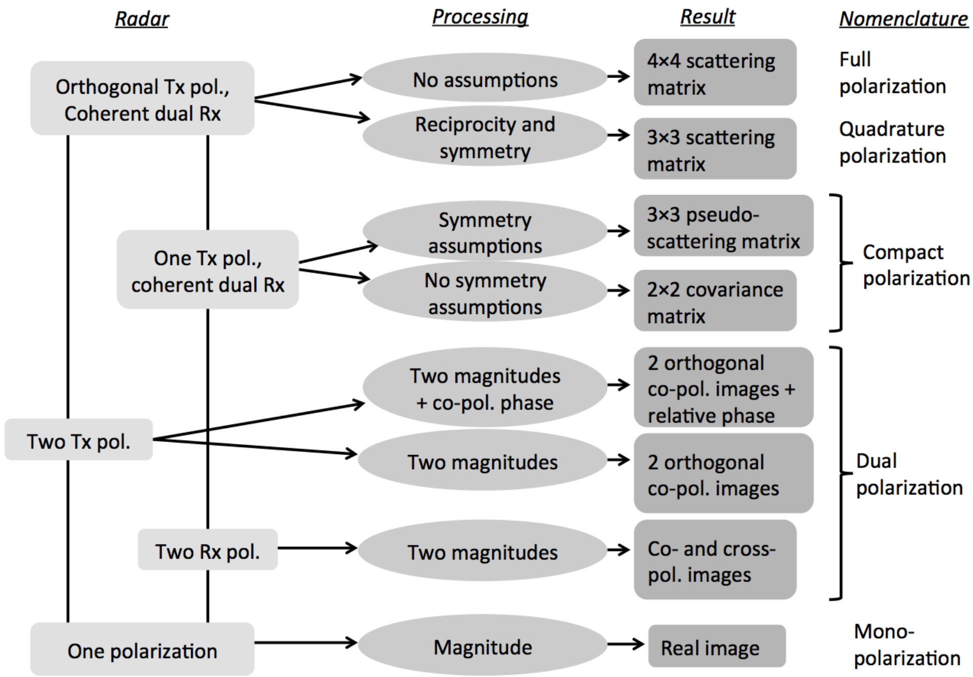

Figure 4.5: Polarization diversity of imaging radars. Figure adapted from [Raney, 2011].

thorough description of radar polarimetry and its application may be found in, e.g., [Touzi et al., 2004, Lee and Pottier, 2009, van Zyl and Kim, 2011]. In the next section, the most important and relevant concepts for our study are introduced.

4.5.2 Representation of Multipolarization Data

In a fully polarimetric SAR sensor, two orthogonally polarized pulses are transmitted separately, and the received signal in both components are measured. For each pixel, a matrix of *complex scattering coefficients* is produced, describing the scattering process that takes place at a given area on the ground. This *scattering matrix* **S** (also called the *Sinclair matrix*) relates the incident electric field E^i to the scattered electric field E^s by

$$\begin{bmatrix} E_p^s \\ E_q^s \end{bmatrix} = \frac{e^{-jkR}}{R} \begin{bmatrix} S_{pp} & S_{qp} \\ S_{pq} & S_{qq} \end{bmatrix} \begin{bmatrix} E_p^i \\ E_q^i \end{bmatrix}, \tag{4.4}$$

where $k = 2\pi/\lambda$ is the wave number. The orthogonal polarizations are indicated by p and q. The first and second subscript of the complex scattering coefficients refers to the transmit and receive polarization, respectively.

In the linear horizontal-vertical basis ($p, q \in \{H, V\}$), the 2×2 scattering matrix is written as

$$\mathbf{S} = \begin{bmatrix} S_{HH} & S_{VH} \\ S_{HV} & S_{VV} \end{bmatrix} = \begin{bmatrix} |S_{HH}|e^{j\phi_{HH}} & |S_{VH}|e^{j\phi_{VH}} \\ |S_{HV}|e^{j\phi_{HV}} & |S_{VV}|e^{j\phi_{VV}} \end{bmatrix}, \tag{4.5}$$

where $|S_{xx}|$ and ϕ_{xx} denote the amplitudes and the phases of the measured complex scattering coefficients. The diagonal elements are referred to as *copolarization* terms whereas the off-diagonal elements, which relate orthogonal polarizations, are denoted *cross-polarization* terms. In the case of monostatic systems, where the transmit and receive antennas are colocated, *reciprocity*, i.e., $S_{HV} = S_{VH}$, is often assumed [Oliver and Quegan, 2004, Lee and Pottier, 2009].

The scattering coefficients can be represented by scattering vectors. In the quad-polarization case, assuming reciprocity, the *Lexicographic scattering vector*, **l**, and the *Pauli scattering vector*, **k**, can be extracted from the scattering matrix as

$$\mathbf{l} = \left[S_{HH} \;\; \sqrt{2} S_{VH} \;\; S_{VV} \right]^T \tag{4.6}$$

and

$$\mathbf{k} = \frac{1}{\sqrt{2}} \left[S_{HH} + S_{VV} \;\;\; S_{HH} - S_{VV} \;\;\; 2S_{VH} \right]^T . \tag{4.7}$$

The superscript T denotes vector transpose. In the case of dual-copolarization measurements, which are applied in this thesis, the scattering vectors are reduced to

$$\mathbf{l} = [S_{HH} \;\; S_{VV}]^T \tag{4.8}$$

and

$$\mathbf{k} = \frac{1}{\sqrt{2}} \left[S_{HH} + S_{VV} \;\;\; S_{HH} - S_{VV} \right]^T . \tag{4.9}$$

The complex scattering coefficients are *single-look complex* (SLC) measurements. *Multilook complex* (MLC) data can be obtained through spatial multilooking. Two commonly applied MLC matrices are the *covariance matrix* **C** and the *coherency matrix* **T**, which are produced from **l** and **k**, respectively, as

$$\mathbf{C} = \frac{1}{L} \sum_{i=1}^{L} \mathbf{l}_i \mathbf{l}_i^{*T} \tag{4.10}$$

and

$$\mathbf{T} = \frac{1}{L} \sum_{i=1}^{L} \mathbf{k}_i \mathbf{k}_i^{*T}, \tag{4.11}$$

where $\mathbf{l}_i$ and $\mathbf{k}_i$ are the i^{th} single-look complex measurements, L is the number of samples included in the averaging and the superscript * is the complex conjugate. The **C** and **T** will be of size $d \times d$ when d is the polarimetric dimension [Lee and Pottier, 2009]. In the quad-polarization case ($d = 3$ when assuming reciprocity), **C** and **T** are given by

$$\mathbf{C} = \begin{bmatrix} \langle |S_{HH}|^2 \rangle & \sqrt{2} \langle S_{HH} S_{VH}^* \rangle & \langle S_{HH} S_{VV}^* \rangle \\ \sqrt{2} \langle S_{VH} S_{HH}^* \rangle & 2 \langle |S_{VH}|^2 \rangle & \sqrt{2} \langle S_{VH} S_{VV}^* \rangle \\ \langle S_{VV} S_{HH}^* \rangle & \sqrt{2} \langle S_{VV} S_{VH}^* \rangle & \langle |S_{VV}|^2 \rangle \end{bmatrix} \tag{4.12}$$

and

$$\mathbf{T} = \frac{1}{2}\begin{bmatrix} \langle |S_{HH}+S_{VV}|^2\rangle & \langle (S_{HH}+S_{VV})(S_{HH}-S_{VV})^*\rangle & 2\langle (S_{HH}+S_{VV})S_{VH}^*\rangle \\ \langle (S_{HH}-S_{VV})(S_{HH}+S_{VV})^*\rangle & \langle |S_{HH}-S_{VV}|^2\rangle & 2\langle (S_{HH}-S_{VV})S_{VH}^*\rangle \\ 2\langle S_{VH}(S_{HH}+S_{VV})^*\rangle & 2\langle S_{VH}(S_{HH}-S_{VV})^*\rangle & 4\langle |S_{VH}|^2\rangle \end{bmatrix} \quad (4.13)$$

where $\langle\cdot\rangle$ indicates ensemble averaging. The dual-copolarization ($d = 2$) versions are

$$\mathbf{C} = \begin{bmatrix} \langle |S_{HH}|^2\rangle & \langle S_{HH}S_{VV}^*\rangle \\ \langle S_{VV}S_{HH}^*\rangle & \langle |S_{VV}|^2\rangle \end{bmatrix} \quad (4.14)$$

and

$$\mathbf{T} = \begin{bmatrix} \langle |S_{HH}+S_{VV}|^2\rangle & \langle (S_{HH}+S_{VV})(S_{HH}-S_{VV})^*\rangle \\ \langle (S_{HH}-S_{VV})(S_{HH}+S_{VV})^*\rangle & \langle |S_{HH}-S_{VV}|^2\rangle \end{bmatrix}. \quad (4.15)$$

On the diagonal, the averaged intensity of each scattering vector component is found, whereas off-diagonal terms are the averaged cross correlations between the components.

4.5.3 Application of SAR Polarimetry

Polarimetry is a powerful tool in the analysis of radar imagery. It can be used to infer information on physical properties of the observed surfaces, e.g., related to surface roughness, geometry and dielectric properties. Polarimetric techniques can be used to develop physical models for identification and separation of scattering mechanisms within the same resolution cell. *Polarimetric target decompositions* are used to describe the scattering properties of distributed targets, and for interpretation and classification of SAR imagery. Many different decompositions exist, and they can be grouped into four main classes [Lee and Pottier, 2009]:

- decompositions based on dichotomy of the Kennaugh matrix[1], e.g., Huynen, Holm and Barnes, Yang,
- "model-based" decomposition of the covariance or coherency matrices, e.g., Freeman and Durden, Yamaguchi,
- decompositions using eigenvector or eigenvalue analysis of covariance or coherency matrices, e.g., Cloude, Holm, van Zyl, Cloude and Pottier,
- coherent decompositions of the scattering matrix, e.g., Krogager, Cameron, Touzi.

A comprehensive review of target decompositions are presented in, e.g., [Lee and Pottier, 2009]. The entropy (H)/anisotropy (A)/mean scattering angle ($\bar{\alpha}$) decomposition proposed by [Cloude and Pottier, 1997] will be presented in Section 5.5.1.

[1] The Kennaugh matrix relates the transmitted and received Stokes vectors and is described in, e.g., [Lee and Pottier, 2009].

A wide variety of applications for SAR polarimetry are found in the literature, including observation of land, snow, ice, ocean and urban areas. As several of the more recently available SAR sensors, as well as planned missions, offer dual- and quad-polarization acquisitions, polarimetric techniques may be of increasing relevance for SAR data analysis [Moreira et al., 2013]. A literature review on the application of multipolarization techniques for oil spill observation is given in Section 5.5.1. The use of multipolarization data for characterization of low backscatter ocean regions is one of the main topics of this thesis, and is discussed in the four papers presented in Chapters 8 - 11.

4.5.4 Compact Polarimetry

A more recently recognized polarization option is the *compact polarimetry* (CP), which encompasses the options that fall between dual-polarization and quad-polarization SARs. In this case, the signal is transmitted in one polarization and two orthogonal polarizations are received, including their relative phase. Several variations within the CP mode exist. In the $\pi/4$ mode, a linearly polarized field rotated at 45° is transmitted, and H and V are received. The hybrid compact mode transmits circularly polarized waves and receives in H and V. The motivation for the CP mode is to obtain backscatter measurements of comparable finesse as fully-polarized systems, while avoiding the disadvantages, e.g., the reduced scene size. Several recently launched and planned SAR systems have CP modes and their application seems to be increasingly discussed in the literature [Raney, 2011, Salberg et al., 2014].

4.6 Statistical Data Properties

A description of selected statistical properties is provided in this section, including an introduction to the product model and the Mellin kind statistics.

4.6.1 Speckle Distributions

If the single-look complex measurements introduced in Section 4.5.2 is written on the form $a + jb$, the *single-look intensity* (SLI) is given by $I = a^2 + b^2$. The *multilook intensity* (MLI) can be obtained by averaging over a sample of measurements

$$I = \frac{1}{L} \sum_{i=1}^{L} \left(a_i^2 + b_i^2 \right). \tag{4.16}$$

In the case of fully developed speckle introduced in Section 4.3, the intensity is gamma distributed, $I \sim \gamma(L, \sigma)$, i.e.,

$$f_I(I; L, \sigma) = \frac{L^L}{\Gamma(L)} \frac{I^{L-1}}{\sigma^L} \exp\left(-\frac{LI}{\sigma} \right), \tag{4.17}$$

where $\sigma = E\{I\}$ and $\Gamma(L)$ is the gamma function, $\Gamma(L) = \int_0^\infty u^{L-1}e^{-u}du$. In the case of SLI ($L = 1$) data, the distribution reduces to a negative exponential distribution [Lee and Pottier, 2009].

If $L \geq d$, the sample covariance matrix in (4.10) will follow a *scaled complex Wishart distribution*, $\mathbf{C} \sim s\mathcal{W}_d^{\mathbb{C}}(L, \mathbf{\Sigma})$, i.e.,

$$f_{\mathbf{C}}(\mathbf{C}; L, \mathbf{\Sigma}) = \frac{L^{Ld}}{\Gamma_d(L)} \frac{|\mathbf{C}|^{L-d}}{|\mathbf{\Sigma}|^L} \exp\left(\mathrm{tr}\left(-L\mathbf{\Sigma}^{-1}\mathbf{C}\right)\right), \tag{4.18}$$

where $|\cdot|$ and $\mathrm{tr}(\cdot)$ are the determinant and trace operator, respectively, $\mathbf{\Sigma} = E\{\mathbf{C}\}$ and $\Gamma_d(L)$ is the multivariate gamma function of the complex kind, $\Gamma_d(s) = \pi^{d(d-1)/2} \prod_{i=0}^{d-1} \Gamma(s-i)$ [Lee and Pottier, 2009].

4.6.2 Product Model

The randomness in a radar measurement is commonly attributed to two separate processes, i.e., the fully developed speckle, and the variation in the underlying radar cross section, referred to as *texture*. The Gaussian model described in the previous section only accounts for the speckle. Texture can be included implicitly by assuming non-Gaussian statistics for the scattering vectors, or explicitly by modeling the texture as a random variable. The latter case produces a doubly stochastic model with a compounded distribution [Anfinsen and Eltoft, 2011]. One such model, commonly used to describe non-Gaussian statistics, is the *product model* described in, e.g., [Oliver and Quegan, 2004], which expresses the SAR measurement as the product of the speckle and the texture variables. For the single-polarization intensity case

$$I = TS, \tag{4.19}$$

where S is the gamma distributed fully developed speckle and T is the scalar texture random variable with a positive only probability density function (pdf). In the MLC covariance matrix case, the product model can be expressed as

$$\mathbf{C} = T\widetilde{\mathbf{W}}, \tag{4.20}$$

where $\widetilde{\mathbf{W}}$ represents the speckle with a scaled complex Wishart distribution (assuming $L \geq d$) [Anfinsen and Eltoft, 2011]. The distributions of the measured I and $\mathbf{C}$ depend on the distribution of the texture variable. Possible distributions for this variable are given in the next section, and are thoroughly discussed in [Anfinsen, 2010, Anfinsen and Eltoft, 2011].

In this thesis, the deviation from Gaussian statistics in low backscatter ocean regions is investigated in terms of log-cumulants, which are defined next.

4.6.3 Mellin Kind Statistics

A statistical distribution can be characterized by its statistical moments and cumulants. In classical statistics, the *characteristic function* (CF) from which these are defined, is derived using the Fourier transform. [Nicolas, 2002, translated in [Nicolas and Anfinsen, 2012]] proposed to use the Mellin transform instead, which lead to the *Mellin kind characteristic function* and *Mellin kind moments and cumulants*, also referred to as *log-moments* and *log-cumulants*.

Univariate Case

In the univariate case, the Mellin kind characteristic function of a stochastic variable X defined on $\mathbb{R}^+$ is given as

$$\phi_X(s) = E\{X^{s-1}\} = \mathcal{M}\{f_X(x)\}(s), \tag{4.21}$$

where $\mathcal{M}\{\cdot\}(s)$ denotes the Mellin transform

$$\mathcal{M}\{f_X(x)\}(s) = \int_0^\infty x^{s-1} f_X(x) dx, \tag{4.22}$$

and $s \in \mathbb{C}$ is the complex transform variable. When the log-moments $M_\nu\{X\}$ exist, the CF can be expanded as

$$\phi_X(s) = \sum_{\nu=0}^{\infty} \frac{(s-1)^\nu}{\nu!} M_\nu\{X\}. \tag{4.23}$$

The ν^{th} order log-moments of X are then given by

$$M_\nu\{X\} = E\{(\ln X)^\nu\}. \tag{4.24}$$

The *sample log-moments* are computed from a collection of N samples as

$$\mu_\nu\{X\} = \frac{1}{N} \sum_{i=1}^{N} (\ln X_i)^\nu. \tag{4.25}$$

The *log-cumulants* are related to the log-moments, and the first three log-cumulants are obtained from

$$\kappa_1\{X\} = \mu_1\{X\}, \tag{4.26}$$

$$\kappa_2\{X\} = \mu_2\{X\} - \mu_1\{X\}^2 \tag{4.27}$$

and

$$\kappa_3\{X\} = \mu_3\{X\} - 3\mu_1\{X\}\mu_2\{X\} + 2\mu_1\{X\}^3 \tag{4.28}$$

and represent the mean, variance and skewness in the log-domain, respectively [Nicolas, 2002, Nicolas and Anfinsen, 2012, Anfinsen and Eltoft, 2011].

Matrix-variate Case

The Mellin kind statistics were expanded to the matrix-variate case in [Anfinsen, 2010, Anfinsen and Eltoft, 2011]. For a $d \times d$ complex Hermitian random matrix $\mathbf{Z}$ that are either positive definite, negative definite or null, the Mellin kind CF is

$$\phi_{\mathbf{Z}}(s) = E\{|\mathbf{Z}|^{s-d}\} = \mathcal{M}\{f_{\mathbf{Z}}(\mathbf{Z})\}(s). \tag{4.29}$$

The Mellin transform is

$$\mathcal{M}\{f_{\mathbf{Z}}(\mathbf{Z})\}(s) = \int_{\Omega_+} |\mathbf{Z}|^{s-d} f_{\mathbf{Z}}(\mathbf{Z}) d\mathbf{Z}, \tag{4.30}$$

where Ω_+ is the cone of positive definite Hermitian matrices. When the *matrix log-moments* $M_\nu\{\mathbf{Z}\}$ exist, the CF can be expanded as

$$\phi_{\mathbf{Z}}(s) = \sum_{\nu=0}^{\infty} \frac{(s-d)^\nu}{\nu!} M_\nu\{\mathbf{Z}\}, \tag{4.31}$$

and the matrix log-moment of ν^{th} order is retrieved from

$$M_\nu\{\mathbf{Z}\} = E\{(\ln|\mathbf{Z}|)^\nu\}. \tag{4.32}$$

The *sample matrix log-moments* are computed from a collection of N covariance matrices as

$$\mu_\nu\{\mathbf{C}\} = \frac{1}{N} \sum_{i=1}^{N} (\ln|\mathbf{C}_i|)^\nu. \tag{4.33}$$

The *matrix log-cumulants* can be obtained from the matrix log-moments in the same way as for the univariate case, and the first three are given as [Anfinsen and Eltoft, 2011]

$$\kappa_1\{\mathbf{C}\} = \mu_1\{\mathbf{C}\}, \tag{4.34}$$

$$\kappa_2\{\mathbf{C}\} = \mu_2\{\mathbf{C}\} - \mu_1\{\mathbf{C}\}^2 \tag{4.35}$$

and

$$\kappa_3\{\mathbf{C}\} = \mu_3\{\mathbf{C}\} - 3\mu_1\{\mathbf{C}\}\mu_2\{\mathbf{C}\} + 2\mu_1\{\mathbf{C}\}^3. \tag{4.36}$$

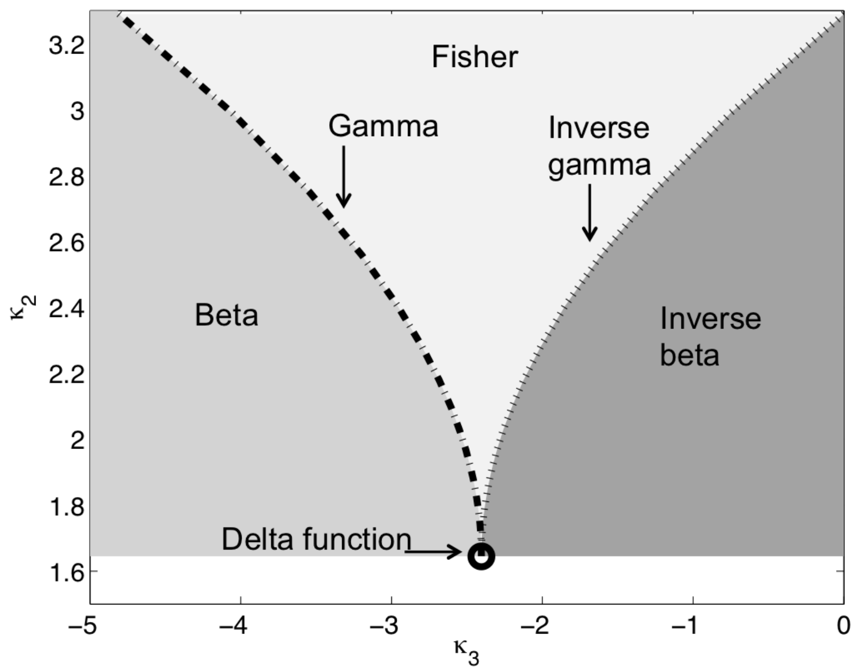

Figure 4.6: Example of a log-cumulant diagram with texture distributions indicated.

Log-cumulant Diagram

The *log-cumulant diagram*, where the second- and third-order log-cumulants, κ_2 and κ_3, are plotted against each other, is a visualization tool that can be used to compare data with distribution models [Anfinsen and Eltoft, 2011, Bombrun et al., 2011]. An example is given in Fig. 4.6, with the span of some texture models in the κ_2 - κ_3 space indicated.

The dimension of the area covered by a given texture model in Fig. 4.6 is equal to the number of free parameters in the model. The circle at the intersection of the distributions indicates the point where the texture distribution is a delta function, i.e., where no textural variation is present and Gaussian statistics are in place. The *Gamma* and *Inverse Gamma* distributions each have one texture parameter, and are represented by curves in the diagram. The *Fisher*, *Beta* and *Inverse Beta* distributions have two texture parameters and are represented by surface regions. κ_2 and κ_3 affect the shape of the distributions. More heavy-tailed distributions are found with increasing κ_2.

In Paper III and Paper IV, presented in Chapter 10 and Chapter 11, log-cumulants are investigated for SLI and MLC data, respectively.

4.7 Spaceborne SAR Sensors

The initial development of SAR systems in the 1950s and 1960s was mainly for military purposes. Several airborne systems for civilian applications emerged in the 1970s and 1980s, and the first civilian satellite-borne SAR sensor, SEASAT, was launched in 1978. More

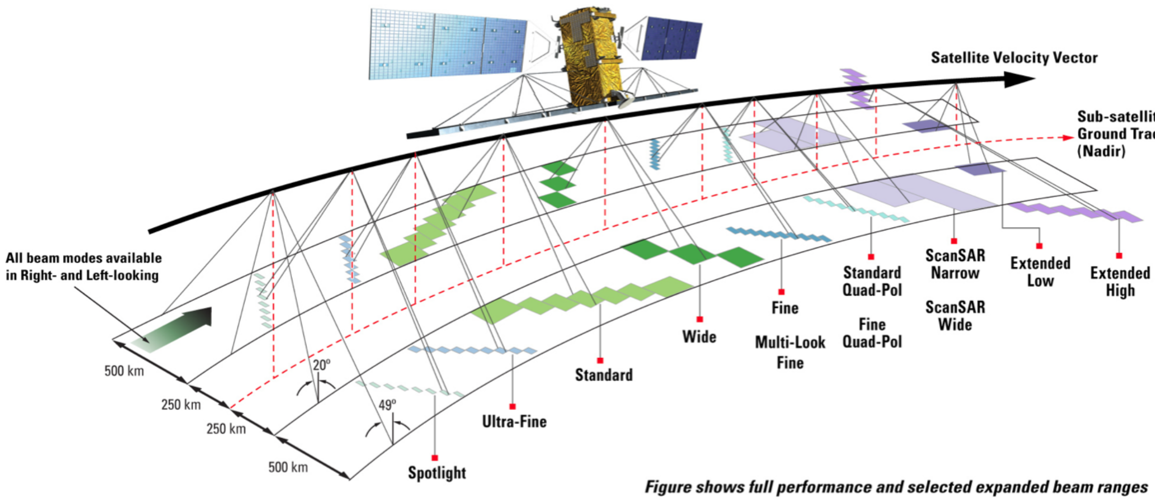

Figure 4.7: Radarsat-2 modes of operation. Figure from [MacDonald, Dettwiler and Associates Ltd., 2009] reproduced by permission of MacDonald, Dettwiler and Associates Ltd.

advanced SAR technologies were developed in the 1980s and 1990s, including polarimetry, interferometry and differential interferometry [Moreira et al., 2013].

A significant increase in the number of spaceborne SAR missions was experienced in the 1990s with the launches of the European Remote Sensing Satellite (ERS)-1/2 (1991 - 2000/1995 - 2011), the Japanese Earth Resources Satellite (J-ERS)-1 (1992 - 1998), and the Canadian Radarsat-1 (1995 - 2013). Each of these was operating at a single frequency and polarization [McCandless and Jackson, 2004]. The Shuttle Imaging Radar-C and X-band Synthetic Aperture Radar (SIR-C/X-SAR) became the first fully-polarimetric spaceborne SAR when it was flown aboard the space shuttle *Endeavour* by the National Aeronautics and Space Administration (NASA) in 1994 [Lee and Pottier, 2009]. The Environmental Satellite (ENVISAT) (2002 - 2012), operated by the European Space Agency (ESA) had an alternating polarization mode which provided dual-polarization measurements, but without useful phase information. The first operational quad-polarization satellite sensor was the Japanese Advanced Land Observing Satellite (ALOS) phased array type L-band SAR (PALSAR) (2006 - 2011) [Lee and Pottier, 2009]. Since 2007, a number of sensors with multipolarization capabilities have been launched. An overview of the currently operational SAR sensors, and some planned missions, are given in Table 4.2. More detailed information on the specific sensors and modes applied in this thesis is provided in Chapter 6.

4.7.1 Modes of Operation

SAR sensors can operate in different modes by varying the antenna radiation pattern. In the *stripmap* mode, which is the most fundamental, the antenna pattern is fixed to one swath, and one continuous strip on the surface is measured. To obtain a wider swath, the *scanSAR*

Table 4.2: Overview of currently operational and planned SAR sensors [Moreira et al., 2013, Earth Observation Portal, 2014]. 'Exp.' and 'Sched.' denote experimental and scheduled, respectively.

Sensor[a]	**Launch year**	**Freq. band**	**Polarization**	**Owner/operator**[b] **(country)**	**Other information**
TerraSAR-X TanDEM-X	2007-2010	X-band	Dual (exp. quad)	DLR/Astrium (Germany)	First spaceborne bistatic radar
Radarsat-2	2007	C-band	Quad	CSA (Canada)	
COSMO-SkyMed (1-4)	2007-2010	X-band	Dual	ASI/MoD (Italy)	Constellation of four satellites
RISAT-1	2012	C-band	Quad	ISRO (India)	Follow-on planned
HJ-1C	2012	S-band	Single	CRESDA/CAST	Constellation of four satellites
Kompsat-5	2013	X-band	Dual	KARI (Korea)	
ALOS-2	2014	L-band	Quad (exp. CP)	JAXA (Japan)	
Sentinel-1a/1b	2014/ Sched. 2016	C-band	Dual	ESA (Europe)	Constellation of two satellites
PAZ	Sched. 2014	X-band	Dual	CDTI (Spain)	Constellation with TerraSAR-X/ TanDEM-X
Radarsat Constellation	Sched. 2016	C-band	Quad, CP	CSA (Canada)	Constellation of three satellites
SAOCOM	Sched. 2014/2015	L-band	Quad	CONAE (Argentina)	Constellation of two satellites
TerraSAR-X Next Generation	Sched. 2016	X-band	Quad	Astrium (Germany)	Constellation with TerraSAR-X/ TanDEM-X

[a] TanDEM-X: TerraSAR-X add-on for Digital Elevation Measurement, RISAT: Radar Imaging Satellite, HJ-1C: Huan Jing-1C, Kompsat-5: Korea Multi-Purpose Satellite-5, SAOCOM: Argentine Microwaves Observation Satellite.

[b] DLR: German Aerospace Center, CSA: Canadian Space Agency, ASI: Italian Space Agency, MoD: Italian Ministry of Defense, ISRO: Indian Space Research Organization, CRESDA: China Centre for Resources Satellite Data and Application, CAST: Chinese Academy of Space Technology, KARI: Korea Aerospace Research Institute, JAXA: Japan Aerospace Exploration Agency, ESA: European Space Agency, CDTI: Spain's Center for Development of Industrial Technology, CONAE: Argentina National Space Activities Commission.

mode can be applied. In this mode, the antenna is steered to different elevation angles corresponding to multiple subswaths. The azimuth resolution for scanSAR is not as good as in the stripmap mode. A third option is the *spotlight* mode, where the antenna pattern is steered to a fixed point on the surface, increasing the illumination time and the azimuth resolution. However, individual regions on the ground rather than a continuous strip are recorded [Cumming and Wong, 2005]. The various modes of Radarsat-2 are illustrated in Fig. 4.7.

Chapter 5

SAR Remote Sensing of Oil Spills

This chapter describes the detection and characterization of oil spills and other low backscatter regions in the marine environment using SAR.

5.1 Ocean Monitoring by SAR

Satellite based remote sensing allows us to study the world's oceans from a very privileged viewpoint, enabling measurements with global coverage that are spatially detailed and regularly repeated. The radar technology has reached an operational stage, and is used as the main source of information for, e.g., oceanographic and meteorological research, climate research, weather forecasting, ship routing, pollution monitoring and tracking of coastal bathymetric changes [Gade et al., 2013]. SAR data are used to measure and monitor a variety of different ocean parameters and phenomena, including the wave field, wind speed and direction, surface currents, eddies, thermal fronts and internal waves. It is also used for ship detection, detection and characterization of sea ice and mapping of ice deformation and movement, and for identifying the presence of biogenic slicks and oil spills.

The independency of light and weather conditions, together with the wide coverage, the possibility of observing remote areas, the relatively low cost and the continuous data acquisition, make SAR sensors very useful for oil spill detection. Satellite SAR is used in combination with aircraft surveillance flights, which are needed to verify an oil spill and identify the polluter [Solberg and Brekke, 2008]. Satellite SAR imagery are used to monitor marine oil pollution for several applications [Ferraro et al., 2006]:

- to support in response operations when an accidental oil spill has taken place, providing information on, e.g., spill position, area, drift and spreading,
- to provide an early-warning of possible threats to coastal regions,
- to detect illegal discharges,
- to measure the state of the seas (e.g., means, variations and trends) to inform policymaking and assess the effects of implemented actions.

Recent reviews on the use of SAR data for oil spill observation can be found in [Solberg, 2012, Caruso et al., 2013]. Observation of accidental oil spills in SAR imagery has been investigated in many studies, see, e.g., [Girard-Ardhuin et al., 2005, Palenzuela et al., 2006, Ivanov, 2010, Kim et al., 2010, Frate et al., 2011, Jones et al., 2011a, Zhang et al., 2011, Minchew et al., 2012, Caruso et al., 2013, Migliaccio and Nunziata, 2014].

SAR data have been used in regional monitoring campaigns to map the extent of oil pollution in various parts of the world. In [Gade and Alpers, 1999], 660 ERS-2 images acquired from December 1996 to September 1998 over the southern Baltic Sea, the North Sea and the Gulf of Lion in the Mediterranean Sea were analyzed. A total of 675 spills were detected, with the most polluted areas found along the major shipping routes. A higher number of spills were detected in the morning passes than in the evening passes, as oil were often released during the night. A higher number of detections were done during summer compared to winter. This was attributed to the lower mean wind speed in the summer time, and hence better conditions for detecting slicks [Gade and Alpers, 1999]. The dimension of illegal pollution from operational discharges in the Mediterranean Sea was documented in [Pavlakis et al., 2001]. About 22% of the oil and refined products are transported through this area, which is particularly vulnerable to pollution due to the long cycle of water renewal. Visual inspection of 1600 ERS-1/2 SAR images acquired during 1999 resulted in 1638 detected spills. In 44% of the images, at least one oil spill was detected [Pavlakis et al., 2001]. A study of 1500 SAR images from the North Sea acquired during year 2000 resulted in 520 detected spills [Ferraro et al., 2006]. A number of similar studies have been carried out for the seas around Europe, see, e.g., [Ferraro et al., 2009] and references therein. A summary of the long-term remote sensing studies, mapping the extent of oil pollution in the European seas, was presented in [Ferraro et al., 2009]. They found that the operational oil pollution seemed to be decreasing.

Operational oil spill detection services carried out by, e.g., Kongsberg Satellite Services (KSAT) in Tromsø, Norway, are based on SAR imagery. Potential spills are detected and information on, e.g., the position, size, shape and contrast are derived. A confidence level is set for the detection, and the information is provided to the coast guard, oil companies or other appropriate authorities. Subsequently, an aircraft may be sent to the area for further investigation. KSAT is a service provider for CleanSeaNet (see Section 2.5). In CleanSeaNet, an area of 1000 million km^2 is monitored, and from April 2007 to January 2011, an average of 2000 SAR images were analyzed per year. Fig. 5.1 gives an overview of the satellite coverage and the distribution of possible spills detected in this period. The average number of possible spills per image has been decreasing from 1.38 in 2008 to 1.0 in 2009 and 0.75 in 2010 [European Maritime Safety Agency, 2011].

5.2 Sea Surface Scattering

When an EM wave transmitted by a SAR sensor encounters the sea surface, *surface scattering* takes place. The scattering depends on the EM wave properties, the surface properties and the environmental conditions. The effect of various properties on the backscatter and

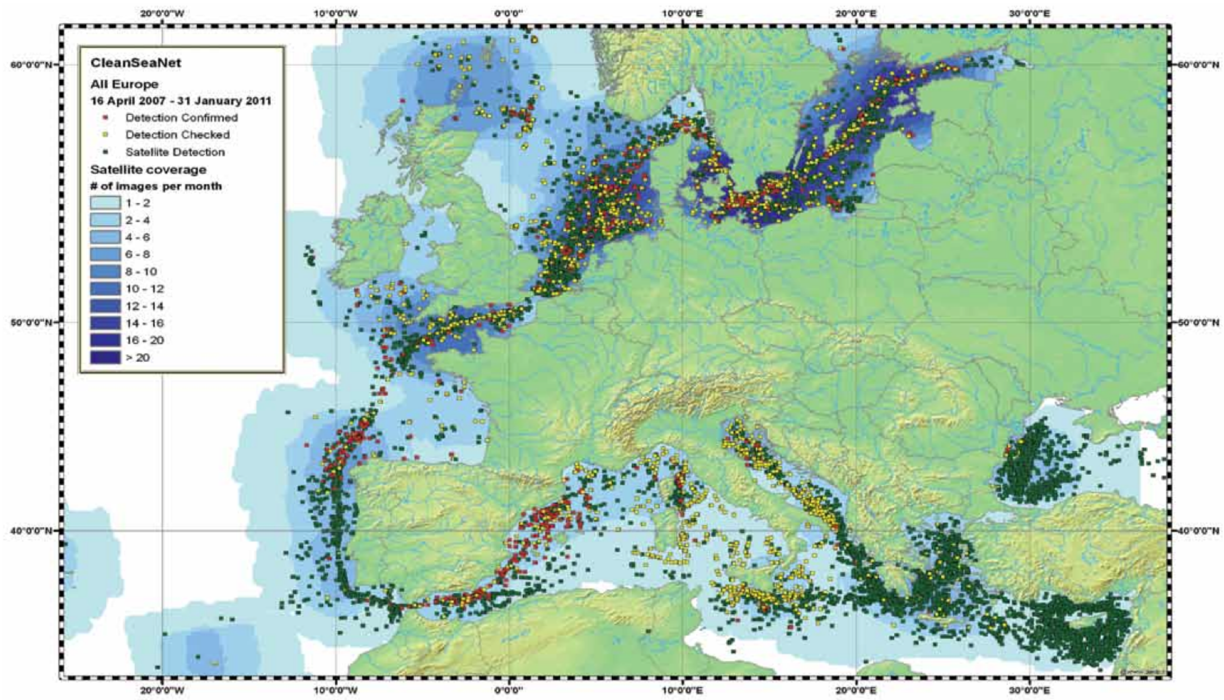

Figure 5.1: Satellite coverage and location of detections by the CleanSeaNet 16 April 2007 - 31 January 2011. Figure from [European Maritime Safety Agency, 2011].

selected scattering models are described in the following sections.

5.2.1 Surface Roughness

The scattering of EM waves from a surface is affected by the surface geometry and the dielectric properties. The relation between surface roughness and scattering is illustrated in Fig. 5.2. For a smooth surface (Fig. 5.2(a)), the angular pattern of the reflected radiation is a delta function centered in the specular direction. No backscatter would occur at this surface. For the slightly rough surface (Fig. 5.2(b)), the angular radiation pattern has two components. One reflection component in the specular direction (with a smaller magnitude than in the smooth case), which is referred to as the *coherent* scattering component. The second component, called the *diffuse* or *noncoherent* component, consists of scattering in all directions. As the roughness increases, the coherent part becomes negligible. For a very rough surface (Fig. 5.2(c)), the radiation pattern approaches that of a Lambertian surface, with only diffuse scattering. Rough surfaces hence produce more radar backscatter [Ulaby et al., 1986a].

The effect of the roughness on the EM wave scattering depends on the wavelength with which the surface is observed. A surface that appears rough to one wave may appear smooth to a wave with a different wavelength. The roughness of a surface must therefore be assessed relative to the radar wavelength. Two parameters typically used for characterizing

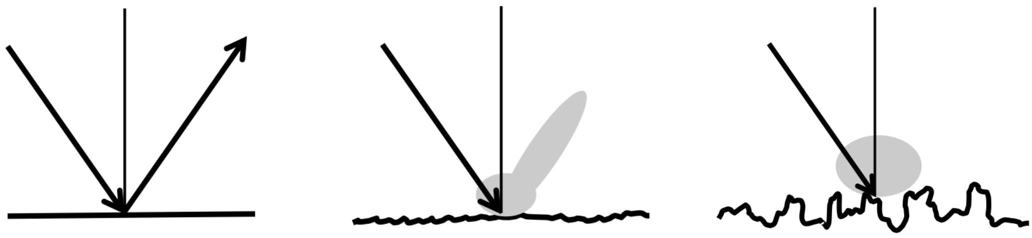

(a) Smooth surface. (b) Slightly rough surface. (c) Very rough surface.

Figure 5.2: Scattering from surfaces of varying roughness conditions. Figure adapted from [Ulaby et al., 1986a]

roughness are the *standard deviation of the surface height (rms height)*, h, and the *surface correlation length*, which describe the vertical and horizontal roughness, respectively [Ulaby et al., 1986a]. The *Rayleigh criterion* states that a surface may be considered smooth if the phase difference between two reflected rays is less than $\pi/2$ radians. This leads to the following requirement

$$h < \frac{\lambda}{8\cos\theta}. \tag{5.1}$$

The Rayleigh criterion is a useful first-order classifier of smoothness, but a stricter criterion is needed for modeling microwave scattering from natural surfaces, as the wavelength is usually on the order of h. The *Fraunhofer criterion* may be used, where

$$h < \frac{\lambda}{32\cos\theta} \tag{5.2}$$

is required for a surface to be considered smooth [Ulaby et al., 1986a].

5.2.2 Dielectric Properties

In addition to the roughness, the dielectric properties of the surface can affect the interaction between the wave and the surface and hence the backscatter signal. The *complex electric permittivity* is given as

$$\epsilon(\omega) = \epsilon'(\omega) - j\epsilon''(\omega), \tag{5.3}$$

where $\epsilon'(\omega)$ is the real part, $\epsilon''(\omega)$ is the imaginary part, $j = \sqrt{-1}$ and $\omega = 2\pi v$ is the angular frequency of the incident wave with ordinary frequency v [Hz]. The *relative permittivity* ϵ_r is the ratio between the material permittivity and the permittivity of vacuum ϵ_0, i.e., $\epsilon_r(\omega) = \epsilon(\omega)/\epsilon_0$. The term *dielectric constant* has been used interchangeably with the electric permittivity and also to refer to the real part of the *relative permittivity*, ϵ_r' [Woodhouse, 2006]. The term *relative dielectric constant* is here used to describe the complex ϵ_r. The backscatter signal increases with increasing dielectric constant [Ulaby et al., 1986a].

The dielectric properties of the surface affect how far into the sea water column the SAR signal can penetrate. The *penetration depth* δ_p is defined as the depth where the power of the propagating electric field is attenuated by a factor $1/e$, and is defined as

$$\delta_p = -\frac{1}{2k\,\Im\left(\sqrt{\epsilon_r}\right)}, \tag{5.4}$$

where $\Im$ denotes the imaginary part [Massonnet and Souyris, 2008].

5.2.3 Scattering Models

In addition to the surface properties described above, a number of other factors also affect the radar backscatter from ocean surfaces. These include environmental conditions (e.g., wind speed and direction relative to the radar beam) and sensor parameters (e.g., incidence angle, polarization and frequency).

An increase in wind speed results in a rougher surface and a stronger backscatter signal. The dependency of the backscatter on the horizontal angle between the radar look direction and the upwind direction is a function of incidence angle, wind speed and polarization. Maximum signal is received if the radar looks in the upwind direction, and smaller signals occur when looking downwind. A minimum in the backscatter is observed if the radar looks in the direction normal to the wind direction [Ulaby et al., 1986a]. The ocean backscatter is known to decrease with increasing incidence angle. Stronger signals are obtained in VV compared to HH and the difference increases with incidence angle and the relative dielectric constant [Valenzuela, 1978]. The cross-polarization channels usually lie around 5 dB below HH, and are often near or below the sensor noise floor (see Section 5.4.4) [Holt, 2004].

For irregular surfaces, such as the sea surface, no exact closed-form solutions describing the scattering exist. Numerical techniques can be used for computation of exact solutions, but these methods are generally computationally prohibitive. Hence, approximate analytic solutions with assumptions on the dimensions of the scattering elements are often used in practical applications. In many cases, they are used effectively, but their validity is restricted to a limited range of surface conditions. The scattering from sea surfaces is described in, e.g., [Valenzuela, 1978]. For typical SAR incidence angles, the scattering is commonly described using the *Bragg scattering model* (small perturbation model), which is introduced next.

Bragg Scattering

The ocean surface contains a spectrum of waves, from short ripples of a few millimeters to waves of hundreds of meters long. In absence of long waves, the ocean backscatter within typical SAR incidence angles ($\sim$18° - 50°) is dominated by Bragg or resonance scattering. The backscatter arises from wave components that are in resonance with the incident waves, i.e., the small capillary and short gravity waves [Holt, 2004].

When an incoming EM wave with wavelength λ reaches the sea surface, the transmitted signal hits each successive surface crest at a slightly different time. If the excess distance from the radar to each crest is $\lambda/2$ (or a multiple of this), the phase difference between the return signals from each crest is 360°, and the signals add in phase. Otherwise, they add out of phase. The Bragg wavelength, λ_B, of ocean waves resulting in resonance is hence given by

$$\lambda_B = \frac{n\lambda}{2\sin\theta}, \tag{5.5}$$

where $n = 1, 2, ...$ is the order of resonance ($n = 1$ produces the dominant return) [Ulaby et al., 1986a]. From (5.5) it is evident that for a given λ, the resonant waves are shorter at more oblique incidence angles, and at a given θ, λ_B increases with radar wavelength.

The first order ocean backscatter coefficients in the Bragg model are given by [Valenzuela, 1978]

$$\sigma_0^{pq}(\theta) = 4\pi k^4 \cos^4\theta |g_{pq}(\theta)|^2 W(2k\sin\theta, 0), \tag{5.6}$$

where $W(\cdot)$ is the two-dimensional wave number spectral density of the surface roughness and the indices p and q denote the polarization of the incident and backscattered radiation, respectively. The first-order scattering coefficients $g_{pq}(\theta)$ are given as [Valenzuela, 1978]

$$g_{HH}(\theta) = \frac{(\epsilon_r - 1)}{\left(\cos\theta + \sqrt{\epsilon_r - \sin^2\theta}\right)^2} \tag{5.7}$$

and

$$g_{VV}(\theta) = \frac{(\epsilon_r - 1)[\epsilon_r(1 + \sin^2\theta) - \sin^2\theta]}{\left(\epsilon_r\cos\theta + \sqrt{\epsilon_r - \sin^2\theta}\right)^2}. \tag{5.8}$$

Cross-polarization returns are zero. It is seen from (5.6) that only g_{pq} depends on the polarization, hence $\sigma_0^{HH}/\sigma_0^{VV} = g_{HH}/g_{VV}$. This ratio depends only on θ and ϵ_r, and is independent of surface roughness. It can hence be used to evaluate the dielectric properties of a surface. If second order terms are included, depolarization effects are introduced and the cross-polarization terms are no longer zero [Valenzuela, 1967].

Tilted Bragg Scattering

The Bragg scattering model in general is incomplete for describing ocean surface backscatter. Longer ocean waves interact with the smaller Bragg waves and affect the radar backscatter through tilt modulation, hydrodynamic modulation and velocity bunching. Hence, the two-scale or composite models, where these interactions are accounted for, are more representative scattering models [Holt, 2004].

In the tilted Bragg model, the surface is assumed to be made up of an infinitely number of slightly rough patches. Due to the presence of long gravity waves, the normal to the facet deviates from the vertical by an angle Ψ in the plane of incidence and by an angle ζ in the plane perpendicular to the plane of incidence. The incidence angle for the tilted facet is

$$\theta_i = \cos^{-1}[\cos(\theta + \Psi)\cos\zeta], \tag{5.9}$$

and the resulting backscatter coefficients for each patch are given by [Valenzuela, 1978]

$$\sigma_0^{HH}(\theta_i) = 4\pi k^4 \cos^4\theta_i \left| \left(\frac{\sin(\theta+\Psi)\cos\zeta}{\sin\theta_i}\right)^2 g_{HH}(\theta_i) + \left(\frac{\sin\zeta}{\sin\theta_i}\right)^2 g_{VV}(\theta_i) \right|^2 \\ \times W(2k\sin(\theta+\Psi), 2k\cos(\theta+\Psi)\sin\zeta), \quad (5.10)$$

$$\sigma_0^{VV}(\theta_i) = 4\pi k^4 \cos^4\theta_i \left| \left(\frac{\sin(\theta+\Psi)\cos\zeta}{\sin\theta_i}\right)^2 g_{VV}(\theta_i) + \left(\frac{\sin\zeta}{\sin\theta_i}\right)^2 g_{HH}(\theta_i) \right|^2 \\ \times W(2k\sin(\theta+\Psi), 2k\cos(\theta+\Psi)\sin\zeta) \quad (5.11)$$

and

$$\sigma_0^{VH}(\theta_i) = \sigma_0^{HV}(\theta_i) = 4\pi k^4 \cos^4\theta_i \left(\frac{\sin(\theta+\Psi)\sin\zeta\cos\zeta}{\sin^2\theta_i}\right)^2 \times |g_{VV}(\theta_i) - g_{HH}(\theta_i)|^2 \\ \times W(2k\sin(\theta+\Psi), 2k\cos(\theta+\Psi)\sin\zeta). \quad (5.12)$$

Again, the ratios between the cross sections are only functions of the surface slope, the incidence angle and the dielectric constant.

Inclusion of a Non-Bragg Scattering Component

It is recognized that even when using the composite models, it has been difficult to obtain consistent characterization of the sea surface backscatter over a range of frequencies, incidence angles, polarizations and weather conditions. Particularly, it has been more difficult to obtain consistency between models and observations in HH compared to VV. Inclusion of a *non-Bragg* component has been shown to improve the correspondence between models and measurements [Kudryavtsev et al., 2003, Johnsen et al., 2008].

In [Kudryavtsev et al., 2013], the radar cross section (on linear scale) was represented as the sum of one polarized scattering component associated with conventional two-scale Bragg scatter, σ_{0B}^{pp}, and one *nonpolarized* (NP) scattering component due to non-Bragg scattering, σ_{0nB}, i.e.,

$$\sigma_0^{pp} = \sigma_{0B}^{pp} + \sigma_{0nB}, \quad (5.13)$$

where p is the polarization of the transmitted and received waves. The NP component is assumed to be the same for both polarizations, and can in theory be removed by computing the *polarization difference* (PD)

$$\text{PD} = \sigma_0^{VV} - \sigma_0^{HH} = \sigma_{0B}^{VV} - \sigma_{0B}^{HH}. \quad (5.14)$$

PD is controlled by the surface roughness produced by wave components close to the Bragg wave number, and should reveal near-surface wind variability and presence of slicks [Kudryavtsev et al., 2013]. The NP component is expressed as

$$\mathrm{NP} = \sigma_{0nB} = \sigma_0^{VV} - \mathrm{PD}/(1 - p_B), \tag{5.15}$$

where $p_B = \sigma_{0B}^{HH}/\sigma_{0B}^{VV}$ is the polarization ratio for the two-scale Bragg scattering model [Kudryavtsev et al., 2013]. NP is interpreted to be caused by wave breaking from steep and rough patches on the surface [Kudryavtsev et al., 2013] and other phenomena that can cause non-Bragg scattering. Finally, the *polarization ratio* (PR) is defined as

$$\mathrm{PR} = \frac{\sigma_0^{HH}}{\sigma_0^{VV}} = \frac{\sigma_{0B}^{HH} + \sigma_{0nB}}{\sigma_{0B}^{VV} + \sigma_{0nB}}. \tag{5.16}$$

The three parameters PD, NP and PR have been used to analyze the scattering from a sea surface, including oil-covered regions, in [Kudryavtsev et al., 2013]. PD and NP contain information about the Bragg and non-Bragg scattering mechanisms, respectively, and PR were used to evaluate the departure from Bragg scattering [Kudryavtsev et al., 2013]. This model is investigated in Paper III (given in Chapter 10), in which the relative contribution of σ_{0B}^{pp} and σ_{0nB} to the total backscatter is evaluated for clean sea and low backscatter ocean regions of various origin.

5.3 Detection of Oil Spills

The surface properties described in Section 5.2 are altered when an oil film is present. These effects, as well as the scheme for oil spill detection by SAR, are described in this section.

5.3.1 Effects of Oil Spills on the Surface Properties

An oil slick can be seen in a SAR image as a dark patch, i.e., an area of reduced backscatter compared to the surrounding clean sea. An example of a Radarsat-2 image is presented in Fig. 5.3. One plant oil slick and several releases of mineral oil (emulsion) are clearly seen as dark regions in the image. The SAR scene is acquired during an oil-on-water exercise in the North Sea, which is further described in Chapter 6.

The radar backscatter is reduced over an oil slick mainly because the oil film dampens the small surface waves and produces a smoother surface. This is clearly seen in Fig. 5.4, where the oil-covered surface close to the boom is much smoother compared to the surrounding sea. The damping of waves due to the presence of slicks is more thoroughly described in, e.g., [Alpers and Hühnerfuss, 1988, Gade et al., 1998].

A second mechanism that can reduce the radar backscatter from oil-covered surfaces is a change in the dielectric constant. Over the frequency range 0.1 to 10 GHz, the relative dielectric constant of sea water (salinity 32.54 ‰) has a real component greater than ∼40 at a temperature of 0°C and greater than ∼55 at 20°C. The absolute value of the imaginary

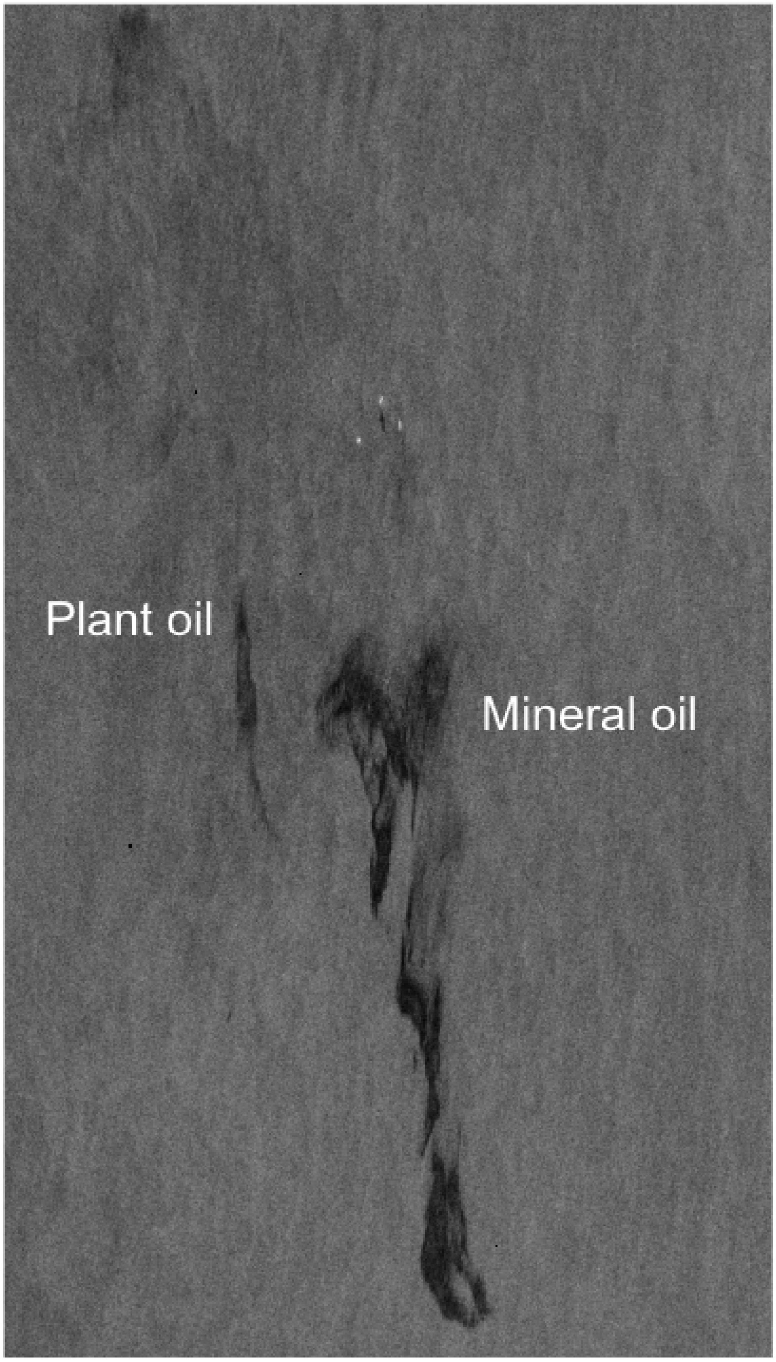

Figure 5.3: Radarsat-2 fine quad-polarization image from 15 June 2012, 06.20 UTC, containing slicks of various origin. RADARSAT-2 Data and Products ©MDA LTD. (2012) - All Rights Reserved.

Figure 5.4: A smoother surface is seen close to the boom where the oil is collected because the oil dampens the small surface waves. Photo: Stine Skrunes.

component is greater than ∼40 and ∼30 for 0°C and 20°C, respectively [Ulaby et al., 1986b]. In the same frequency range, biogenic and mineral oils have real components in the range 2.2 - 2.35 and imaginary components less than 0.02 [Folgerø, 1996, Minchew et al., 2012]. Hence, an oil film can change the dielectric constant of the topmost sea layer. However, the ability of a SAR sensor to detect changes in the dielectric constant due to the presence of oil depends on the thickness of the oil layer relative to the radar wavelength and the penetration depth. The typical thickness of a mineral oil spill is in the μm - mm range, or possibly cm range for freshly spilled oil [Hühnerfuss, 2006]. The thinner oil slicks are not thick enough for the SAR to detect changes in the dielectric constant. In the case of a sufficiently thick layer of oil, or if oil is mixed with water in high enough concentrations in a layer below the surface, the reduction in effective dielectric constant can lead to a decrease in backscattered energy. This was addressed in [Minchew, 2012], where a method for decoupling the effects of reduced dielectric constant and the damping of surface waves was described. In [Franceschetti et al., 2002], a simulation of SAR signals from marine oil slicks was presented. They found that the oil dielectric constant did not significantly modify the electromagnetic return, mainly due to the low slick thickness relative to the wavelength. However, in [Minchew et al., 2012], the authors found that the reduction in backscatter over the Deepwater Horizon oil spill was at least partly caused by differences in the dielectric constant by evaluating the copolarization ratio. The dielectric properties of an oil spill can change with time as the slick is exposed to various weathering processes (see Section 2.3).

The presence of an oil slick may alter the scattering properties of the sea surface. Several studies have evaluated the scattering in oil slicks by investigating polarimetric features that are used as indicators for the presence of Bragg or non-Bragg scattering mechanisms. Indications of non-Bragg scattering in mineral oil spills have been found in, e.g., [Nunziata et al., 2008, Migliaccio et al., 2009a, Migliaccio et al., 2009b, Nunziata et al., 2011, Zhang et al., 2011]. However, other studies found Bragg scattering to be dominating also in mineral oils [Minchew et al., 2012]. This is further discussed in Section 5.5.1.

5.3.2 Damping Ratio

In order to detect oil spills on the ocean surface, an appreciable contrast between the backscatter from slick-free and slick-covered regions is needed. The *damping ratio* is often used to quantify this contrast [Gade et al., 1998, Franceschetti et al., 2002, Kim et al., 2010]. The damping ratio (DR) in dB can be defined as the ratio between the mean backscatter value (on linear scale) from a slick-free background sample $\langle\sigma_{0,sea}\rangle$ to the mean value of a sample extracted from the slick-covered region $\langle\sigma_{0,slick}\rangle$,

$$\mathrm{DR} = 10\log_{10}\frac{\langle\sigma_{0,sea}\rangle}{\langle\sigma_{0,slick}\rangle}. \tag{5.17}$$

Both measured and simulated oil slick damping ratios have been reported to decrease with increasing wind speed and to increase with frequency (Bragg wavenumber), oil viscosity and thickness [Gade et al., 1998, Wismann et al., 1998, Frate et al., 2011, Pinel et al., 2014, Chan-Su et al., 2013]. For moderate incidence angles, the contrast was found to increase with incidence angle in [Minchew et al., 2012, Pinel et al., 2014]. In [Wismann et al., 1998], damping ratios were found to be independent of radar look direction relative to the wind for wind speeds of 6 - 10 m/s. In several studies, no dependency of damping ratios on polarization was found [Wismann et al., 1993, Gade et al., 1998, Wismann et al., 1998], whereas other studies reported enhanced contrast in VV compared to HH [Lombardo and Oliver, 2000, Frate et al., 2011, Minchew et al., 2012, Pinel et al., 2014]. VV has the advantage of being less affected by the noise and is perceived as the preferred polarization channel for oil spill detection [Franceschetti et al., 2002, Alpers and Espedal, 2004, Girard-Ardhuin et al., 2005]. A different damping behavior is expected from sea surface slicks of various origin, as will be described in Section 5.4.1.

Damping ratios for various low backscatter ocean phenomena are investigated in Paper III.

5.3.3 Oil Spill Detection Scheme

The task of oil spill detection in SAR images has commonly been framed into three fundamental phases [Brekke and Solberg, 2005]:

- dark patch detection/segmentation,
- feature extraction,
- oil spill and look-alike classification.

The *detection* task consists of identifying the potential oil slicks present in an image by thresholding and segmentation processing. Subsequently, *feature extraction* is applied, in which a number of characteristics are derived to describe the segmented regions and their surroundings. The features are used in the *classification* step to determine the nature of the identified patches of suspected pollution and to discriminate between oil spills and other low backscatter phenomena (look-alikes).

The main focus of this thesis is on the second step, i.e., the identification of useful features to characterize low backscatter ocean regions. Segmentation of dark patches is done manually or semi-automatically when needed. Classification using k-means and standard Wishart classification is briefly discussed in Paper II. Further discussion on detection and classification methods are outside the scope of this thesis, but can be found in, e.g., [Brekke and Solberg, 2005, Topouzelis, 2008] and references therein.

Feature Extraction

In traditional single-polarization systems, a number of different features have been used to describe segmented low backscatter regions. The features can typically be divided into four classes [Brekke and Solberg, 2005]:

- *geometry and shape of the segmented region*, e.g., length, area, perimeter, elongatedness and complexity,
- *physical characteristics of the backscatter level of the segmented region and its surroundings*, e.g., slick mean value, contrast between slick and background, border gradients and region standard deviation,
- *contextual features*, e.g., wind history, location relative to ships, oilrigs and the shore,
- *texture*, i.e., information about the spatial correlation among neighboring pixels, e.g., features based on co-occurrence matrices, homogeneity measures and angular second moment.

Over the last decade, the use of *multipolarization features* for characterization of low backscatter ocean regions has been increasingly discussed in the literature. These descriptors can be related to physical properties and scattering characteristics of the observed surface. A review of multipolarization features used for oil spill detection and characterization is presented in Section 5.5.1. To the author's knowledge, these descriptors are not yet used operationally. However, as more documentation come in place and the availability of these data types increases, multipolarization features may be a useful tool for both manual/semi-manual analyses, and eventually for automatic detection schemes. Some multipolarization techniques, such as the filtering method described in [Nunziata et al., 2008], may combine several of the steps described above (see Section 5.5.1).

In the work presented in this thesis, a number of different features, mainly based on dual-copolarization data, are investigated for characterization of oil spills and other low backscatter ocean phenomena. More details on the specific descriptors investigated in Papers I - IV in Chapters 8 - 11 are provided in Section 5.5.2.

5.4 Limitations on Oil Spill Observation by SAR

Although SAR has proven to be a valuable tool for oil spill detection and monitoring, some limitations and challenges still exist. These are addressed in this section.

5.4.1 Look-alikes

Look-alikes are natural phenomena that can produce regions of reduced backscatter in SAR images, similar to those of oil spills, and hence can be misinterpreted as oil. These include a number of different phenomena:

- *Natural biogenic slicks:* Natural biogenic slicks are surface films that consist of surface-active compounds, originating from marine plants or animals. The surfactants are very efficient at damping the Bragg waves and hence produce low backscatter regions [Alpers and Espedal, 2004]. Natural slicks can be used as indicators of marine features such as fronts and eddies, as the material tend to accumulate here [Gade et al., 2013]. This look-alike phenomenon is further described below.
- *Low surface winds:* As the surface roughness is very dependent on the wind, the wind speed variability is reflected in the backscatter levels. Low wind areas caused by atmospheric circulation variation produce the most common low backscatter phenomenon. Dark patches can also be seen in cases of wind shadowing due to coastal topography or man-made obstacles [Clemente-Colón and Yan, 2000].
- *Rain effects:* Low backscatter regions can be the result of atmospheric attenuation due to volume scattering in a rain system [Clemente-Colón and Yan, 2000]. This problem is more pronounced at higher frequencies [Danklmayer et al., 2009]. The impact of rain drops on the surface can also dampen the Bragg waves and reduce the backscatter [Clemente-Colón and Yan, 2000].
- *Sea ice:* First-year ice floes are characterized by a relatively smooth surface and high salinity. Hence, the radar signal is reflected away and these areas appear dark compared to, e.g., multiyear ice. In addition, grease ice, which is newly formed ice composed of small millimeter-sized crystals, dampens the Bragg waves and causes a reduction in the SAR backscatter [Clemente-Colón and Yan, 2000].
- *Upwelling:* Upwelling is an oceanographic phenomenon in which cold and nutrient-rich water is brought up to the surface. The decrease in sea surface temperature results in lower wind stress and a decrease in Bragg waves, hence reducing the radar backscatter. In addition, the nutrient-rich waters brought to the surface can lead to formation on natural biogenic slicks [Clemente-Colón and Yan, 2000].
- *Internal waves:* Internal gravity waves affect the local sea surface velocities and hence the Bragg spectrum. Internal waves can also concentrate surfactants and appear as periodic bands of low backscatter [Clemente-Colón and Yan, 2000].

- *Natural seeps:* Natural seeps of oil from the ocean bottom can produce oil films on the sea surface. These films can be considered look-alikes if we are interested in detecting only man-made oil pollution [Brekke, 2008].

Natural Biogenic Slicks vs. Mineral Oil Spills

The natural biogenic slicks seem to be one of the most discussed look-alike phenomena in the literature. These surface films consist of surface-active organic compounds that have one hydrophobic part and one hydrophilic part. The strong tendencies both toward and against water make the molecules spontaneously arrange at the air/water interface with the hydrophobic part up in the air and the hydrophilic part down in the water. Hence, a so-called monomolecular film, which is only one molecule thick (~2.4 - 2.7 nm), is formed. In contrast, crude oil spills mainly consist of chemicals with exclusively hydrophobic character. Depending on the amount and viscosity of the oil, and on the environmental conditions, a crude oil spill will spread out over time, but the final thickness will remain orders of magnitude larger than that of monomolecular films (μm - mm, and even cm for freshly spilled oil) [Hühnerfuss, 2006]. In case of mineral oil spills, the oil will not be uniformly distributed over the slick. According to [Hollinger and Mennella, 1973], more than 90% of the oil is contained in less than 10% of the slick area. A more heterogeneous slick is hence produced compared to natural surface films.

Mineral oils have higher viscosity than natural slicks and therefore tend to remain more concentrated and result in a higher damping [Brekke and Solberg, 2005]. Wave damping by monomolecular slicks are attributed to a resonance-type damping in the short-gravity region, i.e., *Marangoni damping*. Fresh crude oils on the other hand have different physicochemical properties, and the Marangoni effect plays no role. In this case, the waves are dampened due to the high viscosity of the oil compared to the clean sea. For weathered slicks, both Marangoni and viscous damping can be in place, as surface-active compounds may be formed during the weathering, producing monomolecular slicks around the thicker oil [Hühnerfuss, 2006]. In [Gade et al., 1998], the damping ratios of mineral oil and biogenic slicks were investigated for multifrequency (L-, C- and X-band) data. A different damping behavior was observed between the two slick types. In the mineral oil spills, the damping increased with Bragg wavenumber, with a minimum in L-band. Biogenic slicks on the other hand produced a high damping in L-band. It was concluded that multifrequency SAR can be useful for discrimination between mineral oils and biogenic slicks in low to moderate wind conditions, but not in high wind speeds.

Use of Ancillary Data

The discrimination between oil spills and look-alikes is one of the main challenges for operational oil spill detection services. Ancillary information from external sources is used in combination with features extracted from the SAR data itself (see Section 5.3.3) to determine the origin of a detected region.

The primary production, and hence the amount of biogenic slicks on the surface, shows seasonal variations and depends on the quantity of light and nutrients that are available. This type of information may hence be helpful in discriminating biogenic slicks from mineral oils. Also wind speed information is useful for this purpose. The probability of detecting a biogenic slick decreases with increasing wind speed, as natural films are dissolved at moderate wind speeds, under which mineral oils may still persist [Pavlakis et al., 2001, Alpers and Espedal, 2004]. In [Espedal et al., 1998], the slick coverage on the Norwegian coast was found to be up to 40% in low wind speeds (2.5 m/s), whereas at 5 - 10 m/s, the coverage was only 5%. After a storm, more biogenic slicks are often observed, as more surface-active material is released and transported to the surface by turbulence and air bubbles [Alpers and Espedal, 2004].

Other useful ancillary information includes sea surface temperature, precipitation, ocean color and bathymetry data. Sea surface temperature can be useful to identify oceanic fronts that modulate the sea surface roughness, whereas ocean color may reveal plumes from estuaries and coastal rivers. Chlorophyll-A is an indicator of biogenic activity, and bathymetry can predict local upwelling along the continental shelf. Also contextual information such as the proximity to potential pollution sources, e.g., main maritime traffic routes, ports, pipelines and oil rigs may assist in the interpretation. The proximity to the ice edge may indicate the probability of a dark patch being grease ice [Clemente-Colón and Yan, 2000, Vespe et al., 2010].

The problem of look-alikes is an important motivation for the development of new methods utilizing multipolarization SAR data rather than single-polarization measurements. This is further discussed in Section 5.5.1, and is one of the main topics of the research presented in this thesis (Chapters 8 - 11).

5.4.2 Extraction of Slick Information

When an oil spill is detected, it is desirable to extract information about the slick in order to determine the further actions that should be taken. Information of interest includes thickness distribution, oil properties, oil type, volume of the release and the degree of weathering. Currently, no reliable methods for extracting this type of information from SAR images are in place.

The slick area can be estimated from a SAR image, but the slick thickness and hence the volume can not be extracted. As described above, the oil is not uniformly distributed over the slick, and the majority of the oil is found in a small part of the slick area. Hence, information on the thickness distribution may enable a much more effective cleanup, as the response efforts can be directed to the areas of the thickest oil.

Some studies report a potential of radar imagery for retrieving information on the relative thickness. [Wismann et al., 1998] found the damping ratio to increase with thickness for heavy fuel, and [Jones, 2001] observed a generally good correlation between the largest reduction in backscatter values and the thickest part of the oil spill, as determined visually. However, [Jones, 2001] emphasized that environmental conditions must be taken into account in the interpretation.

Some recent studies on multipolarization features have indicated a potential for observing thickness variations [Shirvany et al., 2012], and for extraction of oil volume content in emulsions [Minchew et al., 2012]. These studies are further discussed in Section 5.5.1.

5.4.3 Wind Speed Limitations

Oil spill detection in SAR images can only be performed in a limited range of wind speeds. Very low wind speeds may not provide enough contrast in surface roughness between slick-free and slick-covered surfaces for detection to be possible. On the other hand, in very strong winds, the short waves may receive enough energy to counterbalance the damping effect of the oil, and the turbulence of the upper layer may break and/or sink the oil [Pavlakis et al., 2001]. According to [Girard-Ardhuin et al., 2005], efficient oil spill detection at C-band frequency requires wind speeds in the range 2 - 3 m/s to 10 - 14 m/s.

The minimum wind speed for generating measurable Bragg waves varies with frequency. At an incidence angle of 20°, the approximate thresholds for X-, C- and L-band are ~ 2.5 m/s, ~ 2.2 m/s and ~ 2.0 m/s, respectively. The thresholds increase slightly with incidence angle and decrease slightly with ocean temperature [Donelan and Pierson Jr, 1987, Holt, 2004].

5.4.4 Sensor Limitations

The use of SAR data for oil spill detection and characterization is affected by the sensor properties and availability:

- *Polarization*: Copolarization channels are the most useful for oil spill observation, with a generally better slick-sea contrast and better signal-to-noise ratio in VV compared to HH. Cross-polarization channels produce very low backscatter with poorer slick-sea contrast and closer proximity to the noise floor. This can be a problem when using quad-polarization features, in which co- and cross-polarization channels are combined.

- *Incidence angle*: The ocean backscatter decreases as the incidence angle increases. At large angles, the signal may be limited by the noise floor. The most useful incidence angles are from 20° to 45° [Girard-Ardhuin et al., 2005].

- *Frequency*: C-band has traditionally been regarded as the most suitable frequency band for oil spill observation [Girard-Ardhuin et al., 2005]. However, sensors operating in both X- and L-band have also proven useful, and particularly X-band sensors are now being included in operational oil spill detection services. X-band is expected to provide higher damping than C-band (see Section 5.3.2), but is more sensitive to heavy rain.

- *NESZ*: The noise equivalent sigma zero (NESZ), which is the background noise (noise floor) in the SAR system, represents the limit of the detectable signal. As oil spills are low backscatter areas, the signal may be affected by the NESZ. This factor is further discussed below.

- *Spatial coverage and resolution*: In operational oil spill detection systems, vast ocean areas need to be covered, and SAR modes with large spatial coverage and relatively low resolution are applied. The low resolution may cause missed detections of small slicks, but a large coverage is prioritized. However, in the case of monitoring a known oil spill, high resolution imaging modes may be preferred. The small scene size of dual- and quad-polarization modes is one of the drawbacks of these data types, limiting their use for operational surveillance. However, progress is taking place also in this respect. Due to user demand, five new modes were installed on Radarsat-2 in 2011, including the wide fine quad-polarization, with twice the swath width of the original fine quad-polarization mode. In addition, the CP modes (see Section 4.5.4) that are available on several more recently launched and planned sensors allow for backscatter measurements of comparable finesse as fully-polarized systems, but at larger scene sizes.

- *Temporal coverage*: The temporal resolution of individual satellites is poor, which can be a limitation for operational services. However, the increasing number of available sensors is likely to improve the coverage.

NESZ

Oil spills are low backscatter regions, and the received signal may be close to the sensor noise floor. This is particularly a problem in low wind conditions, for large incidence angles and in cross-polarization channels. HH is also more severely affected by the noise than VV, especially for large incidence angles.

The potential of using SAR data for slick characterization, in addition to just detection is increasingly discussed in the literature, particularly with respect to multipolarization techniques. In the characterization case, when it is desired to extract more information from a low backscatter region, the proximity of the signal level to the noise floor is especially important. This factor hence needs to be appropriately addressed. This is emphasized in [Minchew et al., 2012], where it is found that the proximity to the noise floor can affect multipolarization parameters, which in turn may lead to wrong interpretation of these descriptors. [Minchew et al., 2012] considered all data less than 6 dB above the noise floor to be unsuitable for analysis.

Some SAR sensors are known to have a very low noise floor, like the Uninhabited Aerial Vehicle Synthetic Aperture Radar (UAVSAR) with a NESZ of -53 dB at its minimum at the mid-range of the swath, and -40 dB at near and far range [Jones et al., 2011a]. In current operational satellite SAR sensors however, we must accept much higher noise floors. The NESZ of TerraSAR-X lies between -19 dB and -26 dB, depending on the incidence angle, with an average of -21 dB [German Aerospace Center, 2010]. Radarsat-2 quad-polarization modes have NESZ values in the range -27.5 dB to -43 dB [MacDonald, Dettwiler and Associates Ltd., 2011]. For COSMO-SkyMed, a NESZ $\leq$ -19 dB is given for all products [Italian Space Agency, 2009]. On the everyday basis, this is the type of data that is available for oil spill detection services. For characterization purposes, it is therefore important to develop algorithms where the impact of the noise on value added products is minimized. A more thorough discussion of the NESZ and other data quality measures that are important for oil spill applications can be found in [Vespe and Greidanus, 2012].

The effect of sensor properties on oil spill characterization is discussed in the papers presented in Chapters 8 - 10. In particular, the proximity of the measurements to the noise floor is investigated in Papers I - III and a theoretical and experimental comparison between C- and X-band data is presented in Paper III.

5.5 Characterization of Low Backscatter Regions

This section focuses on the characterization of low backscatter regions in the marine environment. A survey of the literature on multipolarization features for this purpose is first presented. Subsequently, a summary of the features applied for characterization in this thesis is given.

5.5.1 Review of Multipolarization Features

The SIR-C/X-SAR became the first quad-polarization spaceborne SAR when it was flown onboard the space shuttle *Endeavour* in 1994. During these flights, mineral oil and substances used for simulation of biogenic slicks were released and imaged from the shuttle. Quad-polarimetric SAR data were collected in C- and L-band, whereas X-band data were acquired in single-polarization (VV) only. In addition to the experimental releases, naturally occurring slicks and real oil spills were imaged by chance. This data set has been the basis for many of the studies on oil spill observation by multipolarization SAR. Early investigations presented in [Gade et al., 1998] did not find multipolarization data very useful for oil spill characterization. However, later studies performed on the same data set, as well as on data from more recently available sensors, have demonstrated a potential for oil slick characterization using multipolarization techniques. A review of these methods is presented in the following sections.

H/A/$\bar{\alpha}$ Decomposition

The $H/A/\bar{\alpha}$ decomposition [Cloude and Pottier, 1997] based on the coherency matrix $\mathbf{T}$ in (4.13) has been used to describe the scattering taking place at a given target or surface for many different applications, including oil spill observation. The three decomposition parameters, i.e., *entropy* H, *mean scattering angle* $\bar{\alpha}$, and *anisotropy* A, are calculated from the eigenvalues and eigenvectors of $\mathbf{T}$ as

$$H = -\sum_{i=1}^{3} p_i \log_3 p_i, \tag{5.18}$$

$$\bar{\alpha} = \sum_{i=1}^{3} p_i \alpha_i \tag{5.19}$$

and

$$A = \frac{\lambda_2 - \lambda_3}{\lambda_2 + \lambda_3}, \tag{5.20}$$

where

$$p_i = \frac{\lambda_i}{\sum_{i=1}^{3} \lambda_i}, \tag{5.21}$$

and α_i is the alpha angle of the i^{th} eigenvector $\mathbf{e}_i$, extracted as

$$\alpha_i = \cos^{-1}(|\mathbf{e}_i(1)|). \tag{5.22}$$

λ_2 and λ_3 are the two smallest eigenvalues of the coherency matrix ($\lambda_1 > \lambda_2 > \lambda_3$).

H is a measure for the randomness of the scattering process, and takes values between 0 and 1. For $H = 1$, the backscattering is completely depolarized (all λ_i are equal), whereas $H \sim 0$ indicates one dominating scattering mechanism (only one non-zero λ_i). $\bar{\alpha}$ indicates the type of scattering mechanism that is dominant, and takes on values between 0° and 90°. $\bar{\alpha}$ values below 42.5° indicate surface scattering, values in the range 42.5° - 47.5° represent volume scattering and values from 47.5° - 90° suggest double-bounce scattering [Lee and Pottier, 2009]. This designation is most accurate at low values of H. The A describes the relative importance of the secondary scattering mechanisms. For the two limits $H = 0$ and $H = 1$, the A becomes zero. For intermediate values of H, a high value of A indicates that there is only one strong secondary mechanism. The A is related to small-scale roughness and is independent of the dielectric constant [Schuler and Lee, 2006].

[Cloude and Pottier, 1997] proposed an unsupervised classification method where the data are projected into the H - $\bar{\alpha}$ plane, which is segmented into nine zones representing different scattering mechanisms. The Bragg scattering described in Section 5.2.3 is identified as the area with $H < 0.5$ and $\bar{\alpha} < 42.5°$ [Lee and Pottier, 2009]. The zone boundaries have been set primarily for land areas, and a modification for ocean areas may be needed [Schuler and Lee, 2006].

Several studies apply the $H/A/\bar{\alpha}$ decomposition for oil spill observation. An early study was presented in [Fortuny-Guasch, 2003], where the anisotropy was investigated for oil spill detection in L- and C-band SIR-C/X-SAR imagery. Higher values of A were found within the slick compared to in the sea, indicating a smoother surface in the oil-covered region.

In [Schuler and Lee, 2006], the decomposition was applied to describe the scattering from biogenic slicks in Airborne Synthetic Aperture Radar (AIRSAR) L-band imagery. Increased values of H, A and $\bar{\alpha}$ were observed in the slicks compared to the clean sea. Significantly higher values for H were found at incidence angles above 45°, which [Schuler and Lee, 2006] related to resonant Marangoni damping of Bragg waves. [Schuler and Lee, 2006] found the H-$\bar{\alpha}$ classification method to work well.

In [Migliaccio et al., 2007], the $H/A/\bar{\alpha}$ decomposition was applied to C-band SIR-C/X-SAR data where mineral oil and surfactants simulating biogenic slicks were present on the sea surface. The H was found to discriminate slick-covered from slick-free areas and to distinguish some biogenic slicks from the mineral oil spill to some degree. A large overlap between the different slick types was observed in the $\bar{\alpha}$ and A values. H was identified as the main polarimetric feature for both low and high wind regimes. Increased entropy values in slick-covered regions were also observed in [Migliaccio et al., 2009a] and [Migliaccio et al., 2011a], where data from ALOS PALSAR and Radarsat-2 were analyzed, respectively.

The H-$\bar{\alpha}$-classification scheme was applied in a brief study by [Tian et al., 2010] on Radarsat-2 data containing rough sea surface, biogenic film, an atmospheric front and releases of peanut oil, gear oil and engine oil. The results were not discussed in detail, but it was concluded that the parameters were valid for discrimination between sea surface, biogenic slick and anthropogenic oil with different viscosity [Tian et al., 2010].

[Zhang et al., 2011] found increasing H and $\bar{\alpha}$ values when moving from clean sea to oil-slicks in Radarsat-2 data. This was interpreted as a change in scattering mechanism from Bragg to non-Bragg scattering [Zhang et al., 2011].

The increase in entropy over oil-covered areas were not confirmed by [Minchew et al., 2012], who analyzed UAVSAR L-band data from the Deepwater Horizon accident. For this sensor, the backscatter signal mostly lies well above the noise floor, and the scattering properties could be evaluated over a large range of incidence angles. [Minchew et al., 2012] found increased H values over the oil spill only when the signal level was approaching the noise floor. H and $\bar{\alpha}$ values consistent with a Bragg scattering mechanism were found everywhere where the signal was above the noise. At low to intermediate incidence angles, where the cross-polarization signal was more than 6 dB above the noise floor, [Minchew et al., 2012] found a higher A in the oil compared to the clean sea, indicating a smoother surface. [Minchew et al., 2012] concluded that the $H/A/\bar{\alpha}$ classification should only be applied for low noise instruments, and emphasized that the apparent randomness implied by large H values should not be used to indicate the physics of the scattering properties, but rather the randomness of the noise. They suggested the major eigenvalue λ_1 to be a useful feature. This parameter was found to be consistently lower in oil-covered regions compared to clean sea and it was less affected by the proximity of the cross-polarization channel to the noise floor.

Polarization Signature

The *polarization signature* is the normalized intensity plotted as function of the *ellipticity angle* χ and the *orientation angle* ψ, which describe the polarization of the wave. $\chi = 0°$ represents zero ellipticity, i.e., linear polarization, whereas $\chi = \pm 45°$ represents circular polarization. For vertical and horizontal polarization, $\psi = 90°$ and $\psi = 0°$ / $180°$, respectively [Gade et al., 1998]. The shape of the plots and the pedestal height provide information about the present scattering mechanism [Migliaccio et al., 2008].

One of the first studies on the use of polarimetry for oil spill observation was presented in [Gade et al., 1998], who investigated the polarization signature of slicks in SIR-C/X-SAR data. Similar signatures were observed for slicks and clean sea in both C- and L-band data. One oil slick produced an increased pedestal height compared to the clean sea, but this was interpreted as the signal reaching the noise floor. [Gade et al., 1998] concluded that polarimetric SAR was not very useful for discrimination between mineral oil and biogenic slicks, but that it might provide useful information about the scattering mechanisms.

[Migliaccio et al., 2008] compared the copolarization signatures of mineral oil spills, look-alikes and clean sea from C-band SIR-C/X-SAR data. They found a larger pedestal height in oil slicks compared to the slick-free surface, which was related to an increase in the amount of unpolarized backscatter energy. Simulated biogenic slicks were indistinguishable from the clean sea surface, and [Migliaccio et al., 2008] suggested that the pedestal height of the polarization signature could be used to distinguish between oil and biogenic slicks.

Similar results were found in [Migliaccio et al., 2009a] and [Nunziata et al., 2011] for ALOS-PALSAR and Radarsat-2 data. They related the difference in the amount of unpolarized energy to a change from Bragg scatter mechanism in clean sea to non-Bragg scattering in oil slicks. [Nunziata et al., 2011] found the Bragg scatter to be dominant in various look-alikes, including a ship wave, a natural phenomenon and a simulated biogenic slick. The normalized pedestal was found to give a higher slick-sea contrast than the entropy. In [Migliaccio and Nunziata, 2014], Radarsat-2 data over the DWH oil spill were investigated. Spatial variations in the normalized pedestal height were found and interpreted as areas of varying oil damping properties.

Copolarization Cross Product

The *copolarization cross product* is defined from the complex scattering coefficients in (4.5) as

$$\langle S_{HH} S_{VV}^* \rangle \;=\; \left\langle |S_{HH}||S_{VV}| e^{j\left(\phi_{HH} - \phi_{VV}\right)} \right\rangle . \tag{5.23}$$

This parameter is the basis for the next features, which utilize the fact that a high correlation between S_{HH} and S_{VV} is expected in clean sea areas, whereas a reduction in correlation is observed in oil slicks.

[Nunziata et al., 2008] proposed a *Mueller filtering* technique for detection and characterization of oil slicks, using elements from the Mueller matrix[1]. The filtering was based on the cross-polarization intensity $\left\langle |S_{VH}|^2 \right\rangle$ and the *magnitude of the real part of the copolarization cross product* r_{CO}, given as

$$r_{CO} = |\Re(\langle S_{HH} S_{VV}^* \rangle)| \,, \tag{5.24}$$

where $\Re$ denotes the real part. For sea surface Bragg scattering, $\left\langle |S_{VH}|^2 \right\rangle$ is small, whereas the two copolarization channels are highly correlated and large values of r_{CO} are expected. In the case of non-Bragg scattering, a reduction in the correlation is expected. [Nunziata et al., 2008] hence proposed the following method for distinguishing oil-covered areas, where they expected a non-Bragg scattering mechanism to be present, from slick-free sea and biogenic slicks, in which Bragg scattering was assumed:

- $r_{CO} > \left\langle |S_{VH}|^2 \right\rangle$ for slick-free surfaces and biogenic slicks

[1] The Mueller matrix relates the transmitted and received Stokes vectors and is described in, e.g., [Lee and Pottier, 2009].

- $r_{CO} < \langle |S_{VH}|^2 \rangle$ for mineral oil spills

The filtering technique requires no external threshold. The method was found to work well on SIR-C/X-SAR C-band data and ALOS PALSAR data in [Nunziata et al., 2008] and [Migliaccio et al., 2009a], respectively.

In [Zhang et al., 2011], an unsupervised oil spill mapping method based on the same theoretical rationale as in [Nunziata et al., 2008] was presented. The *conformity coefficient*, CC, was defined for quad-polarization SAR as

$$\mathrm{CC} \cong \frac{2[\Re(S_{HH}S_{VV}^{*}) - |S_{VH}|^2]}{(|S_{HH}|^2 + 2|S_{VH}|^2 + |S_{VV}|^2)}. \tag{5.25}$$

Clean sea and oil slicks were expected to produce positive and negative values of CC, respectively, and the logical true-false output could be used for segmentation and classification. The method was tested on Radarsat-2 data in moderate wind conditions, and was found to clearly discriminate oil-covered areas from the sea surface. However, [Zhang et al., 2011] remarked that look-alikes may be a problem for this method, and that in high sea states, breaking waves will depolarize the backscatter and reduce the usefulness of the CC.

The *standard deviation of the copolarized phase difference* (i.e., the standard deviation of the phase of the cross product defined in (5.23)) is given as

$$\sigma_{\phi CO} = \sqrt{\langle(\phi_{HH} - \phi_{VV})^2\rangle - (\langle\phi_{HH} - \phi_{VV}\rangle)^2}. \tag{5.26}$$

The individual phase angles ϕ_{HH} and ϕ_{VV} are uniformly distributed over $[-\pi, \pi]$ and contain no information about the geometric and dielectric properties of a target. The *phase difference* $\phi_{CO} = \phi_{HH} - \phi_{VV}$ on the other hand, may contain useful information. The distribution of ϕ_{CO} is completely specified by two parameters, i.e., the degree of correlation between S_{HH} and S_{VV}, which measures the width of the pdf, and the value of ϕ_{CO} where the distribution is at its maximum [Ulaby et al., 1992]. The standard deviation of the phase difference, $\sigma_{\phi CO}$, may be used as a measure for the degree of correlation between S_{HH} and S_{VV}.

[Migliaccio et al., 2009b] suggested to use $\sigma_{\phi CO}$ as a measure of the departure from Bragg scattering, to distinguish clean sea and weak-damping look-alikes from mineral oil spills. They proposed that a Bragg scatter mechanism in the former case would produce a narrow ϕ_{CO} pdf and small values of $\sigma_{\phi CO}$, whereas an increase in $\sigma_{\phi CO}$ would take place in oil spills characterized by a non-Bragg scattering mechanism.

The $\sigma_{\phi CO}$ was evaluated for C- and L-band SIR-C/X-SAR data in [Migliaccio et al., 2009b], and was found to emphasize oil spills with respect to the sea surface background, whereas biogenic slicks were de-emphasized and indistinguishable from the sea. In one case, the filtering was not effective, and the authors attributed this to the small size of the slick and the high wind conditions. In [Migliaccio et al., 2011b] and [Velotto et al., 2011], $\sigma_{\phi CO}$ was found useful for oil spill detection in ALOS PALSAR and TerraSAR-X data, respectively.

In [Velotto et al., 2011], the $\sigma_{\phi CO}$ was compared to the *magnitude of the copolarization correlation coefficient* ρ_{CO}, given as

$$\rho_{CO} = \left| \frac{\langle S_{HH} S_{VV}^* \rangle}{\sqrt{\langle |S_{HH}|^2 \rangle \langle |S_{VV}|^2 \rangle}} \right|. \tag{5.27}$$

Both ρ_{CO} and $\sigma_{\phi CO}$ emphasized the presence of oil with respect to the background sea, while de-emphasizing the presence of look-alikes. However, the $\sigma_{\phi CO}$ was found to be preferred for observing illicit oil spills, as it gave better results for small window sizes.

Copolarization Power Ratio

The *copolarization power ratio* γ_{CO} is defined as

$$\gamma_{CO} = \frac{\langle |S_{HH}|^2 \rangle}{\langle |S_{VV}|^2 \rangle}. \tag{5.28}$$

As described in Section 5.2.3, in the Bragg and tilted Bragg models, the copolarization power ratio is independent of roughness, and is only a function of the dielectric constant, the surface slope and the incidence angle.

[Minchew et al., 2012] evaluated γ_{CO} for UAVSAR L-band data over the DWH oil spill. A difference in γ_{CO} was observed between clean sea and oil-covered areas. It was hence concluded that the reduction in backscatter in the oil slick was at least partly caused by a reduction in the dielectric constant. Based on the measured γ_{CO} over clean water, [Minchew et al., 2012] estimated the surface slope angles, which were subsequently used to estimate the dielectric constant of the slick and the volumetric oil concentration. To the author's knowledge, this is the first paper utilizing a multipolarization feature to estimate quantitative slick information.

Other Features

A number of other multipolarization features have also been applied for oil spill observation in the literature. The *average intensity* $\Lambda = \lambda_1 p_1 + \lambda_2 p_2 + \lambda_3 p_3$ based on the decomposition of $\mathbf{T}$ was investigated in [Jones et al., 2011b] and the *Shannon entropy* was found useful for oil spill detection in [Jones et al., 2011a]. The *circular polarization coherence*, related to surface roughness, was investigated in [Fortuny-Guasch, 2003]. [Nunziata et al., 2013] examined the *degree of polarization* (DoP) as a measure of the departure from Bragg scattering. In [Nunziata et al., 2012], a subset of the features described above, i.e., the pedestal height, $\sigma_{\phi CO}$ and the DoP were reformulated in terms of Mueller matrix elements, to unify the features and allow for a better comparison.

Feature Combinations

Using combinations of several multipolarization features rather than individual descriptors has been motivated by the fact that look-alikes and sea clutter may have similar values as oil spills in some features but not in all. A combined feature may hence be better for discrimination than the individual features. [Wenguang et al., 2010] proposed the combined feature F_W, given as

$$F_W = \frac{(1 - H) + (1 - \bar{\alpha}) + A_{12} + \rho_{CO}}{4}, \tag{5.29}$$

where

$$A_{12} = \frac{\lambda_1 - \lambda_2}{\lambda_1 + \lambda_2}. \tag{5.30}$$

F_W takes values in the range [0, 1]. [Wenguang et al., 2010] compared segmentations of C-band SIR-C/X-SAR data based on the F_W and the *Span*,

$$Span = |S_{HH}|^2 + |S_{VV}|^2 + 2|S_{VH}|^2 = \lambda_1 + \lambda_2 + \lambda_3. \tag{5.31}$$

Similar results were obtained with F_W and *Span*, but [Wenguang et al., 2010] argued that a lower number of iterations (shorter processing time) was an advantage of the combined feature.

A similar feature combination was applied in [Liu et al., 2011], i.e.,

$$F_L = \frac{H + \bar{\alpha} + A + \rho_{CO}}{4}, \tag{5.32}$$

where each feature was normalized to have a maximum value of one. Enhanced visual slick-sea contrast was found in F_L compared to in the individual features in UAVSAR L-band data over the DWH oil spill. Both *Span* and F_L were found to be effective for oil spill segmentation, but a more strict segmentation result was obtained in the case of F_L [Liu et al., 2011].

Use of Compact Polarimetry

As described in Section 4.5.4, compact polarimetry can be used to realize many of the benefits of quad-polarization or coherent dual-polarization data, with the advantage of a larger swath width. Several papers investigate the use of CP data for oil spill observation by simulating these data types from quad-polarization measurements.

In [Shirvany et al., 2012], the degree of polarization from various combinations of dual-polarization data, including CP modes, were compared with respect to oil spill detection in Radarsat-2 and UAVSAR data. The best discrimination between oil and water was obtained with the HH/HV combination at small incidence angles, and with HH/VV at large incidence angles. The hybrid and compact modes produced results that were similar to those obtained with HH/VV. In [Shirvany et al., 2012], internal slick variations in the degree of polarization were interpreted as areas of varying thickness.

Oil spill detection by hybrid-polarimetric SAR generated from Radarsat-2 data was also explored by [Salberg et al., 2014]. A number of CP features were investigated and it was concluded that similar detection results could be obtained with CP data as with quad-polarization measurements [Salberg et al., 2014].

As the first studies on the application of CP data for oil spill observation have given promising results, and as several recently launched and planned SAR sensors offer CP acquisitions, these data types may be increasingly used for oil spill observation in the future.

5.5.2 Features Investigated in This Thesis

Characterization of low backscatter regions in the marine environment is the main focus of this thesis. A number of different features are investigated for this purpose in the papers presented in Chapters 8 - 11. Table 5.1 gives an overview of these features. The papers in which each feature or feature set is applied are indicated, and parameters that are not defined in the preceding sections of this thesis are defined in Table 5.1.

Several of the investigated features were selected based on the literature review presented in the previous section. As the noise analysis in Paper II reveals that the cross-polarization channels are severely contaminated by noise, the investigated features are based only on the copolarization channels. Hence, an alternative version of the $H/A/\bar{\alpha}$ decomposition is applied, as can be seen in Table 5.1. The superscript $'$ is used to distinguish the dual-copolarization versions from the conventional definitions. In the dual-copolarization case, we have that $p_2 = 1 - p_1$. For p_1 close to 1, H' tends to 0, and a dominant scattering mechanism can be identified. If $p_1 = p_2$, then $H' = 1$ and the scattering is random. As only two eigenvalues are extracted from $\mathbf{T}$, the anisotropy A' measures the difference in size between these two. This differs from the conventional definition using the two smallest eigenvalues. It should be noted that the dual-copolarization versions of the entropy and anisotropy represent the same information, and A' can be written as $A' = 2p_1 - 1$. Only two α_i angles are extracted in this case, with $\alpha_1' + \alpha_2' = 90°$. It is more interesting to look at the dominating scattering mechanism than the mean of the two, hence α_1' is investigated in Paper I.

In addition to the features described above, the *geometric intensity* μ and the *normalized copolarization difference* D_{CO} are investigated. The μ is a measure of the combined intensity in the copolarization channels, and is hence expected to provide a good contrast between slick-free and slick-covered regions. μ is similar to the *Span*, but is computed as the geometric mean of the eigenvalues rather than the sum. The D_{CO} is a normalized version of the PD.

As mentioned in Section 5.3.3, single-polarization *spatial texture* features, e.g., based on the co-occurrence matrix, have previously been used for oil spill classification. However, these features contain a different type of information than the *radar texture* introduced in Section 4.6. In the work presented in this thesis, we explore the radar texture in various low backscatter regions in terms of the sample log-cumulants defined in Section 4.6.3. Log-cumulants from SLI measurements (κ_2 and κ_3) are investigated in Paper III for Radarsat-2 and TerraSAR-X data. Further analysis is presented in Paper IV where log-cumulants (κ_1 and κ_2) are extracted from the MLC covariance matrix based on Radarsat-2 data. To the author's knowledge, log-cumulants have not been applied for oil spill observation in previous studies. κ_1 is related to the backscatter intensity, and lower values are expected in oil slicks

Table 5.1: Overview of the features investigated in Papers I - IV presented in Chapters 8 - 11.

Feature(s)	**Paper(s)**	**Comments**
Entropy (H')	I, II	Dual-copolarization version: $H' = -\sum_{i=1}^{2} p_i \log_2 p_i$
Anisotropy (A')	II	Dual-copolarization version: $A' = \frac{\lambda_1 - \lambda_2}{\lambda_1 + \lambda_2}$
Alpha angle of the largest eigenvalue (α'_1)	II	Dual-copolarization version: $\alpha'_1 = \cos^{-1}(\lvert \mathbf{e_1}(1) \rvert)$
Real the part of the copolarization cross product (r_{CO})	I, II, III	
Standard deviation of the copolarized phase difference ($\sigma_{\phi CO}$)	I, II	
Magnitude of the copolarization correlation coefficient (ρ_{CO})	II	
Copolarization power ratio (γ_{CO})	I, II	
Geometric intensity (μ)	II, III	$\mu = (\lvert \mathbf{T} \rvert)^{1/2}$
Normalized copolarization difference (D_{CO})	I	$D_{CO} = \frac{\langle \lvert S_{VV} \rvert^2 \rangle - \langle \lvert S_{HH} \rvert^2 \rangle}{\langle \lvert S_{VV} \rvert^2 \rangle + \langle \lvert S_{HH} \rvert^2 \rangle}$
Scattering model parameters (defined in Section 5.2.3)	III	PD, PR, NP, $\sigma_{0B}^{VV}/\sigma_0^{VV}$, $\sigma_{0nB}/\sigma_0^{VV}$
Log-cumulants (SLI) (defined in Section 4.6.3)	III	Second and third order (κ_2 and κ_3)
Log-cumulants (MLC) (defined in Section 4.6.3)	IV	First and second order (κ_1 and κ_2)

compared to slick-free areas. As described in Section 5.4.1, mineral oils typically form slicks with inhomogeneous distribution of oil, whereas natural slicks form monomolecular films. Hence, a higher textural variation may be found in mineral oils compared to clean sea and biogenic slicks.

A summary of the research part of this thesis is given in Chapter 7 and the full papers are presented in Chapters 8 - 11.

Chapter 6

Data Collection

One challenge for the scientific community working with remote sensing of oil spills is the lack of data. It is not known where and when an oil spill will take place, and it is difficult to obtain permission to do deliberate releases for scientific purposes. In operational oil spill detection services, mostly single-polarization data are collected, and ground truth information is often not available. For this thesis, data were acquired during large scale oil-on-water exercises in the North Sea conducted by the Norwegian Clean Seas Association for Operating Companies (NOFO). The main objectives of these campaigns are to test procedures and equipment for oil spill response. The unique opportunity also for collection of remote sensing data for scientific purposes is now recognized. During the exercises in June 2011, June 2012 and June 2013, the data set used for the work in this thesis was acquired. This chapter describes the exercises and the data collection.

6.1 Oil-On-Water Exercises

NOFO is an organization for operators on the Norwegian Continental Shelf, that covers the members need for an effective oil spill preparedness. This includes developing and implementing new oil spill response technologies. As part of this work, NOFO conducts an annual oil-on-water (OOW) exercise, in which oil is released onto the open sea in order to test procedures and equipment for oil spill response under realistic conditions. The exercises take place at the Frigg field in the North Sea, within 10 nautical miles of the position 59° 59' N, 02° 27' E, which is indicated in Fig. 6.1. The time and location of the exercises are carefully selected as the biological activities (presence of birds and marine life) are at a minimum.

The OOW exercises are large events, involving a number of vessels, aircrafts and representatives from, e.g., the oil industry, research and development companies, pollution authorities, the coast guard, the coastal administration and research institutions. Norway is one of few countries that allow discharges of oil onto the sea surface for this type of exercises. The OOW campaigns hence gain international attention, and, e.g., oil pollution surveillance aircrafts from different countries have participated. During the exercises,

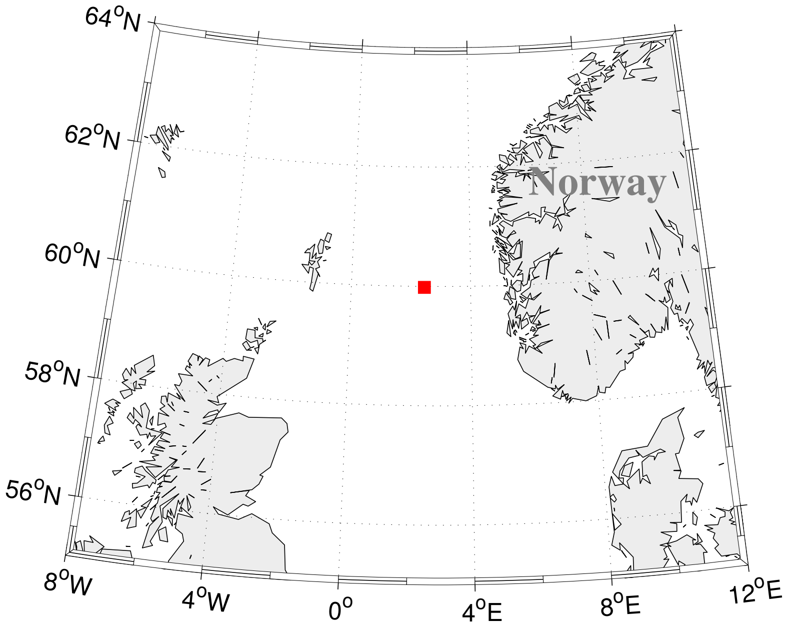

Figure 6.1: The oil-on-water exercises take place at the Frigg field in the North Sea, indicated by the red square.

different tests are carried out. Equipment for oil spill cleaning up, e.g., dispersion systems, booms and skimmers, are the major exercise elements. Other components include leadership, communication, efficient use of equipment and downlink of imagery from aircraft to ship. Remote sensing is done from ships, aircrafts and aerostats tethered to a ship, in addition to the collection of satellite data. Some photos from OOW-2011 taken from ships and aircrafts are shown in Fig. 6.2 and Fig. 6.3, respectively.

6.1.1 OOW-2011

The exercise in 2011 took place from 6 - 9 June, during which three different substances were released. A volume of 20 m^3 emulsion of Oseberg blend crude oil mixed with 5% IFO380[1], with an initial water content of 69%, was released and subjected to mechanical recovery (shown in Fig. 6.2(a) - 6.2(d) and Fig. 6.3(a) - 6.3(b)). About 1 m^3 of emulsion was not recovered, and the remains were imaged by SAR the next day. From boats close to the slick, the thickness of free-floating emulsion was estimated to be 0.1 - 1.5 mm. A volume of 30 m^3 of evaporated Balder crude oil was released and subjected to chemical dispersion (shown in Fig. 6.2(e) - 6.2(f) and Fig. 6.3(c) - 6.3(d)).

In addition to the releases of mineral oil, 0.4 m^3 of Radiagreen ebo plant oil were released and left on the surface untouched. The plant oil is a 2-ethylhexyl oleate, a monoalkyl ester

[1]Intermediate Fuel Oil with viscosity $\leq$ 380 cSt (<3.5% sulphur).

(a) Oil is released into the boom system.

(b) Oil is drifting into the boom.

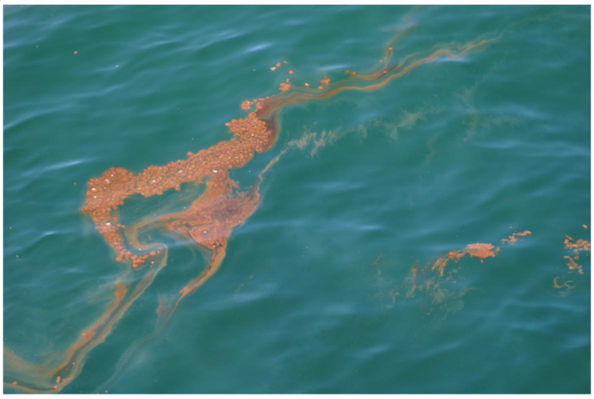

(c) Emulsion on the surface.

(d) Collected oil is being pumped up.

(e) Dispersion of free floating oil.

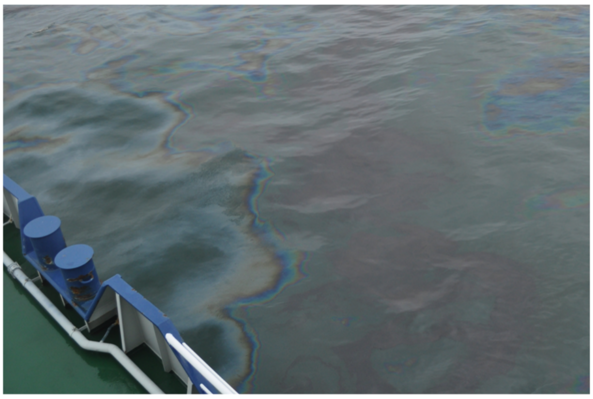

(f) Various thickness zones in the oil spill.

Figure 6.2: Photos from the OOW-2011 exercise. Photos: Stine Skrunes.

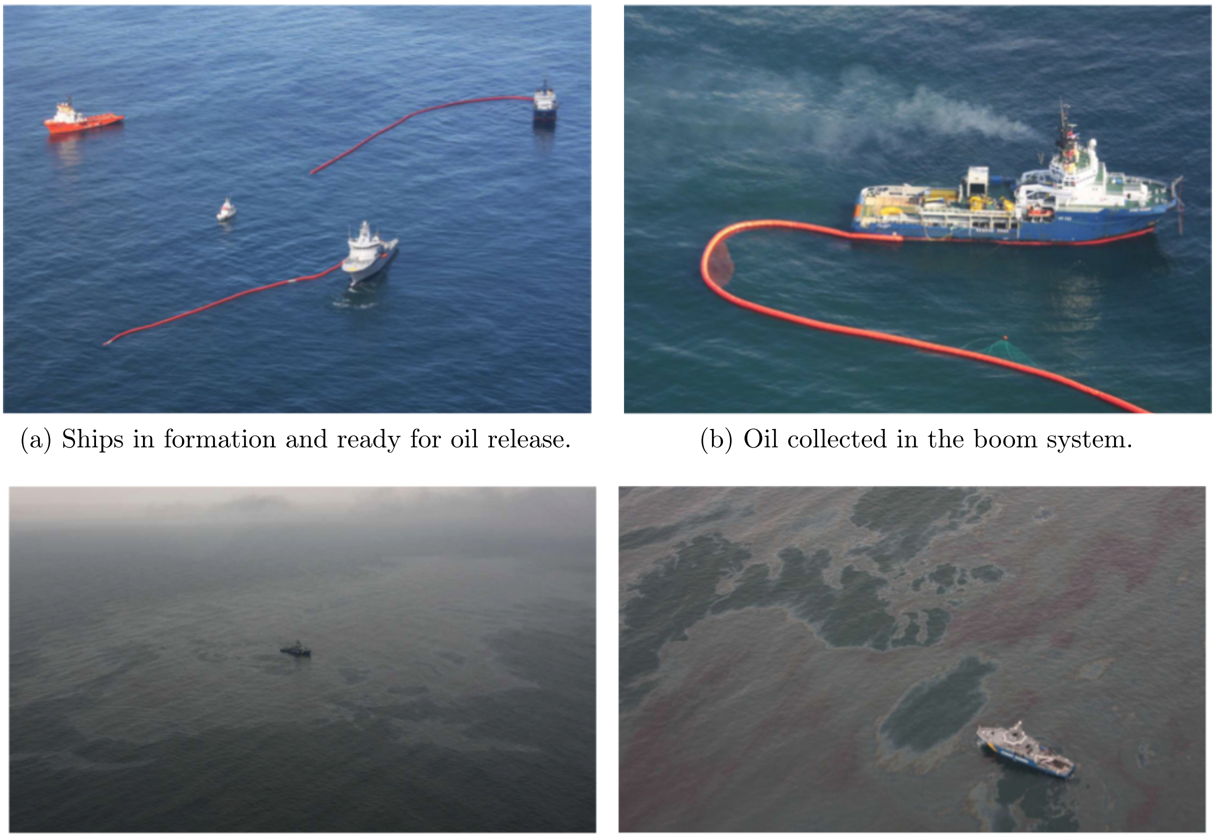

(a) Ships in formation and ready for oil release. (b) Oil collected in the boom system.

(c) Overview of crude oil slick. (d) Crude oil slick.

Figure 6.3: Aerial photos from the OOW-2011 exercise. Photos are courtesy of Kystverket/NOFO/Sundt Air.

of an oleic acid. The plant oil will have a similar ambiphilic structure as the surface active compounds in natural slicks described in Section 5.4.1. In this work, the plant oil slick is treated as a substitute for natural monomolecular biogenic slicks. More information on the properties of the released substances is given in the papers in Chapter 9 and Chapter 10.

6.1.2 OOW-2012

OOW-2012 was conducted from 11 - 15 June 2012. Three releases of Oseberg blend emulsion with an initial water content of 58% were done this year. The first two releases amounted to 31 m^3 and 10 m^3 and were both subjected to mechanical recovery. Chemical dispersion was applied to the third release of 25 m^3. The properties of the emulsion are further described in Paper III in Chapter 10.

As in OOW-2011, 0.4 m^3 of plant oil were released for simulation of natural slicks. In addition, a release of 20 L of oleyl alcohol (OLA) was carried out, as this substance has previously been used to simulate biogenic slicks [Gade et al., 1998]. Unfortunately, the OLA was not detected by SAR, probably due to the poor quality of the subsequent acquisitions.

6.1.3 OOW-2013

OOW-2013 took place from 10 - 14 June 2013. Oseberg blend emulsion (added max 5% IFO380 and max 0.13% emulsifier), with an initial water content of 62% - 64%, was released. Three discharges of 45 m^3, 17 m^3 and 24 m^3 were conducted to test equipment for mechanical recovery. A fourth emulsion release of 6 m^3 was done during night in order to test IR remote sensing from aerostat in darkness. In addition, three releases of plant oil, each 0.4 m^3, were done in en effort to acquire several images with both plant oil and mineral oil spills.

6.2 Remote Sensing Data Collection

During OOW exercises, remote sensing data were acquired with different sensors and carrier platforms, as described in the following sections.

6.2.1 SAR Data Set

The work presented in this thesis is based on satellite SAR data acquired by Radarsat-2, TerraSAR-X and COSMO-SkyMed. Sensor properties are given in Table 6.1, for the specific modes used in this thesis. An overview of the multipolarization SAR data collected during OOW exercises is presented in Table 6.2. It should be noted that COSMO-SkyMed collects dual-polarization data in the PingPong mode, which is based on alternating polarizations between bursts. The phase link between the polarization channels is not preserved and the relative phase can not be used in the data analysis [Nunziata and Migliaccio, 2013]. TerraSAR-X and Radarsat-2 are coherent systems where also the relative phase can be used in the interpretation. Examples of SAR images containing low backscatter regions of various origins are presented in Fig. 6.4. The bright point targets close to the oil slicks are ships participating in the exercises. The Radarsat-2 scene shown in Fig. 6.4(a) is acquired about one hour after the aerial photos of the crude oil spill presented in Fig. 6.3(c) and Fig. 6.3(d).

6.2.2 Other Remote Sensing Data

Initially, a comparison between SAR and multispectral data was intended to be carried out during this project. However, obtaining near coincident data from SAR and multispectral sensors has proven difficult. In addition, acquisition of multispectral data can be challenging due to cloud cover. One multispectral RapidEye scene with visible oil slicks was acquired during OOW-2012. A subset of the scene is presented in Fig. 6.5. The image was collected about 6 hours after the Radarsat-2 acquisition shown in Fig. 5.3, and the same slick shapes can be recognized in both scenes. A preliminary investigation of the two acquisitions is

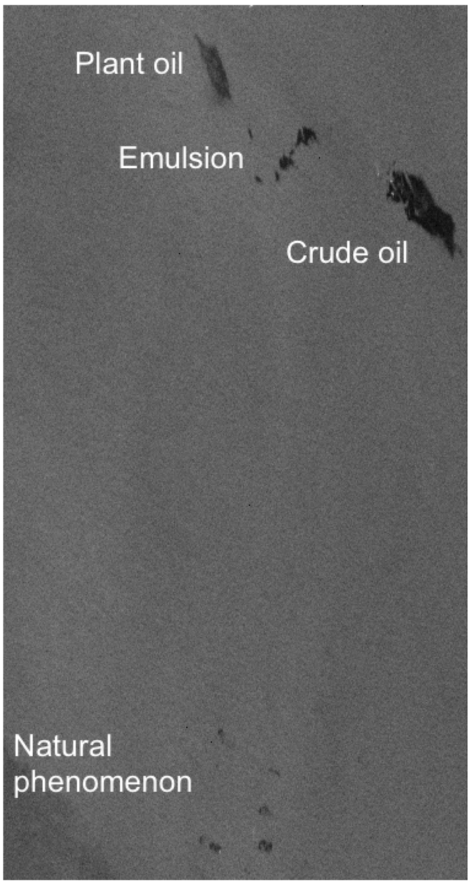

(a) Radarsat-2 scene from 8 June 2011, 17.27 UTC. RADARSAT-2 Data and Products ©MDA LTD. (2011) - All Rights Reserved.

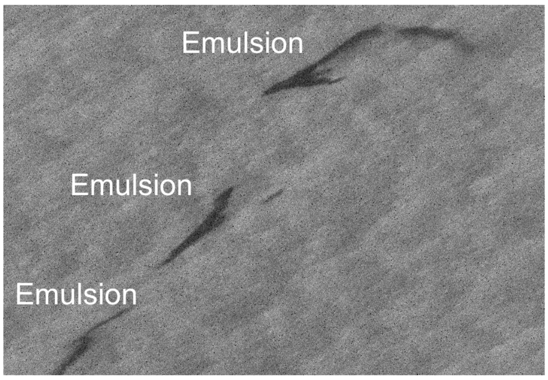

(b) TerraSAR-X scene from 15 June 2012, 17.28 UTC. TerraSAR-X data ©2012 DLR.

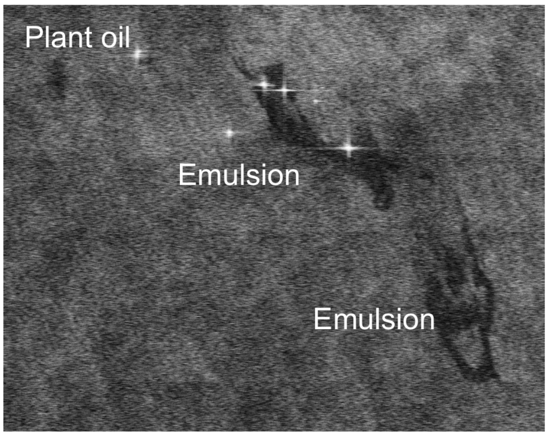

(c) COSMO-SkyMed scene from 14 June 2012, 17.55 UTC. Copyright ©ASI (2012).

Figure 6.4: Examples of SAR images (VV intensity).

Table 6.1: Properties of the SAR sensors and modes used in this thesis [Italian Space Agency, 2009, German Aerospace Center, 2010, MacDonald, Dettwiler and Associates Ltd., 2011]. 'rg.' and 'az.' denote range and azimuth directions, respectively.

	Radarsat-2	**COSMO-SkyMed**	**TerraSAR-X**
Frequency	C-band (5.405 GHz)	X-band	X-band (9.65 GHz)
Mode, format[a]	Fine Quad-pol, SLC	PingPong, SCS	Stripmap, SSC
Polarization	Quad	Dual (HH/VV, HH/HV, VV/VH)	Dual (HH/VV, HH/HV, VV/VH)
Incidence angle	18° - 49°	∼20° - ∼60°	20° - 40° (recommended) (15° - 60° accessible)
Scene size (rg. × az.)	25 km × 25 km	30 km × 30 km	15 km × 50 km
Resolution[b] **(rg. × az.)**	5.2 m × 7.6 m	15 m × 15 m	1.2 m × 6.6 m
Pixel spacing (rg. × az.)	4.7 m × 5.1 m	3 - 8 m × 2 - 2.5 m	0.9 m × 2.5 m
NESZ	-36.5 ± 3 dB	≤ -19 dB[c]	-19 dB

[a] SLC: Single Look Complex, SCS: Single-look Complex Slant, SSC: Single-look, Slant-range, Complex.
[b] Range resolution is given in ground range for COSMO-SkyMed, and in slant range for Radarsat-2 and TerraSAR-X.
[c] Common figure for COSMO-SkyMed products, not mode-specific.

Table 6.2: Overview of the multipolarization SAR data collected during OOW-2011, OOW-2012 and OOW-2013. 'ROIs present' indicates the regions of interest present in the scenes. 'P', 'E', 'C' and 'N' denotes plant oil, emulsion, crude oil and natural phenomenon, respectively.

Sensor	**Date (time)**	**Incidence angle**	**Polarization**	**ROIs present**
Radarsat-2	08.06.11 (05.59)	46.1° - 47.3°	Quad	P, E
TerraSAR-X	08.06.11 (06.23)	27.3° - 29.0°	Dual (HH/VV)	E
TerraSAR-X	08.06.11 (17.11)	19.9° - 21.7°	Dual (HH/VV)	P, E, C, N
Radarsat-2	08.06.11 (17.27)	34.5° - 36.1°	Quad	P, E, C, N
TerraSAR-X	14.06.12 (17.45)	55.4° - 56.0°	Dual (HH/VV)	None visible
COSMO-SkyMed	14.06.12 (17.55)	41.7° - 43.2°	Dual (HH/VV)	P, E
COSMO-SkyMed	15.06.12 (05.29)	39.6° - 41.7°	Dual (HH/VV)	P, E
Radarsat-2	15.06.12 (06.20)	30.3° - 32.0°	Quad	P, E
TerraSAR-X	15.06.12 (17.28)	40.9° - 42.1°	Dual (HH/VV)	E
Radarsat-2	15.06.12 (17.48)	48.3° - 49.5°	Quad	E
COSMO-SkyMed	15.06.12 (19.01)	23.5° - 26.1°	Dual (HH/VV)	E
Radarsat-2	11.06.13 (17.19)	28.1° - 29.8°	Quad	P, E
TerraSAR-X	13.06.13 (17.29)	41.7° - 42.9°	Dual (HH/VV)	P, E

presented in [Skrunes et al., 2012b], where some correlation between apparent variations in multispectral data and SAR multipolarization features is observed. However, limited ground truth data is a challenge for the interpretation of these variations.

SLAR and aerial photo were collected by aircrafts participating in the exercises (see Fig. 6.3), and optical and near IR photo and video were obtained from aerostat. Obtaining coincident measurements from SAR and other instruments proved to be difficult, both due to the weather limitations of other sensors, and due to competing interests during the exercises.

6.3 Challenges and Limitations

The OOW campaigns offer unique opportunities to collect remote sensing data of marine oil spills and corresponding ground truth information, e.g., oil volume, properties and weather conditions. However, some challenges and limitations have been recognized with respect to the exercises and data collection.

A number of different tests were conducted during the exercises, and the main focus was on the oil spill cleaning up operations, not the remote sensing. Hence, in some cases, different interests could make it difficult to obtain all the desired data and information.

The released oil was not always free floating on the surface, and a certain, in some

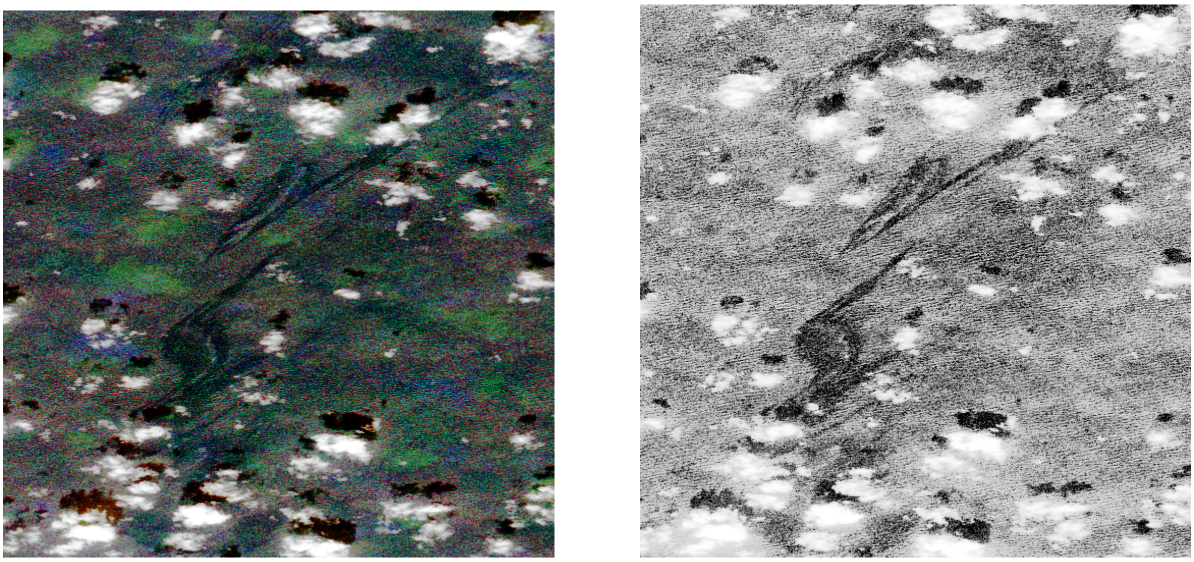

(a) Composite of the red, green and blue channels.

(b) Near infrared channel.

Figure 6.5: RapidEye image from 15 June 2012, 12.08 UTC. Emulsion slicks are seen in the middle of the image. Delivered by RapidEye, ©RapidEye (2012) - All Rights Reserved.

cases unknown, amount of oil was recovered or dispersed before the satellite overpasses. Hence, the amount of oil left on the surface was not always known, and an unknown degree of weathering had taken place before the SAR acquisitions. Sampling and measurements of the oil slick properties were done on a few occasions, but not close in time to satellite overpasses.

One important value of the OOW exercises was the releases of plant oil, which was used to simulate natural biogenic slicks. A number of other substances have previously been used for this purpose, including OLA, oleic acid methyl ester and triolein [Gade et al., 1998]. The plant oil is expected to form a monomolecular film, similar to films produced naturally by marine organisms, and has a relatively low viscosity. However, a quantitative comparison of the slick properties with those of other simulated or natural slicks has not been conducted. A release of OLA was done during OOW-2012, but it was not detected by SAR, probably due to the poor SAR quality of the subsequent acquisitions. As the plant oil slicks were produced artificially, the geometric properties may not be representative of naturally occurring slicks. Therefore, geometric characteristics are not investigated in this thesis.

The wind speed is important for determining the radar backscatter intensity and the detectability of oil slicks. In this work, wind measurements are done at ships participating in the exercises and from the closest platform Heimdal, which is situated south of the exercise area. Some uncertainty applies to the platform measurements due to spatial and temporal differences between SAR acquisitions and wind observations. The measurements from ships are acquired in the area of interest, but are only recorded every one or four hours. In some cases, these measurements are on the Beaufort scale, which gives a range of wind speeds rather than one value. The limitations of the available wind information are discussed in Paper III and Paper IV. In these papers, wind speed extracted from the SAR data is also included. The wind retrieval is done by scientists at the Northern Research Institute (Norut). Some deviation between wind measurements and the SAR wind are found. Large incidence angles and low wind speeds can cause the SAR wind to be more uncertain. In addition, some uncertainty applies to the wind directions that are used as input, as these are the measurements from the ships and the platform. Recording wind speed information from ships at the exact time of satellite overpasses will be emphasized in the future experiments.

Chapter 7

Overview of Publications

This chapter contains a summary of the four publications presented in Chapters 8 - 11 and an overview of other, related publications.

7.1 Paper Summaries

Paper I

S. Skrunes, C. Brekke, T. Eltoft and V. Miegebielle, "**An Experimental Study of X-Band Synthetic Aperture Radar (SAR) Imagery for Marine Oil Slick Monitoring**", *Proc. 36th Arctic and Marine Oilspill Program (AMOP) Technical Seminar on Environmental Contamination and Response*, Halifax, Canada, 4 - 6 Jun. 2013, pp. 498-514.

Over the last decades, mostly C-band SAR sensors have been used for operational satellite based oil spill detection. Several of the more recently launched satellites, e.g., TerraSAR-X and COSMO-SkyMed, as well as planned missions such as TerraSAR-X Next Generation and PAZ, operate in the X-band frequency range. As X-band sensors are now being incorporated into the oil spill detection services, more information on the use of X-band compared to C-band is requested.

The aim of this paper is to investigate the usefulness of multipolarization X-band SAR data for oil spill observation. Noise properties and visual slick-sea contrasts in multipolarization features are investigated and compared with respect to incidence angle. In addition, a preliminary evaluation of temporal slick changes, feature value consistency between scenes and a comparison in terms of slick type and age are presented. Dual-copolarization SAR data collected by TerraSAR-X and COSMO-SkyMed during OOW-2011 and OOW-2012 are analyzed.

It is found that slicks of different types and ages are detected by both sensors in low wind conditions (1.6 - 5 m/s), except at very large incidence angles ($> 55°$). The noise analysis shows that for large incidence angles, the signal levels lie partly below the noise floor. On the other hand, the multipolarization features are less useful at the lowest incidence angles

($\sim 20° - 21°$ for TerraSAR-X and $\sim 24° - 26°$ for COSMO- SkyMed). Hence, intermediate incidence angles seem preferable when using multipolarization features.

In the COSMO-SkyMed PingPong mode, the phase link between the polarization channels is not preserved, and only intensity based multipolarization features are extracted from these acquisitions. This is an important difference between COSMO-SkyMed and TerraSAR-X, as the latter provides coherent measurements, where the relative phase can also be used. For the data analyzed here, we find that the intensity based features produce a poorer slick-sea contrast compared to the features in which phase information is included. Hence, TerraSAR-X data are found more useful for multipolarization analysis than COSMO-SkyMed data. For TerraSAR-X data at incidence angles $\sim 27° - 29°$ and $\sim 41° - 42°$, the features including phase information clearly distinguish slicks from the surrounding sea, and consistency in the feature values between the scenes is seen to some extent. No clear variation with slick age is found.

The applicability of TerraSAR-X data for oil spill observation is further discussed in Paper III, where a comparison between coincident Radarsat-2 and TerraSAR-X data is presented.

Paper II

S. Skrunes, C. Brekke and T. Eltoft, "**Characterization of Marine Surface Slicks by Radarsat-2 Multipolarization Features**", *IEEE Transactions on Geoscience and Remote Sensing*, vol. 52, no. 9, pp. 5302-5319, Sep. 2014.

Oil spill detection by SAR has conventionally been performed on single-polarization (VV or HH) data. The availability of sensors with dual- and quad-polarization abilities has increased over the last decade and many studies on the application of these measurements for oil spill observation have been carried out. Promising results for the detection and characterization of oil slicks, including the task of oil versus look-alike discrimination, have been found. Most of the previous studies promote individual features without a comparison to other recommended/available features. In addition, a majority of the previous investigations were performed on data from discontinued missions, such as the SIR-C/X-SAR, or from systems with restricted availability, such as the UAVSAR.

In this paper, a systematic comparison of eight well-known multipolarization features is carried out, with the aim of identifying the most useful descriptors for mineral oil spill versus biogenic slick discrimination. Two Radarsat-2 fine quad-polarization scenes acquired during OOW-2011 are analyzed. These are morning and evening scenes from the same day, and each contains both mineral oil spills and a simulated biogenic slick.

A noise analysis of the data is first performed, from which we conclude that the signal levels in the cross-polarization channels are not strong enough for the desired analysis of oil slick characteristics. Therefore, the cross-polarization channels are discarded, and multipolarization features derived from only the copolarized scattering coefficients are explored. The subsequent feature analysis and selection are performed on one of the two scenes. We find that the two most powerful multipolarization features are the *geometric* *intensity*, which measures the combined intensity based on the determinant of the coherency matrix, and the *real part of the copolarization cross product*, which is related to the scattering behavior of the target. The selected feature pair is used as basis for a k-means classification of both scenes. The results show that the two features can distinguish between a simulated biogenic slick and mineral oil types such as Balder and Oseberg blend in North Sea summer conditions and low winds. The discriminative power seems to be persistent with time.

The two selected features are further investigated in Paper III, where the discriminative power is compared between Radarsat-2 and TerraSAR-X acquisitions.

Paper III

S. Skrunes, C. Brekke, T. Eltoft and V. Kudryavtsev, "**Comparing Coincident C- and X-band SAR Acquisitions of Marine Oil Spills**", *IEEE Transactions on Geoscience and Remote Sensing*, in review, 2014.

This paper presents a theoretical and experimental comparison of C- and X-band SAR for oil spill observation, partly based on the findings of Paper I and Paper II. Paper I concludes that TerraSAR-X is more useful for oil spill observation than COSMO-SkyMed when multipolarization techniques are applied. Hence, TerraSAR-X acquisitions are further investigated in this paper. During the OOW-2011 and OOW-2012, Radarsat-2 and TerraSAR-X data were collected less than 24 minutes apart on three different occasions. These three scene pairs are investigated in this study.

The main objective of this paper is to characterize and quantify differences between the Radarsat-2 and TerraSAR-X measurements. Specifically, the analysis consists of first, a data quality study in terms of signal-to-noise levels and damping ratios, and second, an investigation of signal characteristics including statistical properties and dual-copolarization parameters, which are used to infer information about the scattering properties. In particular, we look at how the signal characteristics vary between the two sensors and between low backscatter regions of various origin.

No viable argument for selecting one sensor above the other is identified in the data quality study. A comparison of the feature pair selected in Paper II here shows enhanced slick-sea contrasts and a better discrimination between mineral oil spills and other low backscatter phenomena in Radarsat-2 compared to TerraSAR-X. The difference in incidence angle between the Radarsat-2 and TerraSAR-X scenes may affect the results. The presence of a non-Bragg scattering component in the data is revealed for both sensors. The relative contribution of non-Bragg scattering to the total backscatter is found to be higher in the TerraSAR-X data than in the Radarsat-2 data. This may, at least partly, be related to an increased contribution of specular reflection in the TerraSAR-X data at low incidence angles. In general, the non-Bragg component is found to account for a larger part of the backscatter in slick-covered areas compared to in clean sea. It is found that the ratio between the copolarization channels can be used to suppress a natural low backscatter phenomenon, and that the difference between the channels enhances the slick-sea contrast compared to the individual intensities.

In the statistical analysis, log-cumulants of second and third order (κ_2 and κ_3) extracted from single-look VV intensity are investigated. A larger deviation from Gaussian statistics (higher texture) is found in the TerraSAR-X data compared to the Radarsat-2 measurements. This may be related to the smaller pixel spacing of TerraSAR-X, to variation in relative roughness, or to a difference in scattering properties. The log-cumulant diagram, in particular κ_2, is shown to be a useful tool for discrimination between oil spills and other low backscatter regions in both sensors. Physical variations within the mineral oil slicks may cause the increased texture observed in these areas. The log-cumulants are further investigated in Paper IV, where the analysis is expanded to the multipolarization case.

Paper IV

S. Skrunes, C. Brekke and A. P. Doulgeris, "**Characterization of SAR Low Backscatter Ocean Features Using Log-Cumulants**", *IEEE Geoscience and Remote Sensing Letters*, submitted, 2014.

In this paper, the analysis of log-cumulants presented in Paper III is expanded from the single-look intensity case to the multilook dual-copolarization covariance matrix. The objective is to investigate the potential of log-cumulants for discriminating mineral oil slicks from simulated biogenic slicks and a natural phenomenon. Five Radarsat-2 fine quad-polarization scenes from OOW-2011, OOW-2012 and OOW-2013 are analyzed.

In Paper III, the second order log-cumulant is identified as a powerful feature, whereas the third order log-cumulant exhibits a less discriminative behavior. In this paper, a combination of the first and second order log-cumulants, representing the mean and variance in the log-domain, respectively, is explored. As log-cumulants, and in particular κ_1, can vary with incidence angle and sea state, a normalization with respect to water is applied. A good consistency in the relative log-cumulants is observed between the scenes.

It is found that the combination of the first and second order log-cumulants clearly discriminate the majority of the mineral oil spills from the simulated biogenic slicks and the natural phenomenon. The discrimination between regions is somewhat better when using dual-copolarization data compared to single-polarization intensity and it improves with the degree of multilooking. The proposed method has a potential application in classification of low backscatter ocean regions of unknown origin.

7.2 Other Publications

As first author

1. S. Skrunes, C. Brekke and T. Eltoft, "An Experimental Study on Oil Spill Characterization by Multi-Polarization SAR", *Proc. 9th European Conference on Synthetic Aperture Radar (EUSAR)*, Nuremberg, Germany, 23 - 26 Apr. 2012, pp. 139-142.

2. S. Skrunes, C. Brekke and T. Eltoft, "A Comprehensive Analysis of Polarimetric

Features for Oil Spill Characterization", *Proc. SeaSAR*, Tromsø, Norway, 18 - 22 Jun. 2012, 8 pp.

3. S. Skrunes, C. Brekke and T. Eltoft, "Oil Spill Characterization with Multi-Polarization C- and X-Band SAR", *Proc. IEEE International Geoscience and Remote Sensing Symposium (IGARSS)*, Munich, Germany, 22 - 27 Jul. 2012, pp. 5117-5170.

4. S. Skrunes, C. Brekke and T. Eltoft, "Ocean surface slick characterization by multi-polarization Radarsat-2 data", *Proc. SPIE Remote Sensing*, Edinburgh, Scotland, 24 - 27 Sep. 2012, 15 pp.

As coauthor

1. C. Brekke, V. Kudryavtsev, A.-B. Salberg, S. Skrunes, S. Ermakov, M. Migliaccio and B. Holt, "Current Advances in SAR Remote Sensing of Oil Slicks and a Look-ahead", *Proc. SeaSAR*, Tromsø, Norway, 18 - 22 Jun. 2012, 12 pp.

2. C. Brekke, B. Holt, C. Jones and S. Skrunes, "Towards Oil Slick Monitoring in the Arctic Environment", *Proc. POLinSAR*, Frascati, Italy, 28 Jan - 1 Feb. 2013, 8 pp.

3. C. Brekke, B. Holt, C. Jones and S. Skrunes, "Discrimination of oil spills from newly formed sea ice by synthetic aperture radar", *Remote Sensing of Environment*, vol. 145, pp. 1-14, Apr. 2014.

4. C. Brekke and S. Skrunes, "Polarimetric Synthetic Aperture Radar Measurements of Oil Pollution at Sea", Book chapter, to appear in *Exploitation of fully polarimetric SAR data for application demonstrations (PolSAR-Ap)*, ESA/Springer, 2015, 7 pp.

Chapter 8

Paper I:
An Experimental Study of X-Band Synthetic Aperture Radar (SAR) Imagery for Marine Oil Slick Monitoring

Stine Skrunes, Camilla Brekke, Torbjørn Eltoft and Véronique Miegebielle

Published in: *Proc. 37th Arctic Marine Oilspill Program (AMOP) Technical Seminar on Environmental Contamination and Response*,
Halifax, Canada, 4-6 June 2013, pp. 498-514.

Chapter 9

Paper II:
Characterization of Marine Surface Slicks by Radarsat-2 Multipolarization Features

Stine Skrunes, Camilla Brekke and Torbjørn Eltoft

Published in: *IEEE Transactions on Geoscience and Remote Sensing*,
vol. 52, no. 9, pp. 5302-5319, Sep. 2014.

Chapter 10

Paper III:
Comparing Coincident C- and X-band SAR Acquisitions of Marine Oil Spills

Stine Skrunes, Camilla Brekke, Torbjørn Eltoft and Vladimir Kudryavtsev

In review: *IEEE Transactions on Geoscience and Remote Sensing*,
submitted 27 March 2014, revision submitted 6 June 2014.

Chapter 11

Paper IV:
Characterization of SAR Low Backscatter Ocean Features Using Log-Cumulants

Stine Skrunes, Camilla Brekke and Anthony Paul Doulgeris

Submitted to: *IEEE Geoscience and Remote Sensing Letters*,
submitted 30 June 2014.

Chapter 12

Conclusions and Future Outlook

The papers presented in Chapters 8 - 11 add to the on-going discussion on the application of multipolarization data for oil slick characterization, and provide more information on sensor characteristics and abilities. In this chapter, research conclusions are summarized and a future outlook, including ideas for further research, is given.

12.1 Research Conclusions

A number of multipolarization features have been suggested for oil spill characterization in the literature. In this thesis, a variety of features extracted from dual-copolarization data are investigated for this purpose. In Paper I, features utilizing both intensity and phase information are found to perform better with respect to detection and characterization of slicks, compared to features based on intensity only. Hence, coherent measurements as those provided by Radarsat-2 and TerraSAR-X are considered preferable to COSMO-SkyMed data, in which the phase information is not preserved. In Paper I, the backscatter signal is found to be highly affected by the noise floor at large incidence angles, whereas the multipolarization features provide less information at the smallest incidence angles. Hence, intermediate incidence angles are found preferable for multipolarization analysis.

In Paper II, we investigate eight well-known multipolarization descriptors with potential for oil spill characterization, and compare them in terms of their ability to discriminate between mineral oil spills and a simulated biogenic slick. The geometric intensity and the real part of the copolarization cross product are identified as the most useful features for this purpose. The former measures the combined intensity in the copolarization channels based on the determinant of the coherency matrix, whereas the latter is related to the scattering behavior of the target. The selected feature pair is used as basis for image classification, and is found to discriminate the mineral oils from the simulated biogenic slick.

For characterization purposes, the proximity of the signal level to the sensor noise floor is important. This is addressed in Papers I - III where signal-to-noise analyses are presented. In Paper II, the cross-polarization channels in Radarsat-2 fine quad-polarization data are found to be severely contaminated by noise, and are discarded from the analysis. Features based only on copolarization data are investigated in Papers I - IV.

In Paper I, X-band data are found useful for detection of slicks of various types and ages in low wind conditions, except at very large incidence angles (>55°). A theoretical and experimental comparison between C- and X-band data is presented in Paper III, including analysis of near coincident acquisitions of Radarsat-2 and TerraSAR-X data. No clear difference in the data quality, including signal-to-noise levels and damping ratios, is found between the sensors. The feature pair selected in Paper II shows a better discrimination between clean sea, mineral oils and biogenic slicks in Radarsat-2 compared to TerraSAR-X for this data set. The difference in incidence angle between the Radarsat-2 and TerraSAR-X scenes may affect the results. The presence of a non-Bragg scattering component is revealed in the measurements from both sensors. However, a relatively higher contribution of the non-Bragg component to the total backscatter is found in the TerraSAR-X data compared to the Radarsat-2 data. A general increase in the non-Bragg contribution in the slicks compared to the clean sea is also observed.

Statistical properties are investigated in terms of log-cumulants in Paper III and Paper IV. A larger deviation from Gaussian statistics (higher texture) is found in the TerraSAR-X data compared to Radarsat-2 data in Paper III. This may be related to the smaller pixel spacing of TerraSAR-X, to variation in relative roughness, or to a difference in scattering properties. In Paper III, log-cumulants based on single-look VV intensity are also shown to be useful for discriminating between oil spills and other low backscatter regions in both Radarsat-2 and TerraSAR-X data. Physical variations within the mineral oil slicks may cause the increased texture observed in these areas. This finding is further investigated in Paper IV, with an expansion to the multipolarization domain. A clear separation between mineral oils and other low backscatter ocean phenomena is here obtained using the first and second order log-cumulants extracted from the dual-copolarization covariance matrix. The proposed method has a future potential for classification of low backscatter ocean features of unknown origin.

12.2 Future Outlook

Although satellite SAR data are used operationally for continuous surveillance of ocean areas, e.g., in the European oil spill service CleanSeaNet, some challenges still exist, and new questions arise as the areas of application are expanding. The discrimination between oil spills and look-alikes is one of the main challenges for operational oil spill detection. More documentation on the effect of sensor parameters and their useful ranges of application for oil spill detection and characterization is also requested. These topics are addressed in this thesis. Some thoughts on future research areas and issues that should be further pursued are given in the following.

Over the last decade, a potential for using multipolarization methods for oil spill characterization have been demonstrated in the literature, including the papers presented in this thesis. However, more extensive testing is required to verify these methods, and take them from the research stage to the operational stage. Data over a wider range of wind conditions, sensor parameters (e.g., incidence angles and frequency) and slick properties should be analyzed in order to evaluate the effect of these parameters on the multipolarization descriptors, and map the ranges in which the features are useful. When more data are available, and a better understanding of the features and their applicability is obtained, a feature-based supervised classification method may be established. Such a classification method may be based on, e.g., the feature pair selected in Paper II. The feature comparison conducted in Paper II may also be repeated on a larger data set to evaluate the consistency in the features discriminability. A larger number of descriptors could be included, and a more advanced method for feature comparison could be applied. Particularly the measure for within-class variance should be improved, e.g., by using the coefficient of variation rather than the variance. Several recently launched and planned missions have multipolarization acquisition capabilities, which can increase the availability of these data types, and enhance their operational potential. The CP mode, with the advantage of larger scene coverage compared to quad-polarization and coherent dual-polarization measurements, is likely to be increasingly explored for oil slick characterization.

One limitation of SAR is the lack of slick information that currently can be extracted from these measurements. In particular, information on slick thickness is desired, which would be very valuable information during oil spill response operations. Some papers have suggested that multipolarization features may be used to observe thickness variations within an oil spill. In studies not included in this thesis, we find that feature-based classification results show internal zoning in the oil spills that correlate well with expected thickness variations [Skrunes et al., 2012a, Skrunes et al., 2012c]. However, more extensive ground truth data, e.g., aerial photo or in situ measurements, are needed for reliable interpretation of the SAR results.

Obtaining data for research on oil spill remote sensing can be a challenge. The data collection during oil-on-water exercises has been essential for us to carry out the work presented in this thesis. Efforts to collect data during oil-on-water exercises and similar events should be continued in order to build up a more extensive SAR data set with varying sensor, weather and slick parameters, as well as corresponding ground truth and ancillary data. Data were collected during OOW-2014 that took place 17 - 20 June 2014, and the planning of OOW-2015 is on-going, including plans for data acquisition with the NASA UAVSAR. Data simulation may be an alternative to, or used in complement with, experimental data collection.

As shown in Papers I - III, the backscatter signal in satellite SAR sensors can be significantly affected by the sensor noise floor, especially at cross-polarization channels, at large incidence angles and in low wind conditions. Hence, care should be exercised when using the data for characterization purposes. In this thesis, we have excluded the cross-polarization channels from the analyzes. However, the copolarization channels can also be somewhat influenced by the noise, which in turn can affect, e.g., the interpretation of multipolarization descriptors. This issue should be further explored. Also, careful selection of imaging modes may somewhat mitigate this problem. In Radarsat-2, a lower noise floor can be obtained by using the standard quad-polarization mode rather than the fine quad-polarization mode, but at the cost of reduced resolution.

The variation in multipolarization feature values among oil spills, look-alikes and clean sea, is often related to the present scattering mechanisms (Bragg versus non-Bragg). Although many studies indicate the presence of a non-Bragg scattering mechanism within mineral oils, this result seem to be neither generally accepted nor well explained in the literature, and further research on this topic is needed. In Paper III, the relative contributions of the two components are evaluated for various low backscatter regions. This model could be further explored in future work. The validity of the estimation of p_B should be more thoroughly investigated, and the parameters could be compared to the theoretical values of the two-scale Bragg model. Since p_B is the ratio between the Bragg components only, it may be possible to estimate dielectric properties from this parameter, in a similar manner as [Minchew et al., 2012] did for the total backscatter.

The multipolarization features investigated in Paper II are combinations of the S_{HH} and S_{VV} measurements. Unfortunately, not all sensors offer this channel combination, e.g., the recently launched European SAR satellite Sentinel-1. Hence, it is important to also explore the possibility of oil spill characterization in single-polarization data. In Paper III and Paper IV, a potential for using log-cumulants for mineral oil versus look-alike discrimination is found, also for single-polarization intensity. Further exploration of this method on multilook intensity data should be carried out, with the possibility of developing an operationally viable method for classification of low backscatter regions of unknown origin. More effort should be put into the identification of a reliable segmentation method and an appropriate decision boundary.

As the Arctic sea ice is melting, the petroleum industry and shipping activities are expected to move towards higher latitudes. This leads to new challenges when it comes to marine oil spill detection and response systems. Little is known about remote sensing of oil under, on, and within ice, but this is likely to be an increasingly discussed topic in the literature. The discrimination between oil spills and natural seeps, which is known to appear in the Barents Sea, is also becoming more relevant [Brekke et al., 2012]. A combination of different remote sensing systems may be needed in Arctic conditions.

As long as oil is being produced and transported at sea, there is a risk of accidental and deliberate releases of oil into the marine environment. SAR will continue to be a valuable tool for detection and monitoring of these spills, and the on-going research suggests that even more information may be extracted from SAR data in the future. Satellite SAR and other remote sensing systems, including aircrafts, aerostats, UAVs and ship based sensors, can be used in combination to reduce the number of illegal oil releases and limit the impacts of accidental spills.

Bibliography

[Alpers and Espedal, 2004] W. Alpers and H. A. Espedal. *Oils and surfactants*. In *Synthetic Aperture Radar Marine User's Manual*, edited by C. R. Jackson and J. R. Apel, pp. 263–275. U.S. Department of Commerce, National Oceanic and Atmospheric Administration, Sep. 2004.

[Alpers and Hühnerfuss, 1988] W. Alpers and H. Hühnerfuss. *Radar signatures of oil films floating on the sea surface and the marangoni effect*. *J. Geophys. Res.*, **93**(C4): 3642–3648, Apr. 1988.

[Anfinsen, 2010] S. N. Anfinsen. *Statistical analysis of multilook polarimetric radar images with the Mellin transform*. Ph.D. thesis, University of Tromsø, Norway, May 2010.

[Anfinsen and Eltoft, 2011] S. N. Anfinsen and T. Eltoft. *Application of the matrix-variate Mellin transform to analysis of polarimetric radar images*. *IEEE Trans. Geosci. Remote Sens.*, **49**(6): 2281–2295, Jun. 2011.

[Bombrun et al., 2011] L. Bombrun, S. N. Anfinsen and O. Harant. *A complete coverage of log-cumulant space in terms of distributions for polarimetric SAR data*. In *Proc. of POLinSAR*. Frascati, Italy, Jan. 2011.

[Bonn Agreement, 2009] Bonn Agreement. *Bonn agreement aerial operations handbook*. URL: http://www.bonnagreement.org/eng/doc/Bonn Agreement Aerial Operations Handbook.pdf, Visited 30. Jun. 2014, May 2009.

[Brekke, 2008] C. Brekke. *Automatic screening of synthetic aperture radar imagery for detection of oil pollution in the marine environment*. Ph.D. thesis, University of Oslo, Norway, 2008.

[Brekke and Solberg, 2005] C. Brekke and A. H. S. Solberg. *Oil spill detection by satellite remote sensing*. *Remote Sens. Environ.*, **95**: 1–13, 2005.

[Brekke et al., 2012] C. Brekke, V. Kudryavtsev, A.-B. Salberg, S. Skrunes, S. Ermakov, M. Migliaccio and B. Holt. *Current advances in SAR remote sensing of oil slicks and a look-ahead*. In *Proc. SeaSAR*. Tromsø, Norway, Jun. 2012.

[Canada Centre for Remote Sensing, 2007] Canada Centre for Remote Sensing. *Fundamentals of remote sensing*. URL: http://www.nrcan.gc.ca/sites/www.nrcan.gc.ca/files/earthsciences/pdf/resource/tutor /fundam/pdf/fundamentals_e.pdf, Visited 30. Jun. 2014, Aug. 2007.

[Caruso et al., 2013] M. J. Caruso, M. Migliaccio, J. T. Hargrove, O. Garcia-Pineda and H. C. Graber. *Oil spills and slicks imaged by synthetic aperture radar*. *Oceanography*, **26**(2): 112–123, 2013.

[Chan-Su et al., 2013] Y. Chan-Su, P. Seong-Min, O. Yisok and O. Kazuo. *An analysis of the radar backscatter from oil-covered sea surfaces using moment method and Monte-Carlo simulation: preliminary results*. *Acta Oceanologica Sinica*, **32**(1): 59–67, 2013.

[Clemente-Colón and Yan, 2000] P. Clemente-Colón and X.-H. Yan. *Low-backscatter ocean features in synthetic aperture radar imagery*. *Johns Hopkins Apl. Technical Digest*, **21**(1): 116–121, 2000.

[Cloude and Pottier, 1997] S. R. Cloude and E. Pottier. *An entropy based classification scheme for land applications of polarimetric SAR*. *IEEE Trans. Geosci. Remote Sens.*, **35**(1): 68 –78, Jan. 1997.

[Cumming and Wong, 2005] I. G. Cumming and F. H. Wong. *Digital processing of Synthetic Aperture Radar data: Algorithms and Implementation*. Artech House, Norwood, USA, 2005.

[Danklmayer et al., 2009] A. Danklmayer, B. J. Döring, M. Schwerdt and M. Chandra. *Assessment of atmospheric propagation effects in SAR images*. *IEEE Trans. Geosci. Remote Sens.*, **47**(10): 3507–3518, Oct. 2009.

[Donelan and Pierson Jr, 1987] M. A. Donelan and W. J. Pierson Jr. *Radar scattering and equilibrium ranges in wind-generated waves with application to scatterometry*. *J. Geophys. Res.*, **92**(C5): 4971–5029, May 1987.

[Earth Observation Portal, 2014] Earth Observation Portal. URL:https://directory.eoportal.org/web/eoportal/satellite-missions, Visited 27. Jun. 2014, 2014.

[Elachi and van Zyl, 2006] C. Elachi and J. van Zyl. *Introduction to the physics and techniques of remote sensing*. John Wiley & Sons, Inc., Hoboken, USA, 2006.

[Espedal et al., 1998] H. A. Espedal, O. M. Johannessen, J. A. Johannessen, E. Dano, D. R. Lyzenga and J. C. Knulst. *COASTWATCH'95: ERS 1/2 SAR detection of natural film on the ocean surface*. *J. Geophys. Res.*, **103**(C11): 24969–24982, Oct. 1998.

[European Maritime Safety Agency, 2011] European Maritime Safety Agency. *CleanSeaNet First Generation*. URL: http://emsa.europa.eu/operations/cleanseanet/items/id/1309.html?cid=122, Visited 4. Jul. 2014, 2011.

[Ferraro et al., 2006] G. Ferraro, D. Tarchi, J. Fortuny and A. Sieber. *Satellite monitoring of accidental and deliberate marine oil pollution*. In *Marine Surface Films: Chemical Characteristics, Influence on Air-Sea Interactions and Remote Sensing*, edited by M. Gade, H. Hühnerfuss and G. Korenowski, pp. 273–288. Springer-Verlag Berlin Heidelberg, 2006.

[Ferraro et al., 2009] G. Ferraro, S. Meyer-Roux, O. Muellenhoff, M. Pavliha, J. Svetak, D. Tarchi and K. Topouzelis. *Long term monitoring of oil spills in European seas*. *Int. J. Remote Sens.*, **30**(3): 627–645, Feb. 2009.

[Fingas, 2011a] M. Fingas. *Introduction*. In *Oil Spill Science and Technology*, edited by M. Fingas, chapter 1, pp. 3–5. Elsevier Inc., Burlington, USA, 2011a.

[Fingas, 2011b] M. Fingas. *Introduction to oil chemistry and properties*. In *Oil Spill Science and Technology*, edited by M. Fingas, chapter 3, pp. 51–59. Elsevier Inc., Burlington, USA, 2011b.

[Fingas, 2011c] M. Fingas. *Introduction to spill modeling*. In *Oil Spill Science and Technology*, edited by M. Fingas, chapter 8, pp. 187–200. Elsevier Inc., Burlington, USA, 2011c.

[Fingas, 2011d] M. Fingas, ed. *Oil Spill Science and Technology*. Elsevier Inc., Burlington, USA, 2011d.

[Fingas and Brown, 2011] M. Fingas and C. E. Brown. *Oil spill remote sensing: A review*. In *Oil Spill Science and Technology*, edited by M. Fingas, chapter 6, pp. 111–169. Elsevier Inc., Burlington, USA, 2011.

[Folgerø, 1996] K. Folgerø. *Bilinear calibration of coaxial transmission/reflection cells for permittivity measurements of low-loss liquids*. *Meas. Sci. Technol.*, **7**(9): 1260–1269, Sep. 1996.

[Fortuny-Guasch, 2003] J. Fortuny-Guasch. *Improved oil slick detection and classification with polarimetric SAR*. In *Proc. Workshop POLinSAR*. Frascati, Italy, Jan. 2003.

[Franceschetti et al., 2002] G. Franceschetti, A. Iodice, D. Riccio, G. Ruello and R. Siviero. *SAR raw signal simulation of oil slicks in ocean environments*. *IEEE Trans. Geosci. Remote Sens.*, **40**(9): 1935–1949, Sep. 2002.

[Frate et al., 2011] F. D. Frate, A. Giacomini, D. Latini, D. Solimini and W. J. Emery. *The Gulf of Mexico oil rig accident: analysis by different SAR satellite images*. In *Proc. of SPIE*, volume 8179. Oct., 2011.

[Gade and Alpers, 1999] M. Gade and W. Alpers. *Using ERS-2 SAR images for routine observation of marine pollution in European coastal waters*. *The Sci. of the Total Environ.*, **237-238**: 441–448, Sep. 1999.

[Gade et al., 1998] M. Gade, W. Alpers, H. Hühnerfuss, H. Masuko and T. Kobayashi. *Imaging of biogenic and anthropogenic ocean surface films by the multifrequency/multipolarization SIR-C/X-SAR*. *J. Geophys. Res.*, **103**(C9): 18,851–18,866, Aug. 1998.

[Gade et al., 2013] M. Gade, V. Byfield, S. Ermakov, O. Lavrova and L. Mitnik. *Slicks as indicators for marine processes*. *Oceanography*, **26**(2): 138–149, 2013.

[German Aerospace Center, 2010] German Aerospace Center. *TerraSAR-X ground segment basic product specification document*. URL: http://www.dlr.de/dlr/Portaldata/1/Resources/documents/TX-GS-DD-3302_Basic-Product-Specification-Document_1_7.pdf, Visited 30. Jun. 2014, Oct. 2010.

[Girard-Ardhuin et al., 2005] F. Girard-Ardhuin, G. Mercier, F. Collard and R. Garello. *Operational oil-slick characterization by SAR imagery and synergistic data*. *IEEE J. of Oceanic Eng.*, **30**(3): 487–495, Jul. 2005.

[Hollebone, 2011] B. Hollebone. *Measurement of oil physical properties*. In *Oil Spill Science and Technology*, edited by M. Fingas, chapter 4, pp. 63–86. Elsevier Inc., Burlington, USA, 2011.

[Hollinger and Mennella, 1973] J. P. Hollinger and R. A. Mennella. *Oil spills: measurements of their distributions and volumes by multifrequency microwave radiometry*. *Science*, **181**(4094): 54–56, Jul. 1973.

[Holt, 2004] B. Holt. *SAR imaging of the ocean surface*. In *Synthetic Aperture Radar Marine User's Manual*, edited by C. Jackson and J. Apel, pp. 25–80. U.S. Department of Commerce, National Oceanic and Atmospheric Administration, Washington DC, USA, Sep. 2004.

[Hühnerfuss, 2006] H. Hühnerfuss. *Basic physicochemical principles of monomolecular sea slicks and crude oil spills*. In *Marine Surface Films: Chemical Characteristics, Influence on Air-Sea Interactions and Remote Sensing*, edited by M. Gade, H. Hühnerfuss and G. M. Korenowski, pp. 21–35. Springer-Verlag Berlin Heidelberg, 2006.

[Italian Space Agency, 2009] Italian Space Agency. *COSMO-SkyMed SAR products handbook*. URL: http://www.e-geos.it/products/pdf/csk-product handbook.pdf, Visited 30. Jun. 2014, 2009.

[Ivanov, 2010] A. Y. Ivanov. *The oil spill from a shipwreck in Kerch Strait: radar monitoring and numerical modelling*. *Int. J. Remote Sens.*, **31**(17-18): 4853–4868, Sep. 2010.

[Ivanov, 2011] A. Y. Ivanov. *Remote sensing of oil films in the context of global changes*. In *Remote Sensing of the Changing Oceans*, edited by D. Tang, chapter 9, pp. 169–191. Springer-Verlag Berlin Heidelberg, 2011.

[Jha et al., 2008] M. N. Jha, J. Levy and Y. Gao. *Advances in remote sensing for oil spill disaster management: State-of-the-art sensors technology for oil spill surveillance*. *Sensors*, **8**: 236–255, 2008.

[Johnsen et al., 2008] H. Johnsen, G. Engen and G. Guitton. *Sea-surface polarization ratio from Envisat ASAR AP data*. *IEEE Trans. Geosci. Remote Sens.*, **46**(11): 3637–3646, Nov. 2008.

[Jones, 2001] B. Jones. *A comparison of visual observations of surface oil with Synthetic Aperture Radar imagery of the Sea Empress oil spill*. *Int. J. Remote Sens.*, **22**(9): 1619–1638, 2001.

[Jones et al., 2011a] C. Jones, B. Minchew and B. Holt. *Polarimetric decomposition analysis of the Deepwater Horizon oil slick using L-band UAVSAR data*. In *Proc. IEEE Int. Geosci. Remote Sens. Symp.*, pp. 2278–2281. Vancouver, Canada, Jul. 2011a.

[Jones et al., 2011b] C. E. Jones, B. Minchew, B. Holt and S. Hensley. *Studies of the Deepwater Horizon oil spill with the UAVSAR radar*. In *Monitoring and Modeling the Deepwater Horizon Oil Spill: A Record-Breaking Enterprise*, edited by Y. Liu, A. M. andZ. G. Ji and R. H. Weisberg, pp. 33–50. American Geophysical Union, Washington DC, USA, 2011b.

[Kim et al., 2010] D.-J. Kim, W. Moon and Y.-S. Kim. *Application of TerraSAR-X data for emergent oil-spill monitoring*. *IEEE Trans. Geosci. Remote Sens.*, **48**(2): 852 –863, Feb. 2010.

[Klemas, 2010] V. Klemas. *Tracking oil slicks and predicting their trajectories using remote sensors and models: Case studies of the Sea Princess and Deepwater Horizon oil spills*. *J. Coastal Res.*, **26**(5): 789–797, Sep. 2010.

[Kluser et al., 2006] S. Kluser, J. P. Richard, G. Giuliani, A. D. Bono and P. Peduzzi. *Illegal oil discharge in European seas*. *Environ. Alert Bulletin*, Feb. 2006.

[Kotova et al., 1998] L. A. Kotova, H. A. Espedal and O. M. Johannessen. *Oil spill detection using spaceborne SAR; a brief review*. *Proc. 27th ISRSE, Tromsø, Norway*, 1998.

[Kudryavtsev et al., 2003] V. Kudryavtsev, D. Hauser, G. Caudal and B. Chapron. *A semiempirical model of the normalized radar cross-section of the sea surface, 1. background model*. *J. Geophys. Res.*, **108**(C3): FET 2–1–FET 2–24, 2003.

[Kudryavtsev et al., 2013] V. Kudryavtsev, B. Chapron, A. Myasoedov, F. Collard and J. Johannessen. *On dual co-polarized SAR measurements of the ocean surface*. *IEEE Geosci. Remote Sens. Lett.*, **10**(4): 761–765, 2013.

[Kwon and Li, 2012] T.-J. Kwon and J. Li. *Mapping marine oil spills from space*. In *Advances in Mapping from Remote Sensor Imagery: Techniques and Applications*, edited by X. Yang and J. Li, chapter 15, pp. 361–386. CRC Press, Boca Raton, USA, 2012.

[Lee and Pottier, 2009] J.-S. Lee and E. Pottier. *Polarimetric Radar Imaging, from basics to applications*. CRC Press, Taylor and Francis Group, Boca Raton, USA, 2009.

[Lehr, 2001] W. J. Lehr. *Review of modeling procedures for oil spill weathering behavior*. In *Oil Spill Modelling and Processes*, edited by C. A. Brebbia. WIT Press, Boston, USA, 2001.

[Leifer et al., 2012] I. Leifer, W. J. Lehr, D. Simecek-Beatty, E. Bradley, R. Clark, P. Dennison, Y. Hu, S. Matheson, C. E. Jones, B. Holt, M. Reif, D. A. Roberts, J. Svejkovsky, G. Swayze and J. Wozencraft. *State of the art satellite and airborne marine oil spill remote sensing: Application to the BP Deepwater Horizon oil spill*. *Remote Sens. Environ.*, **124**: 185–209, Sep. 2012.

[Liu et al., 2011] P. Liu, X. Li, J. J. Qu, W. Wang, C. Zhao and W. Pichel. *Oil spill detection with fully polarimetric UAVSAR data*. *Marine Pollution Bulletin*, **62**(12): 2611–2618, Dec. 2011.

[Lombardo and Oliver, 2000] P. Lombardo and C. J. Oliver. *Optimum detection and segmentation of oil-slicks using polarimetric SAR*. In *IEE Proc. Radar, Sonar Navig.*, volume 147, pp. 309–321. Dec. 2000.

[MacDonald, Dettwiler and Associates Ltd., 2009] MacDonald, Dettwiler and Associates Ltd. *Radarsat-2 product description*. URL: http://gs.mdacorporation.com/products/sensor/radarsat2/rs2_product_description.pdf, Visited 30. Jun. 2014, Nov. 2009.

[MacDonald, Dettwiler and Associates Ltd., 2011] MacDonald, Dettwiler and Associates Ltd. *Radarsat-2 product description*. URL: http://gs.mdacorporation.com/includes/documents/RN-SP-52-1238 RS-2 Product Description 1-8_15APR2011.pdf, Visited 30. Jun. 2014, 2011.

[Massonnet and Souyris, 2008] D. Massonnet and J.-C. Souyris. *Imaging with synthetic aperture radar*. CRC Press, Taylor and Francis Group, Boca Raton, USA, 2008.

[McCandless and Jackson, 2004] S. W. McCandless and C. R. Jackson. *Principles of synthetic aperture radar*. In *Synthetic Aperture Radar Marine User's Manual*, edited by C. Jackson and J. R. Apel, chapter 1, pp. 1–23. U.S. Department of Commerce, National Oceanic and Atmospheric Administration, Washington DC, USA, Sep. 2004.

[Migliaccio and Nunziata, 2014] M. Migliaccio and F. Nunziata. *On the exploitation of polarimetric SAR data to map damping properties of the Deepwater Horizon oil spill*. *Int. J. Remote Sens.*, **35**(10): 3499–3519, 2014.

[Migliaccio et al., 2007] M. Migliaccio, A. Gambardella and M. Tranfaglia. *SAR polarimetry to observe oil spills*. *IEEE Trans. Geosci. Remote Sens.*, **45**(2): 506 –511, Feb. 2007.

[Migliaccio et al., 2008] M. Migliaccio, F. Nunziata and A. Gambardella. *Polarimetric signature for oil spill observation*. In *Proc. IEEE/OES US/EU-Baltic Int. Symp., 2008*, pp. 1–5. May 2008.

[Migliaccio et al., 2009a] M. Migliaccio, A. Gambardella, F. Nunziata, M. Shimada and O. Isoguchi. *The PALSAR polarimetric mode for sea oil slick observation*. *IEEE Trans. Geosci. Remote Sens.*, **47**(12): 4032 –4041, Dec. 2009a.

[Migliaccio et al., 2009b] M. Migliaccio, F. Nunziata and A. Gambardella. *On the co-polarized phase difference for oil spill observation*. *Int. J. Remote Sens.*, **30**(6): 1587–1602, Mar. 2009b.

[Migliaccio et al., 2011a] M. Migliaccio, F. Nunziata, A. Montuori and C. E. Brown. *Marine added-value products using RADARSAT-2 fine quad-polarization*. *Can. J. Remote Sens.*, **37**(5): 443–451, 2011a.

[Migliaccio et al., 2011b] M. Migliaccio, F. Nunziata, A. Montuori, X. Li and W. G. Pichel. *A multifrequency polarimetric SAR processing chain to observe oil fields in the Gulf of Mexico*. *IEEE Trans. Geosci. Remote Sens.*, **49**(12): 4729–4737, Dec. 2011b.

[Minchew, 2012] B. Minchew. *Determining the mixing of oil and sea water using polarimetric synthetic aperture radar*. *Geophys. Res. Lett.*, **39**, 2012.

[Minchew et al., 2012] B. Minchew, C. E. Jones and B. Holt. *Polarimetric analysis of backscatter from the Deepwater Horizon oil spill using L-band synthetic aperture radar*. *IEEE Trans. Geosci. Remote Sens.*, **50**(10): 3812–3830, Oct. 2012.

[Moreira et al., 2013] A. Moreira, P. Prats-Iraola, M. Younis, G. Krieger, I. Hajnsek and K. P. Papathanassiou. *A tutorial on synthetic aperture radar*. *IEEE Geosci. Remote Sens. Magazine*, **1**(1): 6–43, Mar. 2013.

[National Research Council, 2003] National Research Council. *Oil in the Sea III: Inputs, Fates and Effects*. The National Academic Press, Washington DC, USA, 2003.

[Nicolas, 2002] J.-M. Nicolas. *Introduction aux statistiques de deuxième espèce: applications des logs-moments et des logs-cumulants à l'analyse des lois d'images radar*. *Traitement du Signal*, **19**(3): 139–167, 2002.

[Nicolas and Anfinsen, 2012] J.-M. Nicolas and S. N. Anfinsen. *Introduction to second kind statistics: Application of log-moments and log-cumulants to the analysis of radar image distributions*. Technical note, translation from French of [Nicolas, 2002]. URL: http://eo.uit.no/publications/jmn-trans-12.pdf, Visited 30. Jun. 2014, May 2012.

[Nunziata and Migliaccio, 2013] F. Nunziata and M. Migliaccio. *On the COSMO-SkyMed PingPong mode to observe metallic targets at sea*. *IEEE J. of Oceanic Eng.*, **38**(1): 71–79, 2013.

[Nunziata et al., 2008] F. Nunziata, A. Gambardella and M. Migliaccio. *On the Mueller scattering matrix for SAR sea oil slick observation*. *IEEE Geosci. Remote Sens. Lett.*, **5**(4): 691–695, Oct. 2008.

[Nunziata et al., 2011] F. Nunziata, M. Migliaccio and A. Gambardella. *Pedestal height for sea oil slick observation*. *IET Radar, Sonar Navig.*, **5**(2): 103 –110, Feb. 2011.

[Nunziata et al., 2012] F. Nunziata, A. Gambardella and M. Migliaccio. *A unitary Mueller-based view of polarimetric SAR oil slick observation*. *Int. J. Remote Sens.*, **33**(20): 6403–6425, Oct. 2012.

[Nunziata et al., 2013] F. Nunziata, A. Gambardella and M. Migliaccio. *On the degree of polarization for SAR sea oil slick observation*. *ISPRS J. of Photogrammetry and Remote Sens.*, **78**: 41–49, 2013.

[Oliver and Quegan, 2004] C. Oliver and S. Quegan. *Understanding Synthetic Aperture Radar Images*. SciTech Publishing Inc., Raleigh, USA, 2004.

[Palenzuela et al., 2006] J. M. T. Palenzuela, L. G. Vilas and M. S. Cuadrado. *Use of ASAR images to study the evolution of the Prestige oil spill off the Galician coast*. *Int. J. Remote Sens.*, **27**(10): 1931–1950, May 2006.

[Pavlakis et al., 2001] P. Pavlakis, D. Tarchi and A. Sieber. *On the monitoring of illicit vessel discharges using spaceborne SAR remote sensing - a reconnaissance study in the Mediterranean sea*. *Annals of Telecommunications*, **56**(11-12): 700–718, 2001. 10.1007/BF02995563.

[Pinel et al., 2014] N. Pinel, C. Bourlier and I. Sergievskaya. *Two-dimensional radar backscattering modeling of oil slicks at sea based on the model of local balance: Validation of two asymptotic techniques for thick films*. *IEEE Trans. Geosci. Remote Sens.*, **52**(5): 2326–2338, May 2014.

[Raney, 2011] R. K. Raney. *A perspective on compact polarimetry*. *IEEE Geosci. Remote Sens. Newslett.*, pp. 12–18, Sep. 2011.

[Reed et al., 1999] M. Reed, Ø. Johansen, P. J. Brandvik, P. Daling, A. Lewis, R. Fiocco, D. Mackay and R. Prentki. *Oil spill modeling towards the close of the 20th century: overview of the state of the art*. *Spill Sci. and Technology Bulletin*, **5**(1): 3–16, 1999.

[Salberg et al., 2014] A. Salberg, O. Rudjord and A. Solberg. *Oil spill detection in hybrid-polarimetric SAR images*. *IEEE Trans. Geosci. Remote Sens.*, **52**(10): 6521–6533, Oct. 2014.

[Schmidt-Etkin, 2011] D. Schmidt-Etkin. *Spill occurrences: A world overview*. In *Oil Spill Science and Technology*, edited by M. Fingas, chapter 2, pp. 7–48. Elsevier Inc., Burlington, USA, 2011.

[Schuler and Lee, 2006] D. L. Schuler and J.-S. Lee. *Mapping ocean surface features using biogenic slick-fields and SAR polarimetric decomposition techniques*. In *IEE Proc. Radar, Sonar Navig.*, volume 153, pp. 260 – 270. Jun. 2006.

[Shigenaka, 2011] G. Shigenaka. *Effects of oil in the environment*. In *Oil Spill Science and Technology*, edited by M. Fingas, chapter 27, pp. 985–1024. Elsevier Inc., Burlington, USA, 2011.

[Shirvany et al., 2012] R. Shirvany, M. Chabert and J.-Y. Tourneret. *Ship and oil-spill detection using the degree of polarization in linear and hybrid/compact dual-pol SAR*. *IEEE J. Sel. Topics Appl. Earth Observ.*, **5**(3): 885–892, Jun. 2012.

[Skrunes et al., 2012a] S. Skrunes, C. Brekke and T. Eltoft. *A comprehensive analysis of polarimetric features for oil spill characterization*. In *Proc. SeaSAR*. Tromsø, Norway, Jun. 2012a.

[Skrunes et al., 2012b] S. Skrunes, C. Brekke and T. Eltoft. *Ocean surface slick characterization by multi-polarization Radarsat-2 data*. In *Proc. SPIE*. Edinburgh, Scotland, Sep. 2012b.

[Skrunes et al., 2012c] S. Skrunes, C. Brekke and T. Eltoft. *Oil spill characterization with multi-polarization C- and X-band SAR*. In *Proc. IEEE Int. Geosci. Remote Sens. Symp.*, pp. 5117–5120. Munich, Germany, Jul. 2012c.

[Solberg, 2012] A. H. S. Solberg. *Remote sensing of ocean oil-spill pollution*. *Proc. IEEE*, **100**(10): 2931–2945, Oct. 2012.

[Solberg and Brekke, 2008] A. H. S. Solberg and C. Brekke. *Oil spill detection in northern European waters: approaches and algorithms*. In *Remote Sensing of the European Seas*, edited by V. Barale and M. Gade, pp. 359–370. Springer Science+Business Media B.V., 2008.

[The International Tanker Owners Pollution Federation Limited, 2002] The International Tanker Owners Pollution Federation Limited. *Fate of marine oil spills*. Technical report, 2002.

[The International Tanker Owners Pollution Federation Limited, 2014] The International Tanker Owners Pollution Federation Limited. *Oil tanker spill statistics 2013*. URL: http://www.itopf.com/fileadmin/data/Documents/Company_Lit/OilSpillstats_2013.pdf, Visited 4. Jul. 2014, 2014.

[Tian et al., 2010] W. Tian, Y. Shao, J. Yuan, S. Wang and Y. Liu. *An experiment for oil spill recognition using RADARSAT-2 image*. In *Proc. IEEE Int. Geosci. Remote Sens. Symp.*, pp. 2761 –2764. Honolulu, USA, Jul. 2010.

[Topouzelis, 2008] K. N. Topouzelis. *Oil spill detection by SAR images: Dark formation detection, feature extraction and classification algorithms*. *Sensors*, **8**(10): 6642–6659, 2008.

[Touzi et al., 2004] R. Touzi, W. M. Boerner, J. S. Lee and E. Lueneburg. *A review of polarimetry in the context of synthetic aperture radar: concepts and information extraction*. *Can. J. Remote Sens.*, **30**(3): 380–407, 2004.

[Ulaby et al., 1986a] F. Ulaby, R. K. Moore and A. K. Fung. *Microwave remote sensing, active and passive, volume II; Radar remote sensing and emission theory*. Artech House Inc., Norwood, USA, 1986a.

[Ulaby et al., 1986b] F. T. Ulaby, R. K. Moore and A. K. Fung. *Microwave remote sensing, active and passive, volume III; From theory to applications*. Artech House Inc., Norwood, USA, 1986b.

[Ulaby et al., 1992] F. T. Ulaby, K. Sarabandi and A. Nashashibi. *Statistical properties of the Mueller matrix of distributed targets*. In *IEE Proc.-F Radar Signal Processing*, volume 139, pp. 136–146. Apr. 1992.

[Valenzuela, 1967] G. R. Valenzuela. *Depolarization of EM waves by slightly rough surfaces*. *IEEE Trans. Antennas Propag.*, **15**(4): 552–557, Jul. 1967.

[Valenzuela, 1978] G. R. Valenzuela. *Theories for the interaction of electromagnetic and oceanic waves - a review*. *Boundary-Layer Meteorology*, **13**(1-4): 61–85, Jan. 1978.

[Velotto et al., 2011] D. Velotto, M. Migliaccio, F. Nunziata and S. Lehner. *Dual-polarized TerraSAR-X data for oil-spill observation*. *IEEE Trans. Geosci. Remote Sens.*, **49**(12): 4751–4762, Dec. 2011.

[Vespe and Greidanus, 2012] M. Vespe and H. Greidanus. *SAR image quality assessment and indicators for vessel and oil spill detection*. *IEEE Trans. Geosci. Remote Sens.*, **50**(11): 4726–4734, Nov. 2012.

[Vespe et al., 2010] M. Vespe, M. Posada, G. Ferraro and H. Greidanus. *Perspectives on oil spill detection using synthetic aperture radar*. In *Oceanography from Space: Revisited*, edited by V. Barale, J. F. R. Gower and L. Alberotanza. Springer Science+Business Media B.V., 2010.

[Vieites et al., 2004] D. R. Vieites, S. Nieto-Roman, A. Palanca, X. Ferrer and M. Vences. *European atlantic: the hottest oil spill hotspot worldwide*. *Naturwissenschaften*, **91**(11): 535–538, 2004.

[Wenguang et al., 2010] W. Wenguang, L. Fei, W. Peng and W. Jun. *Oil spill detection from polarimetric SAR image*. In *Proc. IEEE Int. Conf. Signal Process.*, pp. 832 –835. Oct. 2010.

[Wismann et al., 1993] V. Wismann, R. Theis, W. Alpers and H. Hühnerfuss. *The damping of short gravity-capillary waves by experimental sea slicks measured by an airborne multi-frequency microwave scatterometer*. In *Proc. OCEANS '93. Eng. in Harmony with Ocean*, volume 2, pp. II342–II347. Oct. 1993.

[Wismann et al., 1998] V. Wismann, M. Gade, W. Alpers and H. Hühnerfuss. *Radar signatures of marine mineral oil spills measured by an airborne multi-frequency radar*. *Int. J. Remote Sens.*, **19**(18): 3607–3623, 1998.

[Woodhouse, 2006] I. H. Woodhouse. *Introduction to Microwave Remote Sensing*. Taylor & Francis Group, Boca Raton, USA, 2006.

[Zhang et al., 2011] B. Zhang, W. Perrie, X. Li and W. G. Pichel. *Mapping sea surface oil slicks using RADARSAT-2 quad-polarization SAR image*. *Geophys. Res. Lett.*, **38**(10), May 2011.

[van Zyl and Kim, 2011] J. van Zyl and Y. Kim. *Synthetic Aperture Radar Polarimetry*. John Wiley & Sons, Inc., Hoboken, USA, 2011.